



**Improving
Feature-based
Non-rigid
Registration
for Applications
in Radiotherapy**

Eliana Vásquez Osorio

Improving Feature-based Non-rigid Registration for Applications in Radiotherapy

Cover design: Koleia Arvila and Wouter Wunderink
Layout: Eliana M. Vásquez Osorio
Fonts: Linux Libertine and Linux Biolinum

Copyright:

- © Eliana M. Vásquez Osorio
- © American Association of Physicists in Medicine (chapters 3 and 4)
- © Elsevier Inc. (chapters 5 and 6)

ISBN: 978-90-6464-537-2

Improving Feature-based Non-rigid Registration for Applications in Radiotherapy

Het verbeteren van kenmerkgestuurde niet-rigide
registratie voor toepassingen in de radiotherapie

Thesis

to obtain the degree of Doctor from the
Erasmus University Rotterdam
by command of the
rector magnificus

Prof.dr. H.G. Schmidt

and in accordance with the decision of the Doctorate Board

The public defence shall be held on
Thursday, 5 April 2012 at 15.30 hours

by

Eliana María Vásquez Osorio
born in Medellín, Colombia



Doctoral Committee

Promoter: Prof.dr. B.J.M. Heijmen

Other members: Prof.dr. P.C. Levendag
Prof.dr. W.J. Niessen
Prof.dr. M.B. van Herk

Copromoter: Dr. M.S. Hoogeman

This thesis has been prepared at the Department of Radiation Oncology, Erasmus MC - Daniel den Hoed Cancer Center, Rotterdam, The Netherlands. The printing of this thesis was partially funded by Elekta BV and Accuray, Inc.

E-mail for correspondence: e.vasquezosorio@gmail.com

‘The most exciting phrase to hear in science,
the one that heralds new discoveries,
is not “Eureka!” (“I found it!”)
but rather “hmm... that’s funny...” ’
– Isaac Asimov

Because it is always good to start with a smile! :)

Contents

1	Introduction	1
1.1	Radiotherapy	3
1.1.1	Treatment precision and anatomical changes	4
1.2	Image registration	5
1.3	This thesis	7
1.3.1	Non-rigid registration method	7
1.3.2	Applications in radiotherapy	8
2	Non-rigid point based registration. A summary of the original method	11
2.1	Introduction	13
2.2	Definition of point registration	13
2.3	Correspondence	14
2.3.1	Fuzzy correspondence using softassign	15
2.3.2	Handling outliers	15
2.3.3	Back from fuzzy to discrete correspondence	16
2.4	Transformation function: thin plate splines	17
2.5	Integrating thin plate splines and correspondence estimation . .	18
2.6	TPS-RPM algorithm	18
3	A novel flexible framework with automatic feature correspondence optimization for non-rigid registration in radiotherapy	21
3.1	Introduction	23

3.2	Materials and methods	25
3.2.1	Patient data	25
3.2.2	Non-rigid registration framework	25
3.2.3	Parameter tuning	31
3.2.4	Transformation error	31
3.2.5	Transformation consistency	32
3.2.6	Correspondence of anatomical features	33
3.2.7	Inclusion of anatomical features in the registration	34
3.3	Results	35
3.3.1	Correspondence filtering	35
3.3.2	Parameter tuning	35
3.3.3	Registration results	36
3.3.4	Anatomical correspondence	39
3.3.5	Inclusion of anatomical features in the registration	40
3.4	Discussion	41
3.5	Conclusion	46
4	A symmetric non-rigid registration method to handle large organ deformations in cervical cancer patients	47
4.1	Introduction	49
4.2	Materials and methods	50
4.2.1	Patient data	50
4.2.2	Surface rendering and smoothing	51
4.2.3	Point generation	51
4.2.4	Theoretical background	52
4.2.5	The symmetric TPS-RPM algorithm	55
4.2.6	Parameter tuning	56
4.2.7	Validation	59
4.3	Results	61
4.3.1	Patient data	61
4.3.2	Surface smoothing	62
4.3.3	Symmetric TPS-RPM vs unidirectional TPS-RPM	62
4.4	Discussion	71
4.4.1	Performance of the novel method and recommendations for further use	71
4.4.2	Limitations and further developments	74
4.5	Conclusions	75

5	Local anatomical changes in parotid and submandibular glands during radiotherapy for oropharynx cancer and correlation with dose, studied in detail with non-rigid registration	77
5.1	Introduction	79
5.2	Materials and methods	79
5.2.1	Patient data	79
5.2.2	Non-rigid registration method	80
5.2.3	Patient data analyses	83
5.2.4	Accuracy of non-rigid registration	84
5.3	Results	85
5.3.1	Volume reduction	86
5.3.2	Local shape and position changes	87
5.4	Discussion	90
5.5	Conclusion	93
6	3D dose addition of external beam radiotherapy and brachytherapy for oropharyngeal patients using non-rigid registration	95
6.1	Introduction	97
6.2	Material and methods	98
6.2.1	Patient data	98
6.2.2	Dose addition	100
6.2.3	Simple alternatives to full 3D non-rigid registration	100
6.2.4	Robustness of dose addition	100
6.3	Results	104
6.3.1	Total dose	104
6.3.2	Perturbations analysis	108
6.4	Discussion	114
6.4.1	Conclusion	117
7	Accurate CT/MR vessel-guided non-rigid registration of largely deformed livers	119
7.1	Introduction	121
7.2	Material and methods	122
7.2.1	Patient data	122
7.2.2	Segmentation and non-rigid registration	123
7.2.3	Validation	131
7.2.4	Rigid registration to estimate the extent of deformation	132
7.3	Results	132
7.4	Discussion	136

7.4.1	Non-rigid registration	136
7.4.2	Future work	140
7.5	Conclusion	140
8	Discussion	143
8.1	Method characteristics and improvements	145
8.1.1	Inclusion of a priori information for registration of multiple structures	145
8.1.2	Inverse consistency	146
8.1.3	Outlier handling	146
8.1.4	Correspondence estimation	147
8.1.5	Point density	147
8.2	Applications in radiotherapy	148
8.3	Method limitations	149
8.4	Similar non-rigid registration methods	151
8.5	Future work	152
8.6	Conclusions	154
	Bibliography	155
	Summary	173
	Samenvatting	181
	Introducción corta y resumen	189
R.1	Radioterapia	191
R.1.1	Precisión del tratamiento y cambios anatómicos	192
R.2	Registro de imágenes	194
R.3	Resumen de esta tesis	195
	Acknowledgements	201
	Curriculum vitae	205
	List of publications	207
	PhD Portfolio	211



Chapter 1

Introduction

1.1. Radiotherapy

Radiotherapy, or radiation therapy, aims to treat cancer and other diseases with ionizing radiation [103, 119]. It works by damaging the genetic material (DNA) of the cells in the area exposed to the radiation. Those cells that cannot repair themselves from the damage are then eliminated by the body. Although healthy cells recover better than cancer cells, both types of cells are damaged by radiation. Therefore, one of the challenges of radiotherapy is to target cancer lesions precisely, while sparing surrounding healthy tissues. Medical images play a key role in achieving this goal which allows localizing the tumor and healthy tissues inside the body of the patient.

The most frequently used imaging modality to localize the tumor and important organs is computed tomography (CT, see figure 1.1(a)). Other common modalities are magnetic resonance (MR) imaging and the combination of Positron-Emission-Tomography and CT (PET/CT). In order to treat a cancer patient with external beam radiotherapy, where high-energy X-rays are

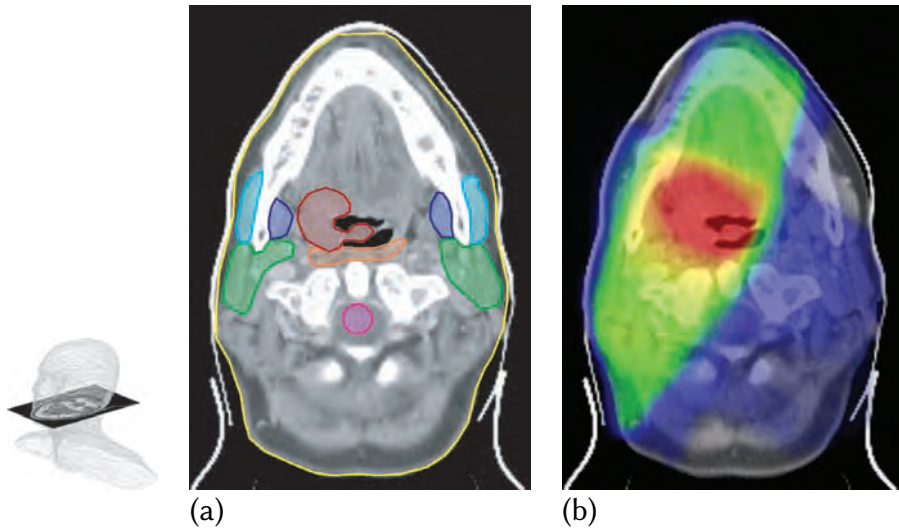


Figure 1.1: CT image of a patient with head and neck cancer. The leftmost image represents the orientation of the slice inside the head of the patient. The CT scan was used to (a) identify the tumor ■, and important organs, such as parotid glands ■, spinal cord ■, constrictor ■, pterygoid ■ and masseter ■ muscles, and (b) to design a radiation therapy treatment plan. In the dose distribution in (b), hot colors indicate a high dose, while cold colors indicate a low dose.

directed to the tumor from outside the body, first a CT scan of the tumor area is acquired. This CT scan is often referred to as planning CT scan. The planning CT is used to demarcate with manually drawn contours the tumor, other areas that are suspected to be affected by the cancer, and important organs that need to be spared from high radiation doses. Other imaging modalities, such as MR imaging and PET/CT can provide additional anatomical and functional information on the tumor and healthy tissue. The tumor and the suspected areas compose the target volume. Second, the planning CT scan and the contoured target and organs are used to design a radiation treatment plan which objective is to damage all cancer cells in the target volume and avoid healthy tissue (see figure 1.1(b)). A radiation treatment plan consists of beams or rays from different directions, aimed at the target volume. The shape of the beams and the radiation intensity across each beam can be optimized such that the obtained distribution of dose, the so-called dose distribution, fulfills the objectives of the treatment. The total radiation dose is then delivered to the patient in daily small amounts, or fractions. This is done to allow healthy cells to recover from the damage caused by the radiation. The total treatment period can range from a couple of days to a couple of weeks. Finally, the patient is followed for several years after the end of the treatment, in order to assess the response of the tumor to the treatment and to monitor potential treatment-related side effects.

In contrast to external beam radiotherapy, tumors can also be treated by placing small radiation sources inside or near the tumor. The sources can either be placed permanently [105] or can be transported in and out the body by implanted tubes or catheters. This treatment modality is called brachytherapy. External beam radiotherapy and brachytherapy are often combined, where the latter technique is used to deliver an extra high dose to the primary tumor.

1.1.1. Treatment precision and anatomical changes

To minimize the damage to the tumor's healthy surroundings, radiation treatments require high precision. This includes positioning the patient before every treatment fraction in the same way as during the acquisition of the planning CT. However, the anatomy of the patient can change during the treatment, for example due to variations in bladder, bowel and stomach filling, tumor regression, inflammation, and weight loss (see figure 1.2). As a consequence, areas that were planned to receive a high dose, such as the tumor, may receive a lower dose, and areas that were planned to receive a low dose, such as healthy organs, may receive a higher dose [89, 30, 49, 71, 74, 4]. In order

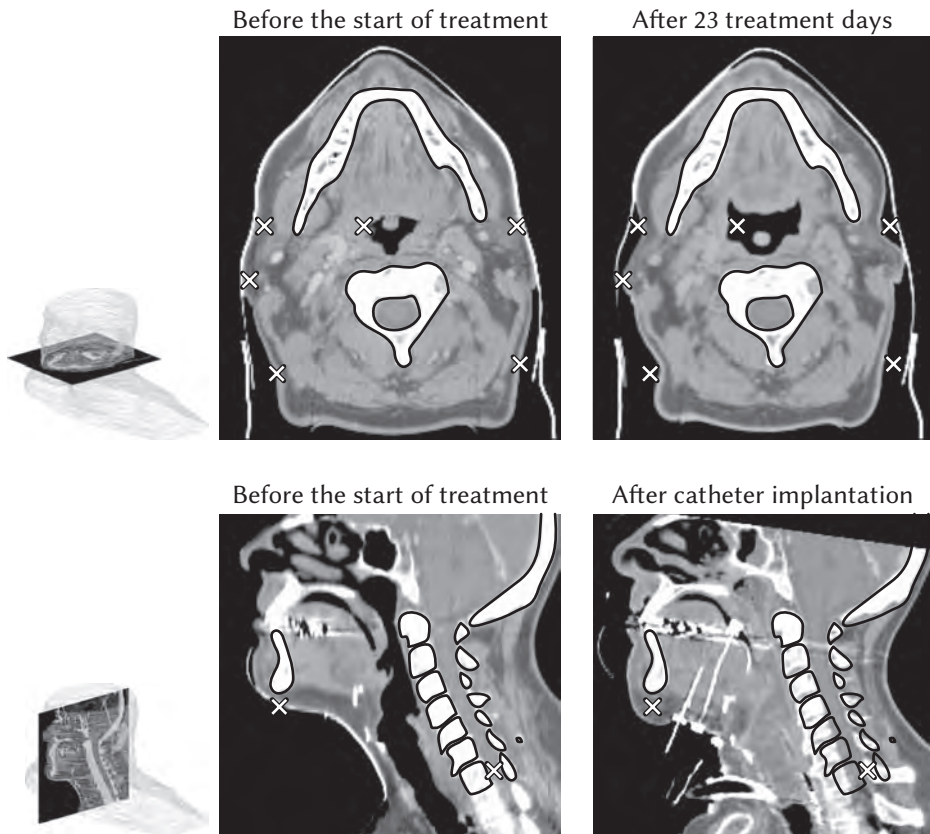


Figure 1.2: Changes in the anatomy of a patient as observed in CT images. The first row shows changes due to weight loss and tumor shrinkage after 23 treatment days. The second row shows changes due to the implantation of catheters for brachytherapy. Anatomical changes are pointed out by crosses. The contours represent the mandible, spine and skull from the CT acquired before the start of the treatment.

to improve radiation treatments, these anatomical changes should be taken into account, for example by means of image registration.

1.2. Image registration

Image registration generally refers to the process of identifying corresponding elements from two images often of the same subject, and subsequently finding a transformation T that maps these corresponding elements [90, 23,

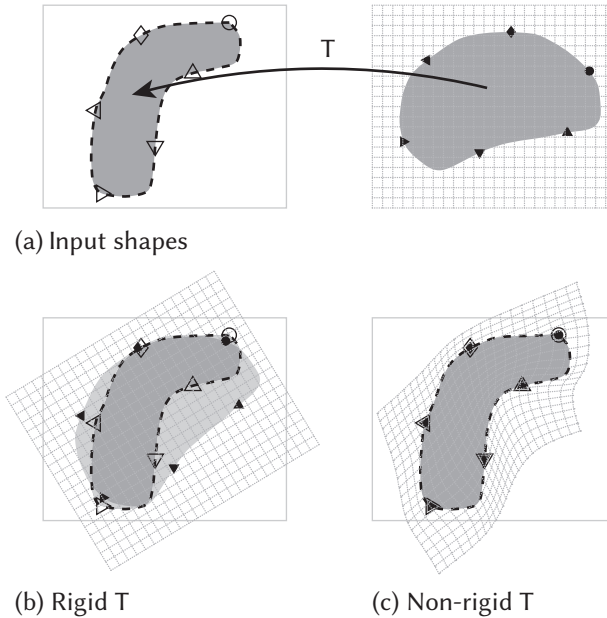


Figure 1.3: Registration of two simple shapes. The aim is to first identify corresponding elements in the two images (depicted as circles, triangles, etc.) and then to find a transformation T , which aligns these corresponding elements. (a) Input images showing an object which shape changed. (b) If T is rigid, the transformation is limited to rotations and translations. A global alignment can be achieved, but local details are not completely aligned (light grey area). (c) if T is non-rigid then local details can be properly mapped.

150]. Depending on the transformation type that is used, the registration can be either rigid or non-rigid. Rigid registrations allow only rotations and translations to align the images, which is sufficient as long as the shape of the subject does not deform. However, if the shape of the subject deforms, as is the case in the example depicted in figure 1.3, rigid registration may align the images globally, but misalignments on a local scale cannot be avoided (see light grey areas in figure 1.3(b)). Non-rigid registration has the potential to align local details, as shown in figure 1.3(c).

One way to register the elements in the two images is by using the intensity values of the image voxels¹ [126, 21, 37, 87]. If two images of the same modality are registered, for example two CT scans, the voxels of a given organ are assumed to have similar intensities in both scans. Therefore, the

¹a voxel is a single point in a 3D image.

registration aims to align areas of similar intensity values. If images from different modalities are registered, for example a CT and a MR image, the voxels of a given organ may have different intensity values. Thus, the registration aims to align areas with similar patterns, but not necessarily similar intensity values. Intensity-based registration is often used to align medical images, however the results depend strongly on the quality of the used images, and it is limited if the contrast between different structures or organs is very low or if large artifacts are present in the images. To overcome these problems, approaches using specific features in the image rather than the intensity values themselves can be used instead [133, 63, 50, 13, 113, 84]. These features can be anatomical landmarks, implanted markers or delineated organs (see for examples figure 1.1a). The problem is then translated to finding the correspondence between the features and aligning the corresponding features.

1.3. This thesis

This thesis describes the improvements of a feature-based non-rigid registration method that were essential for its application in radiotherapy. In addition, this thesis presents three practical applications of the improved method. The following sections briefly introduce the method improvements and the investigated applications.

1.3.1. Non-rigid registration method

The method is point-based, meaning that the structures to be registered are represented by two sets of points. The method iteratively estimates point correspondence between the two sets and updates a non-rigid transformation modeled by a thin-plate spline. It was originally proposed by Chui and Rangarajan [25, 23] and among its advantages is its robustness against noisy data. In chapter 2, a summary of the original method is given for sake of completeness. Chapters 3 and 4 of this thesis describe the essential method improvements developed to make it applicable in the field of radiotherapy. The first major improvement on the original method was to extend it to allow multiple organs or structures to be registered simultaneously, and to include user-defined landmarks, lines, and surfaces inside and outside of the structures to be registered [133]. Chapter 3 contains the technical details of these improvements, and results are presented for three sites with different degrees of deformation: head and neck, prostate, and cervix.

The second major change was to improve the inverse consistency of the method. The original method was unidirectional, i.e. in order to calculate a ‘back-transformation’, the whole registration had to be executed again after reversing the roles of the point sets. For unidirectional registration methods, the quantified anatomical changes can be asymmetric, i.e., the registration results depend on the direction of the registration. Especially, the registrations of large and complex organ deformations resulted in inconsistent transformations. The method was improved, such that it enforces consistency by calculating transformations for both directions simultaneously based on a common correspondence [7]. Chapter 4 describes in detail this modification and presents results for deformations of uterus-cervix and bladder for cervix cancer patients.

1.3.2. Applications in radiotherapy

Chapters 5, 6 and 7 describe three successful applications of the improved non-rigid registration method within the domain of radiotherapy. The applications are: 1) quantification of anatomical changes in 3D for head and neck cancer patients, 2) addition of dose distributions of two radiation treatment modalities for head and neck patients and 3) alignment of CT and MR scans of the liver by automatically segmenting and registering vessels.

Anatomical changes in head and neck cancer patients

Shape and position changes of the salivary glands and tumor were tracked for ten oropharyngeal cancer patients, and the results are presented in chapter 5. Non-rigid registration generates information in full 3D, which allows identifying areas where changes are more or less pronounced. Using this information, patterns in deformation were identified in the group of patients studied. This approach can be used for modeling organ deformation in larger patient populations [132, 129]. Organ deformation models can then be used to improve the radiation treatments [45].

Dose addition

Radiation treatment modalities can be combined, for example to deliver extra dose to the primary tumor. However, in current clinical practice, each treatment plan is optimized and evaluated independently, without taking into account the dose delivered to the patient by the other treatment modalities. In chapter 6, a method to add dose distributions from two modalities in

the presence of anatomical changes is presented and validated. Non-rigid registration was used to account for anatomical changes, and an analysis of perturbations was used to assess the robustness of the dose addition method.

Automatic segmentation and registration of vessels in the liver

Tumors in the liver are often better visible in MR images compared to CT scans [95]. However, CT images are used to design the treatment plan. Differences in the patient anatomy, recorded in the CT and MR images, hinder the alignment and integration of these images. Chapter 7 describes the use of the non-rigid registration method to align largely deformed livers in CT and MR scans guided by automatically segmented vessels. A direct clinical application is to use the CT-MR alignment to improve the localization of tumors in the liver for stereotactic body radiotherapy.



Chapter 2

Non-rigid point based registration. A summary of the original method

2.1. Introduction

For the sake of completeness, a summary of the original method is included in this thesis. The thin plate spline - robust point matching (TPS-RPM) was proposed by Chui and Rangarajan [23, 25]. The framework was built upon previous work for computer vision and pose estimation [24, 44, 43].

The registration method is point-based, meaning that the structures to be aligned are represented by points. When matching point sets, two problems need to be solved: the correspondence between the points, and subsequently the aligning or transformation between the corresponding points. Solving the correspondence and the transformation simultaneously is difficult, if not impossible. However both problems have an optimal and straightforward solution when one of them is held fixed. It is much easier to estimate the non-rigid transformation once the correspondences are known. But, in order to estimate plausible correspondences, a reasonable transformation is required. This fact is the base of the TPS-RPM approach: an alternating estimation of the correspondence and the transformation.

The rest of this chapter is organized as follows. First, point registration is formally defined. Then in section 2.3, the solution of the correspondence problem is described assuming a general transformation function f . Next, the thin-plate splines is introduced and integrated with the correspondence in section 2.4. The chapter concludes with the TPS-RPM algorithm.

2.2. Definition of point registration

Suppose we have two point sets, $X = \{x_i, i = 1, \dots, n_x\}$ and $Y = \{y_j, j = 1, \dots, n_y\}$. The aim of the registration, is to align the points in the sets X and Y using a transformation function f , such that the distances between the points in the sets is minimum while guaranteeing a ‘natural’ function f (see figure 2.1). This can be formulated as a minimization problem:

$$\min_{M,f} E(M, f) = \min_{M,f} \sum_{i=1}^{n_x} \sum_{j=1}^{n_y} m_{i,j} \|x_i - f(y_j)\|^2 + \lambda \|L(f)\|^2, \quad (2.1)$$

where E represents the energy, $m_{i,j}$ the correspondence between point x_i and y_j (see section 2.3), $\|L(f)\|^2$ measures the *smoothness* of the transformation function f by using the operator L , λ is a weight parameter that constrains the transformation function f (see section 2.4) and the correspondence matrix

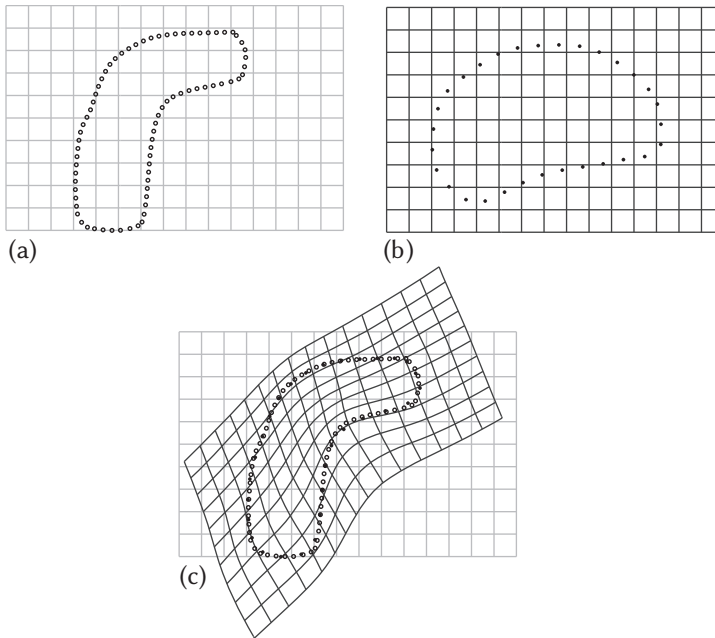


Figure 2.1: Example of a non-rigid registration. The objective of the registration is to find the correspondence between the points and the transformation function, such that the input points are properly aligned. (a) and (b) Input shapes to be registered. (c) Overlap between transformed shape in (b) and reference shape in (a)

M is different than zero (trivial solution). The first term of equation 2.1 estimates the distances between corresponding points, while the second term helps constraining the transformation function f .

2.3. Correspondence

The correspondence between two point sets, X and Y , can be represented with a matrix M , where a value of one in the entry m_{ij} indicates correspondence between x_i and y_j , and zero indicates no correspondence. When the point sets match ‘exactly’, i.e. $n_x = n_y$, this correspondence matrix is a permutation matrix that has exactly one entry ‘1’ in each row and each column, and zeros elsewhere. Finding the correspondence between the points by brute force would require evaluating $N!$ permutations, which leads to a combinatorial explosion. For moderately large number of points, solving the correspondence problem can be solved using the hungarian algorithm [70]. However, the

hungarian algorithm assumes that the points are already optimally aligned. A common approach to solve combinatorial optimization problems, such as the correspondence problem, is to relax the discrete problem to a continuous problem; that is to relax the binary correspondence to a fuzzy correspondence.

2.3.1. Fuzzy correspondence using softassign

Relaxing the binary correspondence to a fuzzy correspondence while enforcing the row and column constraints is known as softassign [43]. The values of each entry $m_{i,j}$ in the correspondence matrix are not constrained to be zero or one, but they are allowed to take a value in the interval $[0, 1]$. However, the rows and columns of the correspondence matrix are constrained to add up to one, as in the discrete case. The correspondence between point x_i and y_j , i.e. the value of $m_{i,j}$, is calculated using equation 2.2.

$$m_{i,j} = e^{-\frac{\|y_j - f(x_i)\|^2}{T}}, \quad (2.2)$$

where T is a temperature parameter (see section 2.3.3), and f is the transformation function. For details on the derivation of equation 2.2, please refer to [23, 43].

Equation 2.2 results in a value close to one when the points are very close together, and it reduces exponentially with the distance between the points, up to a point where it is almost zero. Notice, however, that using equation 2.2 to calculate the entries of the correspondence matrix, does not necessarily result in a matrix whose rows and columns sum up to one. The algorithm proposed by Sinkhorn [117] can be used to ensure this constraint. The algorithm normalizes the rows and columns iteratively until convergence, i.e. each row/column element is divided by the total sum of all row/column elements, until the sum of the rows/columns equals 1.

Notice that as a consequence of the correspondence relaxation, one point does not necessarily correspond to only one other point; it could have multiple possible matching partners, giving some preference to closer points. This characteristic also helps when dealing with noisy data, and when $n_x \neq n_y$.

2.3.2. Handling outliers

Outliers are points that do not have a counterpart in the other set. When outliers are present in the input sets, the correspondence problem is even more complex; besides finding the corresponding points, the algorithm should also

identify outliers. In order to handle outliers, an outlier ‘cluster’ is introduced in the correspondence model. The outlier cluster works like a garbage collector: any point rejected by all possible partners is then labeled as an outlier.

The outlier cluster is implemented by attaching an additional row and column to the correspondence matrix. The outlier row and column participate in the row/column normalization. However, the outlier row and column are not restricted to sum up to one, since more than one outlier is usually present; and their totals yield an estimate of the number of outliers in the sets. As the correspondence matrix is calculated, all points are suspected to be outliers, i.e. a large value is set in the entries of the outlier row and column. For points that have been rejected by all points in the other set, the $m_{i,j}$ values are close to zero. After the row and column normalization, the entry in the outlier row or column becomes close to one, and therefore, the point is identified as an outlier.

2.3.3. Back from fuzzy to discrete correspondence

Inside equation 2.2, there is the temperature term T . T allows to control the level of fuzziness of the correspondence. Large T generates $m_{i,j}$ values that are barely influenced by the distance between the points. Conversely, low T values are mostly influenced by the distance between points, resulting in zero correspondence if the points are far apart, and large values if the points are near to each other. By controlling T , an iterative strategy for refining the correspondence can be implemented. In the first iteration, T is set to a large value T_0 , therefore the correspondence $m_{i,j}$ between the points x_i and y_j is barely influenced by their distance. In this early stage, all points are allowed to correspond weakly to each other. Using the correspondence matrix, a transformation function f is calculated. In the next iteration, the temperature T is decreased, and the distance between points starts to influence slightly more the correspondence. With this new correspondence a new f is calculated. With each new iteration, T is reduced further, and the distance starts to dominate the correspondence $m_{i,j}$, to finally allow only points that are in a close proximity to correspond. This iterative process is called deterministic annealing [144, 127, 52, 41].

In other words, by reducing T in the iterative process, the correspondence evolves from very fuzzy to discrete. If the temperature is brought to be very close to zero, the correspondence is completely discrete. If noise is present in the point sets, T is not forced to reduce close to zero, but it is kept slightly higher at T_{final} . The reduction of the temperature T is set as $T_{\text{new}} = T_{\text{old}} \times r_a$, where r_a is the annealing rate, which is commonly set between 0.5 and 0.99.

2.4. Transformation function: thin plate splines

In interpolation theory, splines have been used since 1946 [115]. Splines have been broadly used to interpolate statistical data and to fit curves to data samples, which assures that the interpolation function is kept smooth [136]. Several criteria can be used to measure the smoothness of the transformation function (second term of equation 2.1). In particular, when the volume integral of the square of the second order derivatives of the transformation function is chosen to measure the function smoothness, the natural solution is the thin-plate splines (TPS, [136, 10]).

The TPS fits a mapping function f between landmarks pairs (p_i, q_i) , where $i = 1, \dots, n$, by minimizing the following energy function:

$$\begin{aligned}
 E_{\text{TPS}} = & \sum_{i=1}^n \|p_i - f(q_i)\|^2 + \\
 & \lambda \int \int \int \left(\frac{\partial^2 f}{\partial x^2} \right)^2 + \left(\frac{\partial^2 f}{\partial y^2} \right)^2 + \left(\frac{\partial^2 f}{\partial z^2} \right)^2 + \\
 & 2 \left(\frac{\partial^2 f}{\partial x \partial y} \right)^2 + 2 \left(\frac{\partial^2 f}{\partial x \partial z} \right)^2 + 2 \left(\frac{\partial^2 f}{\partial y \partial z} \right)^2 dx dy dz \quad (2.3)
 \end{aligned}$$

For a fixed value for the regularization parameter λ , there exists a unique function f that minimizes equation 2.3:

$$f(x) = \sum_i^n c_i \|x - x_i\| + x \times d, \quad (2.4)$$

where c_i are the warping coefficients representing the non-rigid part of the transformation and d is a matrix representing the affine part of the transformation. The function f maps every point p_i onto the point q_i . Solving equation 2.3 with respect to c and d results in a system of linear equations, which can be solved using QR decomposition [25, 136, 10].

In equation 2.3, the parameter λ is used to regularize the resulting TPS function. Large λ values restricts the transformation to be mostly affine and as a consequence, a global alignment is found between the point sets. For low λ values, the transformation is mostly non-rigid and as a consequence, details can be fit more accurately.

2.5. Integrating thin plate splines and correspondence estimation

As mentioned in section 2.4, the TPS fits a function f between known landmarks pairs. The problem, is that the number of points in X and Y may be different, and therefore, a TPS cannot always be fitted. Using the correspondence matrix M , a set Q of virtual corresponding points can be generated using equation 2.5. Then a TPS function is fitted to X and Q .

$$q_i = \sum_{j=1}^{n_y} m_{i,j} y_j \quad (2.5)$$

Additionally, by including T in the penalization term of the energy function 2.1, a refining strategy for the transformation function can be implemented ($\lambda \|L(f)\|^2$ becomes $\lambda T \|L(f)\|^2$). As mentioned in section 2.4, a large λ value constraints the transformation to be mostly affine. Therefore, progressively reducing T , the transformation function evolves from being mostly affine, such that a global alignment can be achieved, to become more non-rigid in order to align local details.

2.6. TPS-RPM algorithm

The individual elements of the method were described in the previous sections. Figure 2.2 shows different iterations of the non-rigid registration procedure for the example in figure 2.1. In the top row, the evolution of the correspondence scope is shown. Similarly, in the bottom row, the evolution of the transformation is depicted.

To conclude this chapter, the TPS-RPM is summarized in algorithm 1. In the algorithm two loops can be distinguished. The outer loop implements the deterministic annealing explained in section 2.3.3. The inner loop allows the correspondence and transformation to converge for a certain temperature. In many applications, the inner loop generates convergent results when it is executed for a fixed number of iterations, Chui and Rangarajan [25] recommended to use 5 iterations.

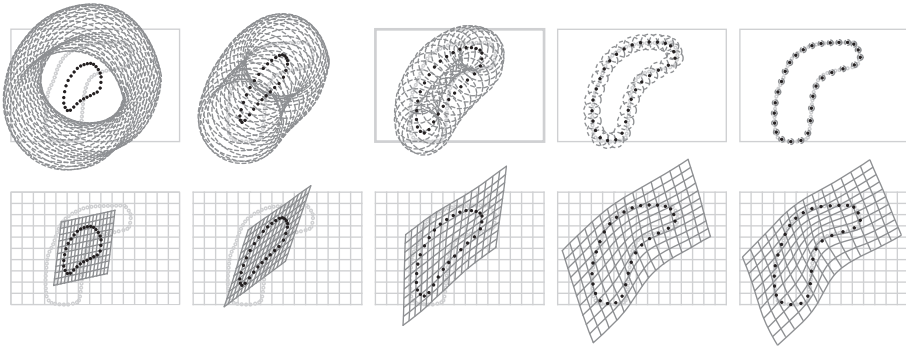


Figure 2.2: Example of the non-rigid registration process using two simple shapes, represented by circles and stars. The top rows depicts the evolution of the correspondence scope during the registration. For each star, a circle of radius \sqrt{T} is drawn. The circles represent the area in which points establish strong correspondence. The bottom row shows the evolution of the TPS transformation function during the registration. Notice that the transformation is mostly affine (rotation, translation, scaling and shearing) in the first iterations, and it is more non-rigid in the last iterations.

Algorithm 1 TPS-RPM algorithm

Initialization

$f \leftarrow$ identity transformation

$T \leftarrow T_0$

while $T > T_f$ **do**

▷ Deterministic annealing

repeat

 ▷ Alternating Update

 Update the correspondence matrix M using equation 2.2

 Normalize rows and columns using Sinkhorn algorithm

 Calculate virtual corresponding points Q using equation 2.5

 Find TPS f in equation 2.4 that fits X and Q using λT

until maximum number of iterations is reached

$T \leftarrow T \times r_a$

end while



Chapter 3

A novel flexible framework with automatic feature correspondence optimization for non-rigid registration in radiotherapy

Eliana M. Vásquez Osorio, Mischa S. Hoogeman, Luiza Bondar,
Peter C. Levendag and Ben J. M. Heijmen

Published in
Medical Physics
Vol. 36, No. 7, pp. 2848-2859, 2009

Abstract

Technical improvements in planning and dose delivery and in verification of patient positioning have substantially widened the therapeutic window for radiation treatment of cancer. However, changes in patient anatomy during the treatment limit the exploitation of these new techniques. To further improve radiation treatments, anatomical changes need to be modeled and accounted for. Non-rigid registration can be used for this purpose. This paper describes the design, the implementation and the validation of a new framework for non-rigid registration for radiotherapy applications. The core of this framework is an improved version of the Thin Plate Splines Robust Point Matching (TPS-RPM) algorithm. The TPS-RPM algorithm estimates a global correspondence and a transformation between the points that represent organs of interest belonging to two image sets. However, the algorithm does not allow for the inclusion of prior knowledge on the correspondence of subset of points and therefore, it can lead to inconsistent anatomical solutions. In this paper TPS-RPM was improved by employing a novel correspondence filter that supports simultaneous registration of multiple structures. The improved method allows for coherent organ registration and for the inclusion of user defined landmarks, lines and surfaces inside and outside of structures of interest. A procedure to generate control points from segmented organs is described. The framework parameters r and λ , which control the number of points and the non-rigidness of the transformation respectively, were optimized for three sites with different degrees of deformation: head and neck, prostate and cervix, using two cases per site. For the head and neck cases, the salivary glands were manually contoured on CT-scans, for the prostate cases the prostate and the vesicles, and for the cervix cases the cervix-uterus, the bladder and the rectum. The transformation error obtained using the best set of parameters was below 1 mm for all the studied cases. The length of the deformation vectors were on average (± 1 standard deviation) 5.8 ± 2.5 and 2.6 ± 1.1 mm for the head and neck cases, 7.2 ± 4.5 and 8.6 ± 1.9 mm for the prostate cases, and 19.0 ± 11.6 and 14.5 ± 9.3 mm for the cervix cases. Distinguishable anatomical features were identified for each case, and were used to validate the registration by calculating residual distances after transformation: 1.5 ± 0.8 , 2.3 ± 1.0 and 6.3 ± 2.9 mm for the head and neck, prostate and cervix sites respectively. Finally, we demonstrated how the inclusion of these anatomical features in the registration process reduced the residual distances to 0.8 ± 0.5 , 0.6 ± 0.5 and 1.3 ± 0.7 mm for the head and neck, prostate and cervix sites respectively. The inclusion of additional anatomical features produced more anatomically coherent transformations without compromising the transformation error. We concluded that the presented non-rigid registration framework is a powerful tool to simultaneously register multiple segmented organs with very different complexity.

3.1. Introduction

Modern radiation treatment (RT) techniques allow for planning and delivery of complex dose distributions, making an increase of the dose to target volumes and a better sparing of normal tissue possible. However, anatomical changes in patients limit the benefits of these techniques. For example, tumor shrinkage, organ deformation and internal motion introduce deviations between the planned and actually received dose, potentially causing underdosage of the target volumes and overdosage of organs at risk [89, 30, 49, 71, 74, 4]. Thus, in order to fully exploit the advantages of modern RT techniques, anatomical changes need to be managed, among others by tracking them using non-rigid registration techniques. In non-rigid registration, two data sets (such as computed tomography (CT) scans, magnetic resonance imaging (MRI) scans, etc...) are aligned by finding a correspondence and a non-rigid transformation between elements in the two sets [90, 150, 67]. The computed transformation can be used to investigate and assess organ motion and deformation [132, 46], to determine suitable margins that encompass the whole extent of organ motion [93, 129], to perform automatic segmentation or delineation [99, 16, 56, 107, 101] and to map dose distributions to a common frame of reference [101, 147].

One way to register the elements in the two data sets is by using the intensities in the images (CT or MRI scans) [126, 21, 37, 87]. Unfortunately, the use of intensity-based non-rigid registration is limited by poor contrast between different structures or organs (especially for CT scans), the presence of artifacts in the images and the absence of overlap between structures in the reference and the deforming set. To overcome these problems, approaches using specific features in the image rather than the intensity values themselves are often used [63, 50, 13, 113, 84]. In general, these features are segmented by hand or automatically following the intensity gradients wherever possible. Most feature-based approaches rely on correspondence defined beforehand between features, either manually or automatically. The most common approach is to use single points, or landmarks, representing the same features in the two scans. Manual localization of landmarks is a tedious work and prone to errors, which in practice translates to a limited number of landmarks being identified. There are also attempts to automatically identify landmarks, for example, by automatically identifying curvatures [13, 50]. However, this approach is not feasible in structures or organs with large deformations where no clear curvatures can be identified or are conserved.

We propose a novel approach, or framework, for non-rigid registration in

which correspondence is automatically estimated and optimized. Furthermore, the framework supports multiple structures being registered simultaneously and allows the inclusion of user-defined landmarks or even features such as lines or surfaces inside and outside the structures of interest. The heart of this approach is an improved version of the non-rigid registration method originally presented by Chui et al. [25], which formulates feature-based non-rigid registration as a non-rigid point matching problem. The original non-rigid registration method automatically estimates the correspondence between the points in two sets, i.e. the *reference* and the *deforming* set, and based on the estimated correspondence, calculates a non-rigid transformation function. The correspondence and the transformation between the point sets are iteratively optimized. Note that in the original method, the correspondence estimation is global, allowing all points in the sets to correspond among each other. In other words, it does not allow to include knowledge on the correspondence between subsets of points, for example subsets representing the same structure or organ. We solved this issue by introducing a filter that eliminates correspondence between points belonging to different structures, and thereby adapted the method to produce a global transformation for multiple structures. Furthermore, this filter also made possible the inclusion of selected points or lines representing anatomical features whose correspondence is known beforehand. The non-rigid transformation obtained can be applied to any point, allowing the transformation of any spatial data such as CT- images and dose distributions.

This framework has been successfully used in two recent studies. The first study quantified treatment-related local anatomical changes in a group of 10 oropharynx cancer patients [132]. A second study analyzed the deformation of the prostate and the seminal vesicles in prostate cancer patients to investigate the potential margin reduction allowed by on-line corrections based on intraprostatic fiducial markers [129].

In the current paper, the framework for non-rigid registration is fully described, tested and anatomically validated. Within this scope, it was applied to three sites commonly treated with radiotherapy presenting different degrees of deformation: head and neck, prostate and cervix. The framework parameters r , which regulate the number of control points, and λ , which controls the non-rigidity of the transformation, were optimized for the three sites, using two cases per site. The accuracy of the registration was assessed by different measures: the distance between the reference and transformed surfaces as an estimate of the transformation error, and the difference between the back-

transformation and forth-transformation as an estimate of the transformation consistency. To validate the correspondence, anatomical landmark points and lines were identified for the different cases in the reference and deforming images, and their mismatch after the registration was measured. Finally, we demonstrated the flexibility of the framework by including these landmark points and lines in the registration process, to produce more anatomical coherent transformations.

3.2. Materials and methods

3.2.1. Patient data

In order to illustrate the versatility of the framework, three sites with different degrees of deformation were included in this study. A total of six example cases were analyzed, two cases per site. For each case two CT scans were used. The CT scans were pre-matched using bony anatomy in the region of interest. The structures of interest were manually delineated on axial CT scans. To obtain consistent contours in the CT scans pairs, the CT scan first contoured was used as a reference to delineate the second scan, and all contours were reviewed by a second observer.

For two oropharynx cancer patients, two CT scans were used: the scan used for planning and a repeat scan after 46 Gy, both acquired with intravenous contrast. The structures of interest were the parotid and submandibular glands. For two prostate cancer patients, two CT scans were used: the scan used for planning and a repeat scan. In each scan, the prostate and vesicles were manually delineated and merged into a single structure. The patients had four gold markers implanted in their prostate. For one cervix patient, three CT scans were acquired at different treatment days. In one CT scan the bladder was full, in another partially filled and in the last one empty. The bladder filling changes induced large deformations of the cervix-uterus. We defined two example cases: (1) partially filled vs. empty and (2) partially filled vs. full. The structures of interest were the bladder, the rectum and the cervix-uterus.

3.2.2. Non-rigid registration framework

The framework contains a method for generating control points from segmented structures and the non-rigid registration method, which was modified to handle multiple structures. Figure 3.1 shows a schematic of the framework. The following sections describe each of the framework components in detail.

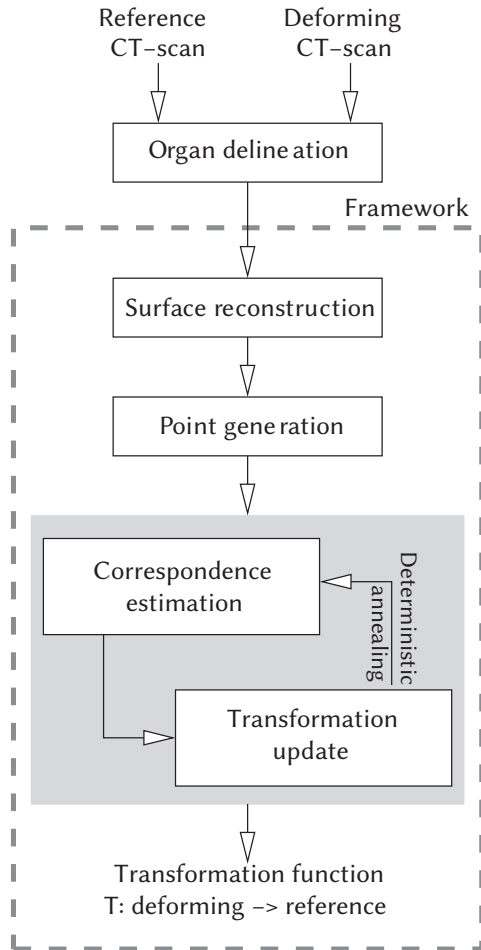


Figure 3.1: Schematic of the framework. The components of the framework are enclosed by a dashed line. The heart of the framework is the non-rigid registration method presented in the gray area.

Generation of control points

Surfaces for each structure of interest were built by joining contours in consecutive slices with triangles. The points defining the triangles of the surfaces lie on consecutive planes, i.e. the axial CT slices. In the axial planes, the contour points do not follow any particular distribution. The heterogeneous point distribution in the space is not desirable in the non-rigid registration

process, since the correspondence between irregularly spaced points can be problematic and error prone, and the thin plate splines work better when homogeneous or pseudo-homogeneous points are used [145]. Therefore, new points pseudo-homogeneously spread on the triangles were generated. Figure 3.2 illustrates the process for a simple case. First, triangles that degenerated to lines or points (two or more points are at the same xyz-position) were removed. Then, the triangles defining the surface were refined (figure 3.2(b)). The triangles with an edge length larger than a given threshold were divided in two triangles. The edge dividing procedure was recursively repeated until all the triangles had their edge length smaller than the threshold. We used threshold values of 1.5, 1.5 and 3 mm for the head and neck, prostate and cervix cases, which resulted in a surface with triangles of roughly uniform size. A small threshold value is required to produce a pseudo-homogeneous point distribution. However, due to the small threshold value, the number of points exceeded the available computational resources. Therefore, we reduced the number of points using an iterative procedure. In this procedure, first a starting point is chosen to be the center of a sphere with radius r (figure 3.2(c)). All points that lie inside the sphere are replaced by the centroid of these points. The procedure is repeated with the remaining points until there are no more points left. The set of centroids is then used as control points (figure 3.2(d)). The radius of the sphere r , determines the density of the resulting point set and consequently the number of control points. The described process was applied to each structure separately.

Non-rigid registration method

The original method, known as TPS-RPM and developed by Chui et al. [25], formulates feature-based non-rigid registration as a non-rigid point matching problem. The goal is to find an optimal correspondence and transformation between two point sets, namely the reference point set, containing n points, and the deforming point set, containing k points. Note that n and k are usually different, and a one-to-one correspondence between the points is not expected.

Solving the correspondence and the transformation simultaneously is difficult, if not impossible. However both problems have an optimal solution when one of them is held fixed. Therefore the use of an iterative scheme is suitable. The process starts by estimating the correspondence between the point sets. Next, based on the estimated correspondence, the non-rigid transformation is calculated, and then applied to the deforming point set. A new iteration starts by estimating the correspondence between the newly

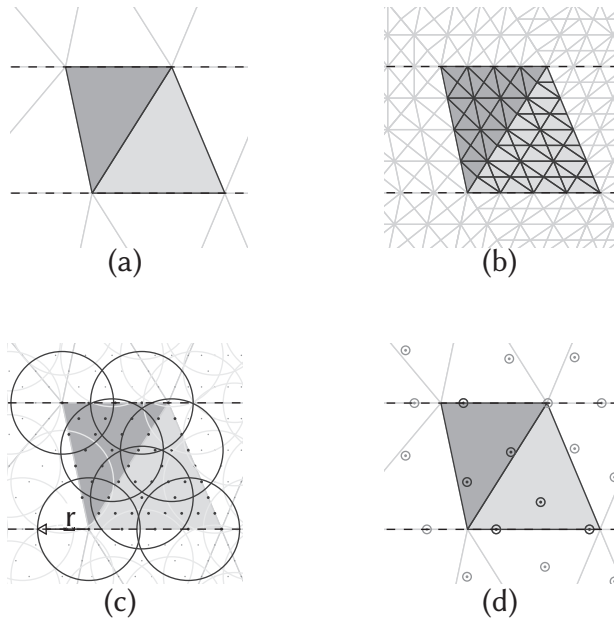


Figure 3.2: Schematic showing the process to generate control points on a small part of a surface. Dashed lines represent the contours on two consecutive slices. (a) Triangles joining the original contours points. (b) Refined triangles. (c) Spheres used to group points using density radius r . (d) Generated control points shown as dotted circles.

transformed deforming points and the reference point set, after which the transformation is recalculated. The process is driven by a numerical technique known as deterministic annealing, which helps to avoid local minima. The annealing technique introduces a temperature variable T which starts at a high value (T_{initial}), and decreases over time using an annealing rate ($T_k = r_a \times T_{k-1}$), until it reaches a final temperature T_{final} . The common range for the annealing rate r_a is between 0.9 and 1. We used r_a equal to 0.93 in our current implementation [23].

Since the number of points in the two point sets is usually not the same, the correspondence between the different points is not binary (or one-to-one), but fuzzy. The fuzzy correspondence [106, 137] allows a point in the deforming set to correspond to more than one point in the reference set and vice versa. In the current implementation a technique called soft-assignment was used [43]. The correspondence is represented by an $n \times k$ matrix m , where the value of $m_{i,j}$, $i = 1..n$ and $j = 1..k$, represents the degree of correspondence between two points p_i and q_j in the reference and deforming set respectively. The values in

m are restricted to be between zero and one. A value $m_{i,j}$ close to zero stands for a weak correspondence between points p_i and q_j . A value $m_{i,j}$ close to one represents a strong correspondence between points p_i and q_j . The values $m_{i,j}$ depend on the distance between the points and the current temperature value T (see figure 3.3). In the first iterations the temperature T is high and the correspondence $m_{i,j}$ between the points p_i and q_j is barely influenced by the distance between each other (see highest temperature figure 3.3). In these early stages, all points are allowed to weakly correspond to each other. With each new iteration the temperature T is decreased and the distance between points starts to dominate the correspondence, to finally allow only points that are in a close proximity to correspond (lowest temperature in figure 3.3). We refer to Chui et al. [25, 23] for details about computing m .

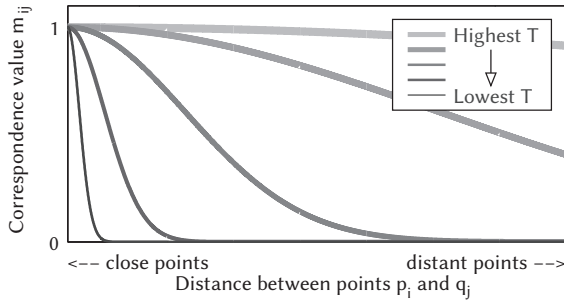


Figure 3.3: Schematic showing the relation between correspondence and distance with varying temperature. The distance between two points p_i and q_j , belonging to the reference and deforming control points set respectively, is (schematically) shown on the horizontal axis. The correspondence value between these points, $m_{i,j}$, is shown on the vertical axis. Note that the correspondence value is barely influenced by the distance between the points when the temperature is high (thick and light line), while it decreases rapidly with the distance for low temperatures.

Since no binary one-to-one correspondence is expected to exist between the two point sets, the temperature is not decreased to zero, as in conventional annealing schemes. Instead, the final temperature T_{final} is equal to the mean square distance between the nearest neighbors of the *deforming* points [23]. The initial temperature T_{initial} should be high enough to allow all points in the two point sets that belong to the same structure to correspond to each other. In this implementation, T_{initial} was set to be the length of the diagonal of the box that bounds the largest structure.

The non-rigid transformation is modeled by thin plate splines (TPS, [25,

23]). To determine the transformation function the following energy function is minimized:

$$\min_f E(f) = \min_f \sum_{j=1}^k \|y_j - f(q_j)\|^2 + \lambda T \|Lf\|^2 ,$$

where $y_j = \sum_{i=1}^n m_{i,j} p_i$, $m_{i,j}$ is the correspondence matrix, p_i are the reference points ($i = 1..n$), q_j are the deforming points ($j = 1..k$), λ is a weight parameter, T is the current temperature of the deterministic annealing, and $\|Lf\|^2$ is the smoothness measure of f using the operator L . When the space integral of the square of the second order derivatives of f is used as the operator L , the function that minimizes the energy function is a TPS, in the form

$$f(x) = \phi(x) \cdot c + x \cdot d ,$$

where c is a $k \times 4$ matrix of warping or non-rigid coefficients, d is a 4×4 affine matrix and $\phi(x)$ is a $1 \times k$ vector related to the TPS kernel [10, 136]. Each element of $\phi(x)$ is related to the point q_j , by $\phi_j(x) = \|q_j - x\|$. The weight parameter λ controls the degree of deformation of the transformation function, and it is annealed using the general annealing rate ($\lambda_k = r_a \times \lambda_{k-1}$). By annealing λ , it is possible to obtain a registration from a mainly affine transformation to a non-rigid one gradually. We refer to Chui et al. [25, 23] for further details.

Correspondence filtering

All structures are registered simultaneously. Note that points of different structures that lie in close proximity may develop a high correspondence during the process. An incorrect correspondence would misguide the transformation leading to unacceptable results. To avoid any correspondence between points of different structures, the correspondence matrix m was replaced by a filtered matrix m_{filtered} defined by

$$m_{i,j}^{\text{filtered}} = \begin{cases} m_{i,j} & \text{if } p_i \text{ and } q_j \text{ belong to the same structure,} \\ 0 & \text{otherwise.} \end{cases}$$

In order to implement this filtering, we associated to each point an index that defined the structure it belongs to. The condition “*belong to the same structure*” was simply tested by checking whether $\text{index}(p_i)$ was the same as $\text{index}(q_j)$.

Forth-transformation and back-transformation

Every registration included two transformations, a forth-transformation (fT) and a back-transformation (bT). The forth-transformation is found by registering the deforming set to the reference set. Likewise, the back-transformation is calculated by reversing the role of the points, and registering the reference set to the deforming set. The average length (and standard deviation) of the deformation vectors was calculated and reported. To limit the number of values reported and increase readability, the length of the vectors of the back-transformation and forth-transformation was averaged.

3.2.3. Parameter tuning

Two important parameters in the non-rigid registration framework are the density radius r for the generation of the point set (figure 3.2) and the initial value of λ used to calculate the transformation function.

The control point density determines how much detail is included in the transformation. Few points will be enough to estimate a general pose of the structures. More points will allow fine details to be registered. However, more points also use more computational resources and time.

The λ parameter controls the degree of deformation that a transformation can achieve. An large initial value for λ will restrict the transformation to mostly affine, while an initial value for λ close to zero will allow more flexible deformations. From now on, we refer to the initial value of λ as λ .

These two parameters were tuned for the sites investigated. The distance between the transformed and the reference surfaces was used as a measure of the transformation error (see section 3.2.4 for details). The error was presented as a function of the density radius r and λ .

3.2.4. Transformation error

To assess the accuracy of the resulting transformation, we quantified the mismatch between the transformed deforming surface and its reference surface. These surfaces represent the boundary of the real structures. First, we created refined surfaces to obtain sufficient detail by using 2.5, 2.5, and 5 mm as threshold values for the head and neck, prostate and cervix cases respectively in the edge dividing procedure described in section 3.2.2. Then, the transformed deforming surface was obtained by applying the computed transformation to the refined deforming surface. Next, to quantify the mismatch between the transformed deforming surface and its reference surface, the distance between

these surfaces was measured. To calculate the distance between the surfaces, we computed the distance between each point p in the transformed refined surface to the closest triangle in the non-refined reference surface (see figure 3.4). We reported the mean distance and its standard deviation. To limit the number of values reported and to increase readability, the transformation error values were averaged over the forth-transformation and back-transformation. The consistency between the forth-transformation and back-transformation was assessed separately (see next section).

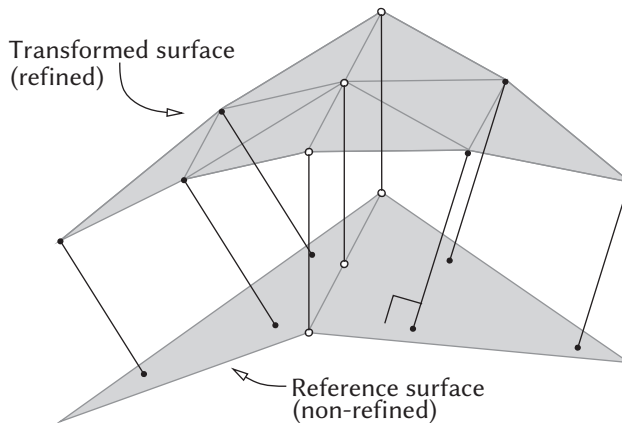


Figure 3.4: Calculating the distance between a transformed deforming surface (refined) and the reference surface (non-refined). The solid points represent projected points that fall inside the closest triangle. Notice that the projection is orthogonal to the triangle plane of the non-refined surface. The empty circles represent points that fall outside the closest triangle. For these points, the distance is defined as the shortest distance to the triangle edges.

3.2.5. Transformation consistency

There is no explicit drive in the method that makes the back-transformation (bT) to be the inverse of the forth-transformation fT , but since the input points are the same, this behavior may be expected. In practice, only the forth-transformation or the back-transformation is used in clinical applications, but to determine the consistency of the transformation we assessed the differences between the forth-transformations and back-transformations. In detail, a point p (belonging to the surface) is transformed by fT , $p' = fT(p)$. The transformed point p' is then transformed back by $bT(p') = p''$. The distance d between p and p'' for each point on the deforming and reference surface was calculated

and their mean and standard deviation are reported. Note that d also accounts for surface misalignments due to transformation inaccuracy (see section 3.2.4). When fT and bT are inverse functions of each other and the transformation error is zero, p and p'' are mapped to the same position, and d is zero. We reported the mean distance d and its standard deviation.

3.2.6. Correspondence of anatomical features

Anatomical correspondence is a prerequisite for some specific applications of non-rigid registration, such as dose accumulation and quantifying anatomical changes. The transformation error and consistency do not quantify to what extent anatomical features in the deforming CT scan are transformed to the same anatomical features in the reference CT scan. To validate anatomical correspondence, anatomical features represented as points and lines were identified for the different cases. Using the transformation found with the density radius r and λ that produced the lowest error in the parameter tuning, the residual distances between the transformed deformed anatomical features and the reference features were calculated and reported.

Anatomical features were manually or automatically identified. Figure 3.5 shows the anatomical features on the first head and neck, prostate and cervix cases. For the head and neck cases, a line was manually drawn in the middle point of the interface between the parotid gland and the mandible and styloid process. In addition, the top and bottom of the parotid and submandibular glands were automatically found by choosing the center of mass of the 5% highest and 5% lowest points. For the prostate case, the start and end points of three gold markers and the tips of the vesicles were manually identified. Each gold marker was represented as a line segment joining the start and end point. The apex was automatically identified in the same way as the bottom of the parotid and submandibular glands in the head and neck case. For the cervix cases, the midline of the uterus was automatically segmented using distance maps. The patient had four calcifications in the cervix, close to the cervix' surface. These calcifications, as well as the tip of the uterus and the top of the bladder were manually defined. The bottom of the bladder was defined in the same way as the bottom of the parotid and submandibular glands in the head and neck case. For the rectum no landmarks were defined, since no unmistakable points could be identified.

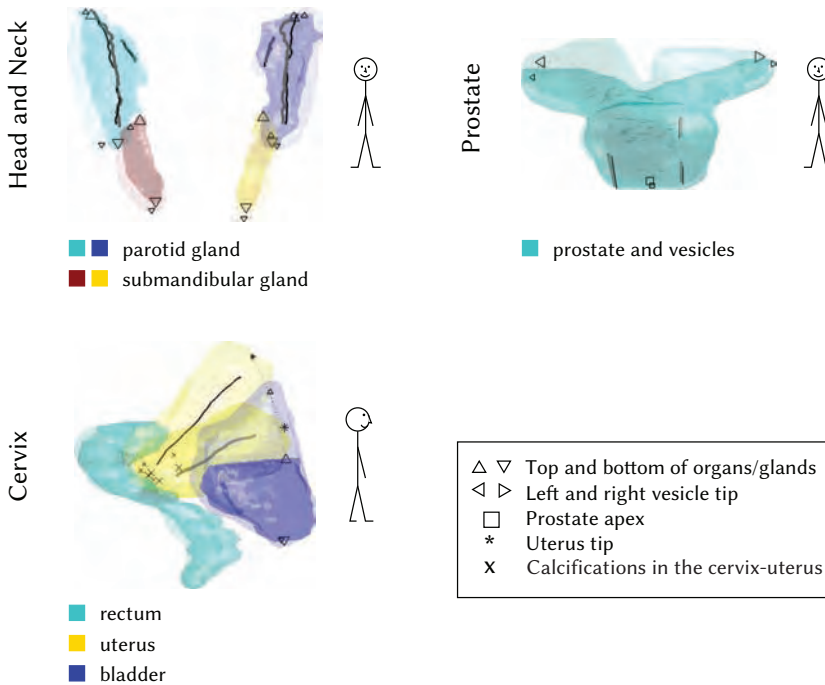


Figure 3.5: Anatomical features per site. Reference points and lines are shown in black, deforming points and lines are shown in gray. The images show the original overlap between deforming and reference sets: surfaces, lines and points. The lines represent the mandible - parotid gland and styloid process - parotid gland interfaces in the head and neck case, the gold markers in the prostate case and the uterus midline in the cervix case.

3.2.7. Inclusion of anatomical features in the registration

We performed non-rigid registrations including the anatomical features identified in the previous section. The anatomical features were used to guide the non-rigid registration locally to achieve a more coherent transformation. Each anatomical feature was included in the control point set as a different structure with a unique index. Using the transformation obtained, residual distances between the transformed deformed anatomical features and the reference features were calculated and reported. The residual distances cannot be used as an independent validation for this registration as they were part of the registration process itself. Nevertheless, we reported them since the residual distances are not necessarily zero. In a non-regularized TPS transformation the residual distances would be zero, but in the current TPS implementation the

degree of deformation of the transformation is regulated by λ . For example, a large value for λ restricts the transformation to be mostly affine and would align the structures globally. This would result in a mismatch of the anatomical features for non-rigidly deforming organs. The transformation error and the transformation consistency were reported as well for the registration including anatomical features.

3.3. Results

3.3.1. Correspondence filtering

Figure 3.6 shows the difference between the original registration (m is not filtered) and our adapted method (m is filtered). The circles show the problematic areas that were wrongly mapped using the original method, and that were correctly mapped using our adapted method. For the head and neck case, the lower area of the parotid gland was mapped to the upper area of the submandibular gland. For the cervix case, areas in the rectum were wrongly mapped to the cervix and uterus, and the upper area of the uterus was wrongly mapped to the upper area of the bladder. By filtering m during the registration, all the structures in the head and neck and cervix cases were handled correctly.

3.3.2. Parameter tuning

A total of 312 registrations, that resulted in 624 back and forth transformations, were performed for parameter tuning, and the results are presented in figure 3.7. The transformation error, defined as the mean distance between the transformed and reference surfaces, was smaller than 1 mm for all the cases. The transformation error for the head and neck and prostate cases presented a shallow minimum as a function of λ . The lowest transformation error ranged between 0.4 and 0.5 (standard deviation ranged between 0.3 and 0.4) mm for λ between 0.05 and 0.7. As expected, the transformation error reduced with decreasing density radius, producing the lowest transformation error for $r = 5$ mm. For the cervix cases, the lowest transformation error was 0.6 ± 0.5 mm (partial vs. empty) and 0.5 ± 0.4 mm (partial vs. full), for $r = 8$ mm and λ around 0.1. The density radius r and λ parameter values that were used in the rest of the analysis are shown as red squares in figure 3.7.

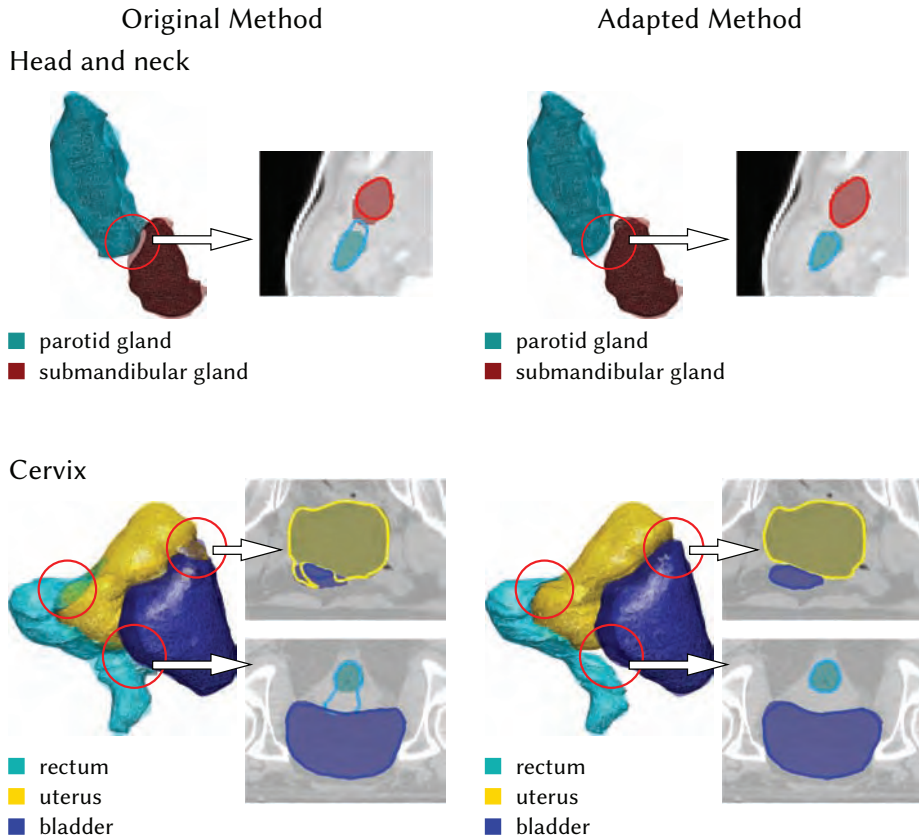


Figure 3.6: Head and neck and cervix examples showing the effect of filtering the correspondence matrix. The reference and transformed surfaces are drawn in transparent and solid color respectively. Next to the surfaces, parts of axial CT images are shown, where the reference contours are presented as shadows, and the transformed contours are presented by solid lines. The first column shows the results of the original method, which does not filter the correspondence matrix m . The circles point out the wrong mapping between different structures. The second column shows the results of our adapted method, which filters the correspondence matrix m .

3.3.3. Registration results

Figure 3.8 shows the results of the registration of the first head and neck, prostate and cervix case. The average length of the deformation vectors was 5.8 ± 2.5 mm (range 0.4 - 15.7 mm) and 2.6 ± 1.1 mm (range 0.1 - 6.6 mm) for the first and second head and neck case; 7.2 ± 4.5 mm (range 0.9 - 19.9 mm) and

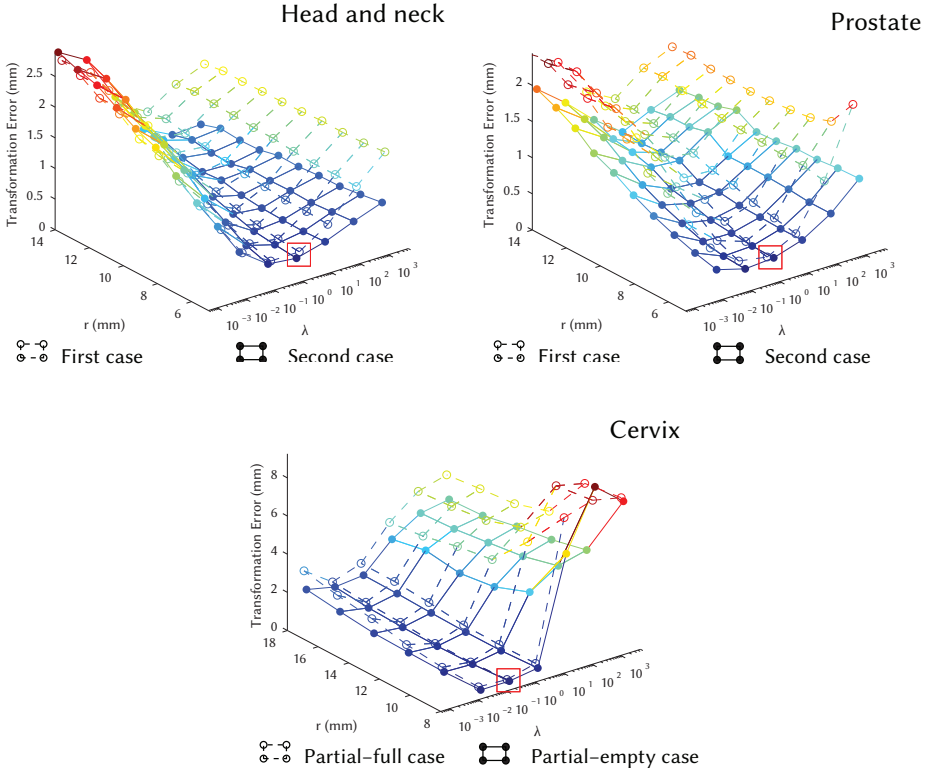


Figure 3.7: Transformation error as a function of the density radius r and λ for all cases. Each graph shows the average of the back-transformation error and forth-transformation error, which was below 1 mm. The open and solid circles show the tested parameter values and the associated transformation error. The square indicates the parameters chosen for the rest of the analysis.

8.6 ± 1.9 mm (range 4.5 - 16.9 mm) for the first and second prostate case, and 19.0 ± 11.6 mm (range 0.6 - 49.7 mm) and 14.5 ± 9.3 mm (range 0.2 - 42.3 mm) for the partial vs. empty and partial vs. full case. The total number of control points was on average 1362, 975 and 2282 for the head and neck, prostate and cervix cases, and their registration took on average 30, 17 and 116 minutes respectively.

Transformation consistency

By comparing the forth-transformation fT and back-transformation bT for the different values of density radius r and λ , we noticed that the

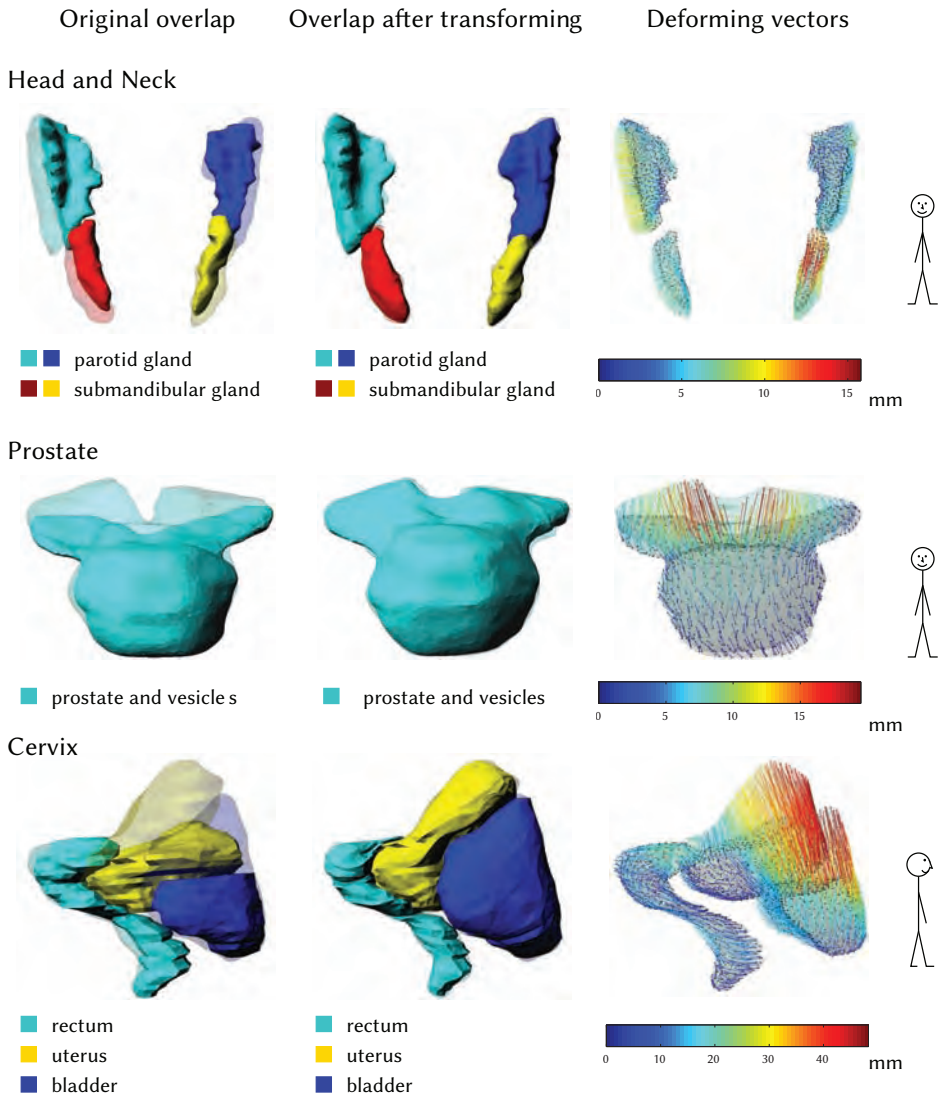


Figure 3.8: Registration results. Reference surfaces are shown in transparent colors, deforming surfaces are shown in solid colors. Note that the three cases are presented in different scales. First column shows the original overlap between deforming and reference surfaces. Second column shows the overlap between transformed deforming surface and reference surface. Third column shows the deformation vectors where, for visualization purposes, the structures were separated.

transformation consistency worsened as λ decreased. For large λ values where the transformation is mostly affine, the consistency worsened again. These transformation were unacceptable, and they showed very large the transformation errors (see cervix case on figure 3.7, large λ , small r). In general terms, the consistency was better (smaller value) for more affine transformations than for more non-rigid transformations. The consistency of the transformation generated with the density radius r and λ that produced the lowest error, was similar for the head and neck and prostate cases: 1.7 ± 1.5 mm and 1.4 ± 1.2 mm for the first and second head and neck cases and 1.6 ± 1.4 mm and 1.0 ± 0.7 mm for the first and second prostate cases respectively. The transformation consistency for the cervix cases was larger, 4.6 ± 3.5 mm and 4 ± 3.6 mm for partial-empty and partial-full cases respectively.

3.3.4. Anatomical correspondence

Tables 3.1-3.3 and figure 3.9, show the registration results for the point and lines that were identified as anatomical corresponding features. The tables list the residual distances between the transformed deformed anatomical features and the reference features for the normal registration and the complemented registration. They also list the original distance between the deforming and reference features.

The residual distances between the landmarks after registration varied for the different sites. For the first head and neck case, all the residual values were below 3 mm, except for the top point in the right submandibular (3.8 mm). The residual distances of the second head and neck case were all below 2 mm. Most residual distances for the prostate cases were below 3 mm, except for the vesicle tips (up to 3.7 mm). Notice that the gold markers in the first prostate case were already very close after the rigid bone matching (around 2 mm apart), opposite to the second case where the markers were relatively far from each other (around 6 mm). The order of magnitude of the residual errors is larger for the cervix cases. The residual errors for the partial vs. empty bladder filling case for the cervix, varied between 2.6 and 11.2 mm. The residual errors of the uterus tip and bladder top were the largest, above 10 mm. The partial vs. full bladder filling case varied between 5.0 and 11 mm. The largest error was found in one of the calcifications.

Table 3.1: Distance between anatomical lines and points for the head and neck cases. *O*: Original distances after rigid bone match. *R*: Residual distances after transformation (not including anatomical features). *R+A*: Residual distances after transformation (including anatomical features).

Anatomical features	Residual distances after transformation (mm)					
	Case 1			Case 2		
	O	R	R+A	O	R	R+A
Left Parotid						
Mandible line	2.7	1.3	0.4	0.9	1.6	0.4
Styloid process line	0.8	1.0	0.3	0.7	1.0	0.4
Top	6.1	2.7	1.6	1.7	0.7	0.4
Bottom	4.6	0.9	0.5	3.8	0.5	0.6
Right Parotid						
Mandible line	1.3	2.2	0.4	0.9	0.9	0.3
Styloid process line	0.5	1.3	0.3	0.8	1.5	0.3
Top	3.6	0.6	1.6	1.2	1.6	0.7
Bottom	8.8	1.2	1.0	1.2	1.3	0.6
Left Submandibular						
Top	10.7	2.1	1.4	1.3	0.6	0.4
Bottom	6.2	2.3	1.3	3.9	0.9	0.6
Right Submandibular						
Top	6.3	3.8	2.2	1.5	0.8	0.4
Bottom	6.1	2.6	1.0	4.3	1.7	0.8

3.3.5. Inclusion of anatomical features in the registration

As expected, all the residual distances reduced for the registrations that included the anatomical landmarks. For the first head and neck case, the residual distance was below 2 mm, except for the top point of the right submandibular gland. For the second head and neck case, the residual distance was below 1 mm. All the residual errors for the prostate cases reduced to below 1.5 mm. Most of the residual errors for the cervix cases were below 2 mm, except for the top point of the bladder in the partial vs. empty bladder filling case (2.5 mm) and one of the calcifications in the partial vs. full bladder filling case (2.8 mm).

Table 3.2: Distance between anatomical lines and points for the prostate cases. *O*: Original distances after rigid bone match. *R*: Residual distances after transformation (not including anatomical features). *R+A*: Residual distances after transformation (including anatomical features).

Anatomical features	Residual distances after transformation (mm)					
	Case 1			Case 2		
	O	R	R+A	O	R	R+A
Prostate						
Gold marker 1	2.5	2.7	0.1	6.7	1.3	0.1
Gold marker 2	1.3	1.8	0.2	6.1	3.0	0.3
Gold marker 3	1.7	1.3	0.2	6.1	1.8	0.1
Apex	1.6	1.5	0.5	6.2	1.4	0.5
Vesicles						
Left Tip	6.7	2.0	0.6	14.9	3.7	1.5
Right Tip	5.3	3.4	1.4	17.3	3.6	1.3

The transformation error was not compromised by including anatomical features in the registration. The transformation error was below 1 mm for all cases, 0.5 ± 0.4 , 0.4 ± 0.3 mm for the first and second head and neck cases, 0.4 ± 0.3 , 0.4 ± 0.3 mm for the first and second prostate cases and 0.6 ± 0.5 , 0.5 ± 0.4 mm for the cervix cases. The transformation consistency, which showed a slight improvement, was 1.4 ± 1.3 , 1.0 ± 0.8 mm for the first and second head and neck cases, 1.4 ± 1.3 , 0.9 ± 0.8 mm for the first and second prostate cases and 4.3 ± 3.0 , 3.6 ± 2.6 mm for the cervix cases.

3.4. Discussion

The described framework estimates the correspondence as part of the registration process. This is an important difference with the currently available feature-based registration methods in radiotherapy. Brock et al. [13] relied on the curvature of the structures to determine points of correspondence that were used to calculate the non-rigid registration. Schaly et al. [113] generated corresponding points and applied thin-plate splines to find the non-rigid transformation, assuming that in-plane or out of plane rotations are negligible. Kaus et al. [63] created corresponding points by adapting a generated surface

Table 3.3: Distance between anatomical lines and points for the cervix cases. *O*: Original distances after rigid bone match. *R*: Residual distances after transformation (not including anatomical features). *R+A*: Residual distances after transformation (including anatomical features). Case 1: partial-empty. Case 2: partial-full.

Anatomical features	Residual distances after transformation (mm)					
	Case 1			Case 2		
	O	R	R+A	O	R	R+A
Uterus						
Mid-line	24.3	5.7	0.5	12.0	5.0	0.4
Tip	48.8	10.1	1.9	22.1	7.6	1.5
Calcification 1	5.4	3.2	0.9	4.9	6.5	1.3
Calcification 2	8.7	4.7	0.5	4.8	8.5	1.6
Calcification 3	7.5	3.2	0.7	3.4	11.0	2.8
Calcification 4	3.6	3.2	0.9	4.1	5.0	1.2
Bladder						
Top	45.5	11.2	2.5	26.3	8.5	1.9
Bottom	2.1	2.6	0.5	3.0	5.1	1.7

from the reference organ to the deformed organ. However, all these methods rely on a correspondence that is known before the registration starts, and a fixed correspondence, if it is not rightly set, can be a source of error in the registration. The only attempt to dynamically adjust the corresponding points was made by Liang and Yan [84]. They tried to cope with the uncertainty related to the correspondence between points by iteratively changing the location of the points by minimizing a strain energy function obtained from a FEM simulation. The limitation with this last approach is that it relies on one-to-one correspondence. Our framework uses the method described by Chui et al. [25], where the correspondence is fuzzy, allowing the registration of n vs. k points, and is refined progressively during the process. Our new approach of filtering the correspondence matrix, based on structure correspondence, is essential when more than one structure is being processed simultaneously (figure 3.6).

Using the density radius r and λ that produced the lowest transformation error, the framework yielded reasonable transformations when only the surface of the structures was included in the process. Validating the method is difficult, since there is no golden standard to compare the results with. We measured the

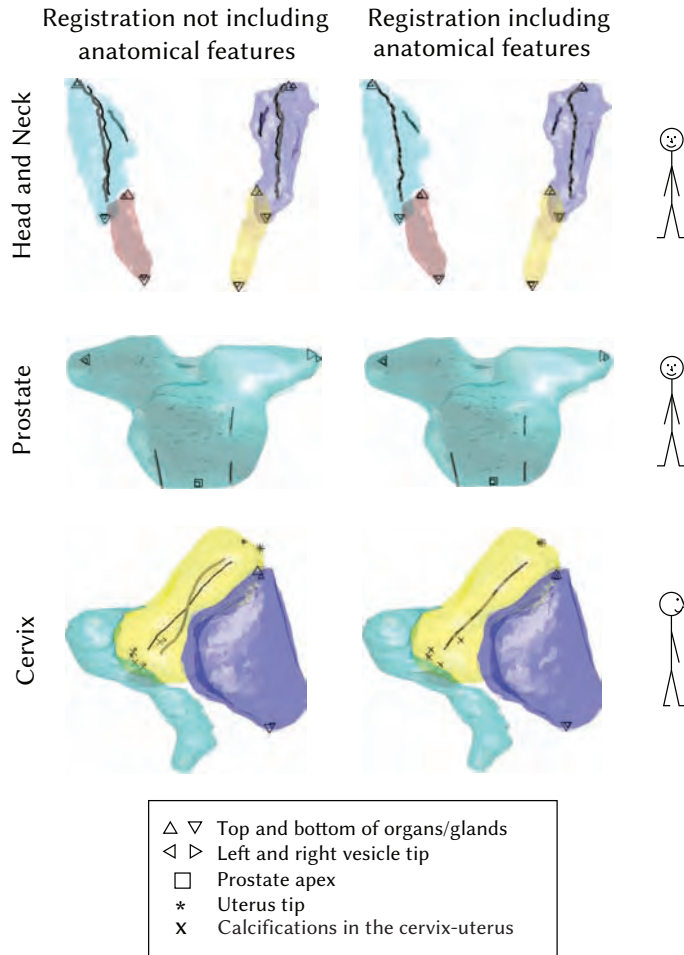


Figure 3.9: Differences between the registration including and not including anatomical features. Reference points and lines are shown in black, deforming points and lines are shown in gray. The original sets are shown in figure 3.5. The first and second columns show the overlap between the transformed deforming set and the reference sets using the transformations resulting from not including and including anatomical features respectively. The lines represent the mandible - parotid gland and styloid process - parotid gland interfaces in the first row, the gold markers in the second row and the uterus midline in the last row.

residual distances between corresponding anatomical features (tables 3.1, 3.2 and 3.3; see the 'R' columns to compare the results with other studies). Similar approaches to validate non-rigid registration methods have been used in the

past. Brock et al. [13] validated their method by tracking visible bronchial and vessel bifurcations in lung and liver, and reported an error of 1.9, 2.8 and 1.7 mm in the left-right (LR), antero-posterior (AP) and inferior-superior (IS) directions respectively. Kaus et al. [63] measured the accuracy of their approach by tracking implanted gold markers in the prostate, and reported standard deviation of the errors of 1.6, 2.3 and 2.5 mm for LR, AP and IS directions respectively. Schaly et al. [113] measured the residual distance between markers in the prostate and vesicles and reported an average registration error of 3.0 mm. Our results are comparable (average 3D error of 2.1 and 2.5 mm for the first and second prostate case, not including the anatomical features in the registration). Notice that all these methods use a fixed correspondence set beforehand.

In the current study, the non-rigid registration framework was applied to three different sites. For all the studied sites, the density radius r that yielded the lowest error was the smallest density radius tested (5, 5 and 8 mm for head and neck, prostate and cervix sites respectively). A smaller density radius, would probably further reduce the transformation error, but would lead to an unacceptably high computational time. Furthermore, the achieved accuracy of 0.6 mm is acceptable for clinical applications. At present, the transformation obtained is applied in regions close to the structures or landmarks. The use of the transformation far from the region of interest is not yet tested nor validated. To use the current method for such an application, further research is needed.

Intraobserver variation in delineations plays an important role in the accuracy of the non-rigid registration. Every mistake that is made when delineating propagates in the method, since the delineated structures are the only visible information used by the framework. Including complementary information, such as internal structures clearly visible or automatically extracted features near or around the delineated structures could minimize the effect of delineation uncertainties.

The values presented in the first column ('O') in tables 3.1, 3.2 and 3.3 serve as a reference of the initial mismatch between anatomical features. However, these values are, to a certain extent, arbitrary since they depend on the pre-registration used. In our study, the pre-registration was rigid and based on bony anatomy in the region of interest. If a different pre-registration, e.g. based on golden markers, or no pre-registration had been used, the initial mismatch values could have been completely different.

For the cervix cases, the λ parameter played an important role in finding the lowest transformation error. In order to reach a deformation with an acceptable

transformation error, the transformation has to be able to achieve a minimum flexibility to register the organs. In this study we found an appropriate λ by testing different values per case. However, this approach is for clinical applications not practical because of the large number of registrations that has to be performed. A possible alternative is to estimate λ based on the amount of overlapping between the input structures, with tools such as the Jaccard index or the dice coefficient, but further experimentation and research is needed. A practical approach is to use a constant λ value per site. Previous studies [132, 129] have used such an approach. Care has to be taken if the inter-patient variability in shape and deformation is large, as the use of an inappropriate λ value could render unacceptable results.

Including complementary a-priori information in the process did not require any modification in the existing framework and resulted in a more anatomically coherent transformation. When the anatomical landmarks were included, the residual distances reduced on average to less than 1 mm for the head and neck and prostate cases and 1.6 mm for the cervix cases. The largest residual distances for the cervix cases were found for the calcifications, which were close to the surface. Notice that due to the proximity, the surface points compete in the registration with each calcification point. Consequently, the influence of a single anatomical point within close proximity to the surface is not enough to reduce the residual distances to the submillimeter range.

The registration including anatomical features was not independently validated. Error measures such as the transformation error and transformation consistency were calculated, and their values hardly changed. In order to independently validate this registration, additional landmarks should be identified. However, these extra landmarks could not be identified in the CT scans. To obtain additional independent landmarks other imaging modalities could be applied, e.g. MR imaging. Many of the anatomical landmarks were manually identified, such as the tip of the uterus. The identification of these anatomical landmarks depends on the observer's interpretation and on image quality. The uncertainty in the location of the landmarks is a possible source of error.

In this study we included anatomical landmarks in the form of points and lines. Points were used to represent locations for which correspondence was clear, such as the vesicle tips in the prostate cases. Lines were used to indicate the interface between bony anatomy and glands for the head and neck cases, the midline of the cervix-uterus in the cervix cases and the gold markers in the prostate cases. Lines can also be used to represent veins, arteries, foldings,

air conducts, etc. Also open or partial surfaces representing structures that are not completely included in the region of interest, such as skin, bony anatomy, etc, can be included in the process by sampling their area with points, by using the procedure illustrated in figure 3.2. Each of these points, lines or open surfaces is considered a different organ when filtering the correspondence matrix, therefore the points that make up a line or open surface do not require one-to-one correspondence. Moreover, there is no restriction on whether the points, lines or open surfaces are on the surface, inside or outside of the structures. In this study we identified anatomical landmarks on CT scans. However, the advantages of this method can be exploited even more when images with better soft tissue contrast, such as MRI scans, are used to identify the anatomical landmarks.

The framework in its current state has a limited use for online corrections, since the computational times are large (17 minutes for around 900 points, prostate cases). However, there is room to optimize the code. On the other hand, the number of points plays a very important role in the computational time. Literature has shown that thin plate spline works best when homogeneously spread data is used [145]. In the current study a semi-homogeneously spread set of points was generated on the surface. In this way, all parts of the surfaces are equally represented for the non-rigid registration. Nevertheless, adaptive point generation [69, 62], where critical areas that need more detail get denser point clouds than areas that are less critical for the registration, may yield good results in the registration and may also reduce the computational time when less points are needed.

3.5. Conclusion

The results demonstrate that our non-rigid registration framework is an effective method to simultaneously register anatomical changes of multiple organs with very different magnitudes and complexity. Moreover, a global transformation, which is locally more anatomically coherent is produced when anatomical features are added to the registration. The inclusion of additional features is fully supported by our novel flexible framework.



Chapter 4

A symmetric non-rigid registration method to handle large organ deformations in cervical cancer patients

Luiza Bondar, Mischa S. Hoogeman, Eliana M. Vásquez Osorio, and Ben J. M. Heijmen

Published in
Medical Physics
Vol 37, No. 7, pp. 3760 - 3773, 2010

Abstract

Purpose: Modern radiotherapy requires assessment of patient anatomical changes. By using unidirectional registration methods, the quantified anatomical changes are asymmetric, i.e., depend on the direction of the registration. Moreover, the registration is challenged by the large and complex organ deformations that can occur in, e.g., cervical cancer patients. The aim of this work was to develop, test, and validate a symmetric feature-based nonrigid registration method that can handle organs with large-scale deformations.

Methods and Materials: A symmetric version of the unidirectional thin plate spline robust point matching (TPS-RPM) algorithm was developed, implemented, tested, and validated. Tests were performed by using the delineated cervix and uterus and bladder in CT scans of five cervical cancer patients. For each patient, five CT scans with a large variability in organ shape, volume, and deformations were acquired. Both the symmetric and the unidirectional algorithm were employed to calculate the registration geometric accuracy (surface distance and surface coverage errors), the inverse consistency, the residual distances after transforming anatomical landmarks, and the registration time. Additionally, to facilitate the further use of our symmetric method, a large set of input parameters was tested.

Results: The developed symmetric algorithm handled successfully the registration of bladders with extreme volume change for which TPS-RPM failed. Compared to the unidirectional algorithm the symmetric algorithm improved, for the registration of organs with large volume change, the inverse consistency by 78% and the surface coverage by 46%. Similarly, for organs with small volume change, the symmetric algorithm improved the inverse consistency by 69% and the surface coverage by 13%. The method allowed for anatomically coherent registration in only 35 s for cervix-uterus and 151 s for bladder, while keeping the inverse consistency errors around 1 mm and the surface matching errors below 1 mm. Compared to rigid alignment the symmetric method reduced the residual distances between anatomical landmarks from a range of $5.8 \pm 2 - 70.1 \pm 20.1$ mm to a range of $1.9 \pm 0.2 - 8.5 \pm 5.2$ mm.

Conclusions: The developed symmetric method could be employed to perform fast, accurate, consistent, and anatomically coherent registration of organs with large and complex deformations. Therefore, the method is a useful tool that could support further developments in high precision image guided radiotherapy.

4.1. Introduction

Imaging is an integrated part of patient management in modern radiotherapy [35, 67, 116, 130]. Image registration is routinely used to find the spatial correspondence (mapping) between two image datasets acquired at different moments in time [67, 116, 90, 28]. Proper registration techniques can improve patient setup, the estimation of the actual dose delivered, and the assessment of anatomical changes needed in adaptive radiotherapy [67, 116]. For many situations, a “gold standard” correspondence between two images cannot be known [90, 28]. Instead, several tests are used to validate the registration results such as by assessing the residual error between corresponding anatomical features (e.g., markers and vessel bifurcations, [116]), the contour matching of segmented structures, and the inverse consistency of the registration [28, 20]. The advantage of inverse consistent registration is that the observed change, e.g., organ motion, is independent of the order in which the images are registered [20, 60, 142]. Compared to unidirectional methods, inverse consistent or symmetric registration algorithms lead to more coherent and biologically meaningful results, better correspondence between medical images [20, 60, 142], smoother displacement fields [148] and consistent deformation vectors [142]. For image guided and adaptive radiotherapy, consistent registration supports mapping in both directions, which allows for coherent dose accumulation [142].

Online image guidance, fast image registration, and assessment of organ change are required to improve the radiotherapy treatment for cervical cancer patients [65, 66]. However, registration of images in the pelvic region is a challenging task due to the extreme organ displacements and the large differences in bladder and rectum filling [141, 42, 140]. There are several methods that can handle the large deformations in the pelvic area [141, 42, 140, 85, 21]. Symmetric image registration methods were used to register intensity-manipulated images of prostate patients [42], but their extension to images of cervical cancer patients is limited by the complexity and the large magnitude of uterus motion.

The aim of our work was to develop a fast and consistent registration method that would allow for the evaluation of the anatomical changes experienced by the internal organs in cervical cancer patients. Similar to other registration methods that can handle large deformations [141, 42, 140, 85, 21, 13, 133], our method employs features delineated from images. Our method is an improvement of the unidirectional thin plate spline robust point matching (TPS-RPM) feature-based registration algorithm [133, 25]. TPS-RPM is an attractive

method that evaluates simultaneously a unidirectional correspondence between automatically placed markers on the surfaces of organs and a unidirectional transformation that maps one organ into the other. Moreover, TPS-RPM can handle multiple structures and allows for the inclusion of additional anatomical features to guide the registration [133]. However, the unidirectional TPS-RPM suffers from poor inverse consistency for cervical cancer patients and is computationally demanding [133]. In addition, the unidirectional TPS-RPM fails to map bladders with extreme bladder volume change.

Our improved method aims to reduce the inverse consistency error (ICE) and to allow for an accurate mapping of organs that exhibit large-scale deformations at low computational costs. We demonstrate the performance of the new registration method over the unidirectional TPS-RPM algorithm by using the CT scans of five cervical cancer patients that presented large intra- and interpatient variability in organ shape, volume, and deformation. Additionally, to facilitate the further use of our method, we provide recommendations for an optimal choice of input parameters based on extensive parameter testing and validation. The patient data used in this study and the novel registration method are described in section 4.2 of this paper. The improvements in inverse consistency, accuracy, and robustness and the recommendations on the choice of input parameters are presented in section 4.3. Finally, the most important features of our method and the results are discussed in section 4.4 before we draw our conclusions in section 4.5.

4.2. Materials and methods

4.2.1. Patient data

A total of 25 CT scans of five cervical cancer patients was employed. Each patient underwent a planning CT scan with a large full bladder. To allow for a better delineation of the planning CT scan, the patients received intravenous (IV) contrast before scanning. Additionally, four subsequent variable bladder filling CT scans were acquired during 1 h after the patient emptied her bladder and drank 300 ml of water. These repeat CT scans were acquired with the purpose of visualizing the natural filling of the bladder from empty to full. To ease the tumor localization, patients had three to four fiducial markers implanted in the fornices of the vagina. The bladder and the cervix-uterus structure (uterus, cervix, and the superior part of the vagina) were manually contoured on the axial slices of the 25 CT scans. The most caudal contour of the cervix-uterus was delineated in the slice below the most caudal fiducial. The

structures were contoured by a radiation technologist, reviewed by a radiation oncologist, and inspected in 3D to further minimize delineation errors. For convenience, the deformations of an organ were registered and analyzed in the frame of reference of the planning CT. Therefore, for each patient the four repeat scans were rigidly bone-matched with the planning CT scan by using the pelvis bony anatomy.

4.2.2. Surface rendering and smoothing

From each delineated structure, a three dimensional (3D) triangulated surface was generated. The 3D surfaces were faceted and presented sharp edges due to the interslice distance and the approximation of contours with polygonal lines. To minimize delineation artifacts and to improve the anatomic representation of the organs, a Taubin filter [121, 122] was used to smooth all 3D surfaces. Unlike Gaussian or Laplacian smoothing, Taubin filtering produces little or no volume shrinkage [121]. Moreover, this filtering process can be constrained such that the resulting surfaces are smoothed along boundary curves but not across these curves [122]. Thus, tubular organs like rectum or blood vessels can be smoothed with minimum volume change and without unnecessary shrinkage of the end contours. Here, global smoothing was used for the bladder structures and constrained smoothing was used for the cervix-uterus to prevent smoothing across the most caudal axial contour. The smoothing error was quantified in terms of the percentage of the volume difference between the smoothed surface and the original surface from the volume of the original surface. Additionally, the mean distance between the points on the smoothed surface and the original surface was evaluated. The mean distance between points and surface was determined by using the method developed by Vásquez Osorio et al. [133, 132]. For the cervix-uterus case, the contour preserving error, i.e. mean distance between the points on the constrained contour on the smoothed and the same contour on the original surface, was also computed. The filtering method gives good results when the triangulation has faces of roughly uniform size. Therefore, a mesh refinement algorithm was applied before smoothing to assure that the lengths of the triangle edges were smaller than a given threshold [133].

4.2.3. Point generation

Here, point-based registration was guided by sets of control points (landmarks) distributed on the surfaces of two organs. Unlike other point-based

methods, the TPS-RPM method does not require a-priori knowledge on landmark correspondence. Instead, the correspondence between control points is part of the solution of the registration process. Sets of homogeneously distributed points were generated on the smoothed surfaces to limit correspondence errors caused by irregular point distributions. The points were distributed by following an improvement of the methodology developed by Vásquez Osorio et al. [133]. In reference [133], the vertices were grouped in spheres of a certain radius and replaced by the centroid of the grouped vertices. The centroids, however, did not necessarily lie on the surface. The improved method selects from the grouped vertices the vertex that is closest to the centroid of the group. This vertex, which is by definition on the surface, is added to the control point set. Finally, by varying the sphere's radius, control point sets with different mean densities ρ can be generated on the surface of the organs. Here, the point set density is given by the inverse of the average of the minimum distance between an individual point and the remaining points in the cloud. Thus, for a given surface the number of control points increases with the increase in ρ .

4.2.4. Theoretical background

TPS-RPM is a unidirectional method that iteratively searches for a correspondence and for a forward transformation FT between the control points on the surface of the source organ and the control points on the surface of the target organ [25]. In the following, we will denote the control points on the surface of the source with X and the control points on the surface of the target with Y . The point sets X and Y have n_x points $\{x_i, i = 1, \dots, n_x\}$ and n_y points $\{y_i, i = 1, \dots, n_y\}$, respectively. The number of points n_x and n_y and the point set densities of the sets X and Y can be different. The correspondence between the points in X and Y is expressed in terms of a correspondence matrix $FM := \{m_{i,j}, i = 1, \dots, n_x + 1, j = 1, \dots, n_y + 1\}$ with positive entries, and which each first n_x rows and first n_y columns sum up to 1. For $1 \leq i \leq n_x$ and $1 \leq j \leq n_y$, the value of $m_{i,j}$ represents the strength of the correspondence between points x_i and y_j . The method allows for partial matches between the control points, i.e., a point in one organ can correspond to more points on the other organ. Values of the correspondence matrix close to 1 indicate strong correspondences, whereas weak correspondences are denoted by values close to 0. This method also allows for the possibility to treat points as outliers, i.e., points in a set that do not correspond to any point in the other set. The degree of acceptance of the points in X and Y as outliers is indicated by the values

of $m_{i,j}$ in the extra n_{x+1} th row and extra n_{y+1} th column, respectively. The solution of the registration problem, i.e., the correspondence matrix and the transformation FT , is the minimum of the following objective function:

$$E(FM, FT) = \sum_{i=1}^{n_x} \|q_i - FT(x_i)\|^2 + \lambda T \|L(FT)\|^2, \quad (4.1)$$

where $q_i = \sum_{j=1}^{n_y} m_{i,j} y_j$ is a virtual corresponding point for x_i . The transformation FT from X to Y is found based on thin plate spline interpolation, which requires setting L in eq. 4.1 to the “bending energy” operator [10]. In order to obtain more stable results, a smoothing parameter λ is introduced [136]. The parameter λ controls the assumed initial rigidity of a transformation. Large values correspond to affine transformations, whereas small values correspond to elastic registrations. The outlier sets in X and Y are modeled as clusters with a large variance T^0 . Algorithm 2 was proposed by Chui and Rangarajan [25] to solve the minimization problem 4.1.

The algorithm is an iterative annealing process that controls the updates of the correspondence and the transformation. The annealing process gradually reduces a temperature parameter T from a large initial temperature T^0 to a final temperature T_{final} by a fixed annealing rate $T_{k+1} = T_k \times r_a$, where $0 < r < 1$ is the annealing rate and k is the iteration number. The temperature controls the level of fuzziness of the correspondence between the two point sets. Thus, T_{final} controls the level of fuzziness of the final correspondence matrix determined by the registration process. A low T_{final} allows for a final correspondence between the control points closer to the one-to-one limit, whereas a higher T_{final} allows for partial matches. The elasticity parameter λ is also decreased by the annealing rate from a large value corresponding to a global rigid match λ^0 to a small value that allows for fine nonrigid tuning. The maximum number of internal iterations I^0 is a stopping criterion that influences the computation time and controls the level of accuracy of the correspondence matrix and of the transformation achieved at each intermediate value of the decreasing temperature [44]. The total calculation time increases linearly with the increase in I^0 . The stopping criterion based on reaching a maximum number of iterations is a convenient replacement of a convergence check for the parameters of the transformation. In practice, this is more efficient because it is not necessary to have achieved a strict convergence of the transformation function and correspondence matrix at each iteration level [25, 44].

To additionally calculate the backward transformation (BT), the registration process needs to be repeated by exchanging the roles of the control points

Algorithm 2 TPS-RPM

Initialization

 $FT \leftarrow$ identity transformation $T \leftarrow T^0$ $m_{i,j} \leftarrow \frac{1}{T^0}$ $\lambda \leftarrow \lambda^0$

Iterations

while $T > T_{\text{final}}$ **do** **for** $I \leftarrow 1$ to I^0 **do** Update the correspondence matrix FM **for** $i \leftarrow 1$ to $n_x + 1$ and $j \leftarrow 1$ to $n_y + 1$ **do** **if** i is $n_x + 1$ or j is $n_y + 1$ **then** $T_{i,j} = T^0$ **else** $T_{i,j} = T$ **end if** $m_{i,j} = \frac{1}{T_{i,j}} e^{-\frac{\|y_j - FT(x_i)\|^2}{2T_{i,j}}}$ **end for** normalize first $n_x + 1$ rows and $n_y + 1$ columns to sum up to 1 Update the transformation FT **for** $i \leftarrow 1$ to n_x **do** $q_i \leftarrow \sum_{j=1}^{n_y} m_{i,j} y_j$ **end for** $FT \leftarrow$ thin plate spline that maps x_i to q_i using λ **end for** $T \leftarrow T \times r_a$ $\lambda \leftarrow \lambda \times r_a$ **end while**

X and Y . This results in a backward transformation BT and in a backward correspondence matrix (BM). The correspondence of the control points given by the matrix BM is different from the correspondence stored in the matrix FM calculated by the forward registration process. BT is not the inverse of FT , which means that an anatomical change measured by FT is different from the one measured by BT .

4.2.5. The symmetric TPS-RPM algorithm

To improve the consistency of the algorithm, we propose to estimate the point correspondence of the forward and backward registration based on only one correspondence matrix M instead on two different matrices (BM and FM). In addition, we impose a symmetry constraint by evaluating the correspondence matrix M based on both the forward and the backward transformations. The idea is similar to a suggestion made by Chui [23]. In the new symmetric algorithm, the correspondence matrix is given by

$$m_{i,j} = \frac{1}{T_{i,j}} e^{-\frac{\|y_j - FT(x_i)\|^2 + \|x_i - BT(y_j)\|^2}{4T_{i,j}}}, \quad (4.2)$$

for $1 \leq i \leq n_x + 1$ and $1 \leq j \leq n_y + 1$,

where $T_{i,j}$ is T^0 for the additional $n_x + 1$ row and $n_y + 1$ column for outliers and T for all point pairs x_i and y_j , as described in algorithm 2. Large values pointing at a strong correspondence are assigned to $m_{i,j}$ when both the distance between a transformed point $FT(x_i)$ and a point y_j on the deforming surface and the distance between the transformed point $BT(y_j)$ and the point on the target surface x_i are small. Likewise, small values are assigned to $m_{i,j}$ when both distances are large resulting in a weak correspondence. Therefore, rather than calculating a unidirectional correspondence, in the new symmetric algorithm the correspondence between X and Y is determined by the contribution of both the distance between the points in Y and the transformed points X and the distance between the points in X and the backtransformed points Y . The solution of the registration problem can be expressed as the minimum of the following objective function:

$$E(M, FT, BT) = \sum_{i=1}^{n_x} \|q_i - FT(x_i)\|^2 + \lambda T \|L(FT)\|^2 + \sum_{j=1}^{n_y} \|p_j - BT(y_j)\|^2 + \lambda T \|L(BT)\|^2, \quad (4.3)$$

where q_i is the virtual corresponding point for x_i and $p_j = \sum_{i=1}^{n_x} m_{i,j} x_i$ is the virtual corresponding point for y_j . We propose the symmetric TPS-RPM (S-TPS-RPM) algorithm 3, to find the solution of the minimization problem 4.3.

In the symmetric formulation, the forward and the backward transformations and the correspondence matrix M are simultaneously optimized by the iterative process. Note that the symmetric algorithm evaluates and stores only one correspondence matrix, whereas the unidirectional TPS-RPM method requires the calculation and the storage of two correspondence matrices (BM and FM) to determine the forward and the backward transformations. Moreover, unlike other inverse consistent methods [20], the above symmetric algorithm does not additionally compute the inverses of the forward and the backward transformations.

4.2.6. Parameter tuning

The final choice of registration parameters should be a trade-off between accuracy, anatomical coherence, inverse consistency, and registration time. Therefore, the following parameters were tested, the density ρ , the elasticity parameter λ , and the maximum number of internal iterations I^0 .

Parameter tuning: ρ

The density ρ determines the number of the control points and therefore influences the accuracy of the registration. Both the computation time and the accuracy increase with the increase in density. To tune the ρ parameter, surface point sets with mean point densities ρ of 1/4, 1/6, 1/8, and 1/10 were generated for each organ. By default, the density ρ was equal for the source and target surface, resulting, for the case of organs with small volume change, in a more or less equal number of control points on the surface of the source and target organs. For example, for the cervix-uterus cases, the average ratio between the number of points on the source organ and the number of points on the target organ was 0.98 ± 0.05 . However, for the case of a large volume

Algorithm 3 S-TPS-RPM

Initialization

$FT \leftarrow$ identity transformation

$BT \leftarrow$ identity transformation

$T \leftarrow T^0$

$m_{i,j} \leftarrow \frac{1}{T^0}$

$\lambda \leftarrow \lambda^0$

Iterations

while $T > T_{\text{final}}$ **do**

for $I \leftarrow 1$ to I^0 **do**

 Update the correspondence matrix M , using equation 4.2

 Normalize first $n_x + 1$ rows and $n_y + 1$ columns to sum up to 1

 Update the transformation FT

for $i \leftarrow 1$ to n_x **do**

$q_i \leftarrow \sum_{j=1}^{n_y} m_{i,j} y_j$

end for

$FT \leftarrow$ thin plate spline that maps x_i to q_i using λ

 Update the transformation BT

for $j \leftarrow 1$ to n_y **do**

$p_j \leftarrow \sum_{i=1}^{n_x} m_{i,j} x_i$

end for

$BT \leftarrow$ thin plate spline that maps p_j to y_j using λ

end for

$T \leftarrow T \times r_a$

$\lambda \leftarrow \lambda \times r_a$

end while

change, the number of control points for the source and target surface would be considerably different. For example, the ratio between the number of control points that was obtained using an equal ρ ranged from 2.4 to 5.3 for bladders with a large volume change. In order to investigate the relation between the number of point ratio and the quality of registration, additional sets of control points with mean point densities of 1/2, 1/3, 1/4, and 1/5 were generated on the surfaces of small volume bladders. The range of point ratio was thus reduced from 2.4 - 5.3 to 1 - 2.2.

Parameter tuning: λ

The initial temperature T^0 is set to the length of the diagonal of the smallest box encompassing the source and the target surfaces [133, 25]. The initial temperature is iteratively decreased to a final temperature by an annealing rate of $r_a = 0.93$ [133, 25]. The final temperature T_{final} is set to the average value of the mean densities of the control points on deforming and on target surfaces. Here, the elasticity parameter λ is set to a ratio c/T^0 , where c is a constant. This allows us to compare registration results obtained when registering organs with different degrees of deformation and to determine the suitable value for λ in terms of a simple recipe based on the initial temperature. The parameter $c = \lambda T^0$ takes nine values in the interval $[10^{-4}, 10^{+4}]$.

Parameter tuning: I^0

Previous tests on brain mapping suggest that maximum five internal iterations I^0 are sufficient to generate accurate registration results [25]. To investigate the influence of the maximum number of iterations on the registration results, here the number of internal iterations I^0 varies between 1 and 5.

Overview of performed registrations tests

For each patient, the planning organ (cervix-uterus or bladder) is registered (forth and back) by using the S-TPSRPM method with each of the four corresponding organs delineated in the repeat CT scans. Equal point densities were used for the target and source surface. By varying the parameters described above, a total number of 7200 registration pairs was generated (for both organs). For six cases of bladder registration with large volume change, an additional set of 1080 registration tests was performed by distributing on the

surface of the small bladder control points with a point density twice as large as the point density on the planning bladder.

To compare S-TPS-RPM to the original unidirectional method (TPS-RPM), unidirectional registrations were performed as well. The unidirectional registrations were performed on a subset of the data, i.e., for each patient registering the data in the planning CT scan to the data of the first repeat CT scan (large organ deformations) and to the data of the last repeat CT scan (small organ deformations). The registrations were performed for the same range of parameters as for the S-TPS-RPM method. The control point density for the target and source surface was kept equal. Thus, a number of 1080 pairs (forth and back) of unidirectional transformations were generated. The two methods were compared in terms of geometric and anatomical accuracy, inverse consistency, and registration time. The accuracy and inverse consistency metrics and the residual distance used to quantify the anatomical accuracy are defined in Sec. II G. For each error metric and for all registration tests (performed on the subset of data), the difference between the error measured by the unidirectional method and the corresponding error measured by the symmetric method was calculated. Then the percentage of the error difference from the error by the unidirectional method was determined and the average of the percentage was reported. The registration time of the symmetric method was compared to the registration time of the unidirectional method for computing both the forward and the backward transformations. Additionally, the registration time of the symmetric method (both directions) was compared to the registration time of the unidirectional method in only one direction (average over the time to compute the forward transformation and the time to compute the backward transformation). The registration tests were performed on an Intel[®] Core[™] dual core processor (2.4 GHz).

4.2.7. Validation

Geometric accuracy and inverse consistency

Geometric accuracy measures the degree of surface matching achieved by a registration test. Two metrics were used here to quantify the geometric accuracy of a transformation, the surface distance error (SDE) and the surface coverage error (SCE) (see figure 4.1). SDE is given by the mean distance between the transformed points and the target surface [133]. A small SDE is a necessary but not a sufficient condition for high accuracy surface matching (see figure 4.1(b)). For example, the SDE of an inaccurate transformation that maps all

points of the source surface onto one point of the target surface is equal to zero. Thus, a small SDE indicates that the transformed points are on the target surface but does not measure how well is the target surface covered by the transformed points.

The surface coverage is measured here by SCE, which is the standard deviation of the minimum distances between the vertices of the target surface and the transformed points of the source surface. Large values of SCE indicate that there are regions of the target surface that are not well covered by the transformed points (see figure 4.1(b)). Thus, high geometric accuracy is indicated by small SDE and SCE values (see figure 4.1(c)). By measuring both SDE and SCE, the reconstruction of a triangulated mesh from the transformed points is conveniently avoided. The registration's ICE is the deviation of the forward transformation from the inverse of the backward transformation averaged with the deviation of the backward transformation from the inverse of the forward transformation. The deviation of the forward transformation from the inverse of the backward transformation is the mean of the distances between the points on the source surface and the points resulting from backtransforming the forward transformed source points [132]. The deviation of the backward transformation from the inverse of the forward transformation is calculated in a similar way. To measure SDE, SCE, and ICE with sufficient detail and to avoid the evaluation of the registration results on the control points used for the registration process, the smoothed surfaces (with an average vertex distance of 2.5 ± 0.1 mm) were refined to surfaces with an average vertex distance of 2 ± 0.3 mm.

Anatomical validation

High geometric accuracy is required to achieve good surface mapping, but small SDE, SCE, and ICE values do not necessarily guarantee the anatomical validity of the registration results. In the absence of the true anatomical gold standard mapping between the organs, the following anatomical structures were used for the anatomical validation: The midline, the uterus tops, and the fiducial markers of the cervixuterus and the top of the bladder. The midline is the centerline of the 3D skeletons generated by using a parameter-controlled volume-thinning algorithm [40]. The top of the uterus was manually identified. For the bladder case, the sets of the 1% most cranial points were acceptable anatomical landmarks. The registration's accuracy in mapping an anatomical landmark is given by the residual distance between the transformed landmark and the corresponding landmark on the target surface. For each marker and

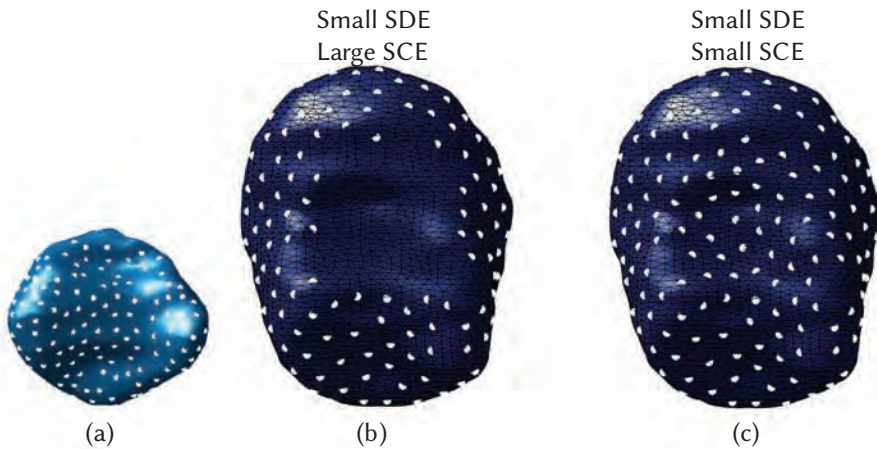


Figure 4.1: Schematic illustration of SDE and SCE. (a) Points (white circles) on a source surface. (b) A transformation maps the points of the source surface onto the target surface such that the distance between the transformed points (white circles) and the target surface is zero, i.e., $SDE=0$. However, a large part of the target surface remains uncovered by the transformed source points, $SCE=4.5$ mm. (c) A transformation maps the vertices of the source surface such that the target surface is better covered, $SCE=1.2$ mm.

each method, we calculated the difference between the residual distance after the rigid alignment and the residual distance after the nonrigid match. Then the percentage of the error difference from the residual distance after the nonrigid match was determined and the average of the percentage was reported.

4.3. Results

4.3.1. Patient data

The cervix-uteri and the bladders delineated in the acquired CT scans showed large interscan and interpatient variability in the extent of motion. The interpatient range of the cervix-uteri volumes was 108–241 cc. There was hardly any interscan cervix-uterus volume change (the range of the relative standard deviation of the cervix-uteri volumes was 3%– 8%). The bladder showed intended large variations in volume, the ratio between the volume of the planning bladder and the volume of the bladder in the repeat CT scans ranged from 0.9 to 11. For six cases, the volume ratio was larger than 3. The range of the bladder volumes was 57–730 ml. With respect to the planning CT, the organs in the first repeat CT scan showed extreme deformations, whereas

the organs in the last CT scan presented relatively small changes. Figure 4.2 depicts the bone-matched variable bladder filling CT scans for a patient that experienced an extreme bladder volume change.

4.3.2. Surface smoothing

By applying the Taubin filter, smoothed surfaces were obtained with an average volume increase with respect to the nonsmoothed surface of 0.8% for cervix-uterus and 1% for bladder. The average mean distance between the points on the smoothed surfaces and the original surfaces was 0.3 ± 0.2 mm (1 SD) for both cases. The average contour preserving error for the most caudal contour was 0.8 ± 0.4 mm (1 SD) for the cervix-uterus case.

4.3.3. Symmetric TPS-RPM vs unidirectional TPS-RPM

Figure 4.3 illustrates the main feature of the new symmetric method compared to the original unidirectional algorithm. The figure shows a clear reduction in the inverse consistency error for both a registration for organs with a large volume change (bladder) and a registration for organs with a small change in volume (cervix-uterus). The performance of both algorithms was influenced by the magnitude of the volume change of the organ. Therefore, the results for the registration of organs with large volume change (six cases for which the ratio of the volume of the large planning bladder and the smaller bladder was larger than 3) and the results for the registration of organs with small volume change (all remaining cases) are presented in separate sections. The registration of organs with small volume change represented 85% of all organ cases.

Registration of organs with small volume change

For the case of registration of organs with small volume change, the forward and the backward transformations had similar SCE and SDE values. This behavior was observed for both the unidirectional TPS-RPM and the symmetric TPS-RPM method. Therefore, in this section, the surface distance errors and the surface coverage errors denote the averages measured for the forward and the backward transformations.

Opposite to the results obtained with the unidirectional algorithm, the symmetric transformations proved robust with respect to the change in the number of internal iterations. By using the symmetric method, the increase in the number of internal iterations either improved or had hardly any effect

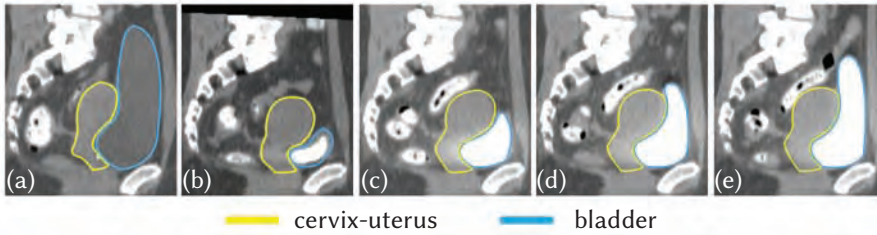


Figure 4.2: Delineated variable bladder filling CT scans for a cervical cancer patient (sagittal view). The delineated structures are cervix-uterus and bladder. a) Planning CT scan with a full bladder, b) empty bladder, and c-e) repeat CT scans demonstrating the natural filling of the bladder. The bladder in b-e) has a higher intensity than the planning bladder a) due to the washout of the IV contrast.

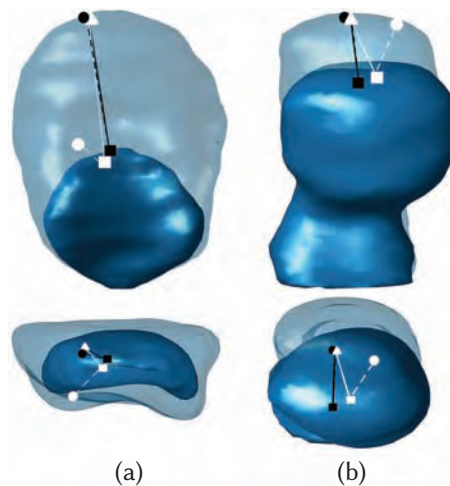


Figure 4.3: Symmetric TPS-RPM vs unidirectional TPS-RPM for a) bladder and b) cervix-uterus. First row: Coronal view, second row: Axial view. For each case, the white triangle lying on the source surface (transparent) is mapped by the unidirectional FT (white line) into the white square on the target surface (solid). The unidirectional BT (white dashed line) maps the white square into the white circle lying on the source surface. Note the large distance between the white triangle and the white circle (75 mm for bladder and 15.5 mm for cervix, depicted distances and organs are not to scale). The symmetric FT (black line) maps the white triangle into the black square and the symmetric BT (black dashed line) maps the black square into the black circle. Note that the distance between the white star and the black circle is very small (3 mm for bladder and 0.3 for cervix, depicted distances and organs are not to scale).

on the surface distance, surface coverage, and inverse consistency errors. Moreover, the influence of the number of internal iterations on the measured errors was limited only to the case of very flexible transformation ($\lambda T^0 \leq 0.1$) and had hardly any impact on the quality of the registration for the remaining range of the elasticity parameter values. The results produced by the unidirectional algorithm displayed lack of robustness with respect to the increase in the number of internal iterations. For example, the increase in the number of internal iterations resulted in an increase in the inverse consistency error. The same divergent behavior was exhibited by the unidirectional surface distance error (for the case of flexible registrations, $\lambda T^0 \leq 1$).

Figure 4.4 depicts the behavior of the inverse consistency error (figure 4.4(a)) and of the surface coverage error (figure 4.4(b)) with respect to the change in elasticity parameter and in density for unidirectional TPS-RPM and S-TPS-RPM. The ICE decreased from a range of 3-7 mm for unidirectional TPS-RPM to a range of 0.5-2 mm for S-TPS-RPM. For both methods, the SCE and SDE decreased with the increase in λT^0 on the interval of flexible and moderate elastic transformations ($10^{-4} \leq \lambda T^0 \leq 10$). On this interval, the range of SCE and SDE decreased from 0.5-1.1 and 0.2-1 mm for the unidirectional TPS-RPM to 0.5-0.8 and 0.2-0.7 mm for the S-TPS-RPM, respectively. For both methods, for the remaining range of λT^0 values ($100 \leq \lambda T^0 \leq 10^4$), the SDE and SCE increased with the increase in λT^0 , i.e. the more rigid the registration, the worse the accuracy. On this interval, the SCE of the unidirectional TPS-RPM was slightly larger (range of 0.5-2.2 mm) than the SCE of S-TPS-RPM (range 0.5-1.8 mm). For both methods, for $100 \leq \lambda T^0 \leq 10^4$, the SDE had similar values (range of 0.2-2.4 mm). For the entire range of elasticity parameter values and for both methods the ICE, SDE, and SCE decreased with the increase in control point density.

Compared to the unidirectional algorithm the symmetric method improved the inverse consistency of the transformations by $69 \pm 10\%$ (average of percent improvement) and slightly improved the surface coverage (by $13 \pm 11\%$). In addition, the surface distance error was improved for the case of elastic to moderate deformations ($\lambda T^0 \leq 10$) by $26 \pm 18\%$. For the remaining range of the elasticity parameter, there were hardly any differences in the surface distance error obtained with the two algorithms.

For the case of symmetric registration of organs with small volume change, we recommend moderate elastic registrations ($\lambda T^0 = 10$), which provided the lowest surface distance errors, low inverse consistency, and surface coverage errors. Moreover, this value of the elasticity parameter provided low residual

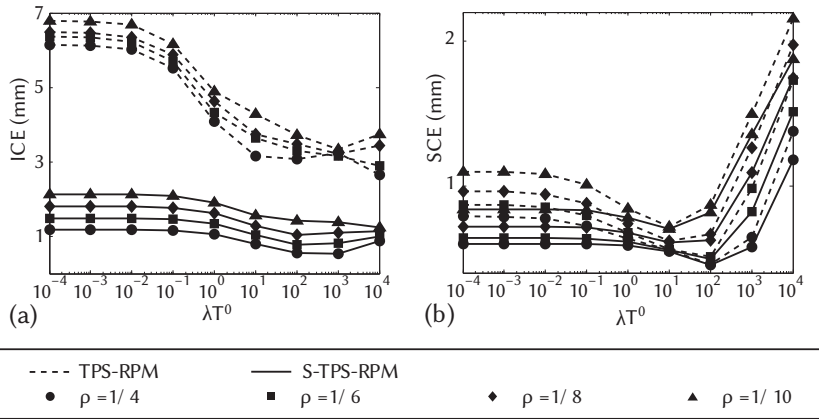


Figure 4.4: Symmetric TPS-RPM vs unidirectional TPS-RPM for the case of registrations with small volume change. a) Inverse consistency error. b) Surface coverage error. The errors are averaged over all patients and iterations. Line: Dashed, TPS-RPM and solid, S-TPS-RPM.

errors at anatomical markers (see section 4.3.3). The averaged values of the SDE, ICE, and SCE for two internal iterations and λT^0 equal with 10 are given in table 4.1.

Table 4.1: Registration errors for S-TPS-RPM for organs with small volume change for $\lambda T^0 = 10$ and two internal iterations.

Density (ρ)	SDE (mm)	ICE (mm)	SCE (mm)
1/4	0.2 ± 0.2 (1 SD)	0.8 ± 0.7 (1 SD)	0.5 ± 0.1
1/6	0.3 ± 0.3 (1 SD)	1.0 ± 0.8 (1 SD)	0.6 ± 0.1
1/8	0.4 ± 0.4 (1 SD)	1.3 ± 1.1 (1 SD)	0.6 ± 0.1
1/10	0.6 ± 0.6 (1 SD)	1.6 ± 1.4 (1 SD)	0.8 ± 0.1

Registration of organs with large volume change

A major advantage of the S-TPS-RPM method lies in its capability to successfully register bladders with large volume differences, while the unidirectional TPS-RPM completely fails in transforming the empty bladder into the full bladder (see figure 4.5(b)). TPS-RPM is unsuccessful because the correspondence is guided by the shortest distances between the transformed

points of an organ, e.g. empty bladder, and the points on the other organ, e.g. large bladder. For the case depicted in figure 4.5(b), after the initialization of the transformation with the identity mapping (see section 4.2.4), the control points on the empty bladder developed weak correspondences with the points on the top of the large bladder, since the top of the large bladder is far away from the empty bladder. Instead, the points on the empty bladder developed strong correspondences with the neighboring points located on the large full bladder. The shortest distances from the points on the top of the full bladder and the surface of the empty bladder were not employed when calculating the unidirectional correspondence matrix. As a result, the unidirectional TPS-RPM fails to map the small bladder into the large full bladder. The symmetric TPS-RPM successfully registered the two bladders (see figure 4.5(c)) because the correspondence takes into account the mutual distances between the points on one bladder and the surface of the other bladder.

For both algorithms, the number of internal iterations had a large impact on the inverse consistency and on the surface coverage error of the transformations from empty to full bladder but had hardly any impact on the surface coverage error of the transformations from full to empty bladders and on the surface distance errors. The surface coverage errors of both algorithms improved with the increase in the number of iterations. Except for one registration case performed with the unidirectional method, the inverse consistency improved with the increase in the number of iterations. Compared to the registration of organs with a small volume change more internal iterations were required (three to five internal iterations for the symmetric method). In addition, accurate symmetric registration was limited to dense sets of control points.

Figure 4.6 depicts the behavior of the inverse consistency error (figure 4.6(a)) and of the surface coverage error (figure 4.6(b)) with respect to the change in elasticity parameter and in density for unidirectional TPS-RPM and S-TPS-RPM with five internal iterations. The sets of control points distributed on the surface of the organs had equal point distribution. The range of the ICE decreased from 15-25 mm for unidirectional TPS-RPM to 2-6 mm for S-TPS-RPM. Similarly, the range of SCE of the transformations from empty to full bladders decreased from 5-13 to 1-8 mm (figure 4.6(b)) and the range of SCE of the transformations from full to empty bladder decreased from 0.5-5 to 0.4-2 mm (data not shown). For each tested value of the λT^0 parameter, the worst ICE and SCE result for S-TPS-RPM (obtained for the smallest number of control points) was better than the best result for TPSRPM method (obtained for the

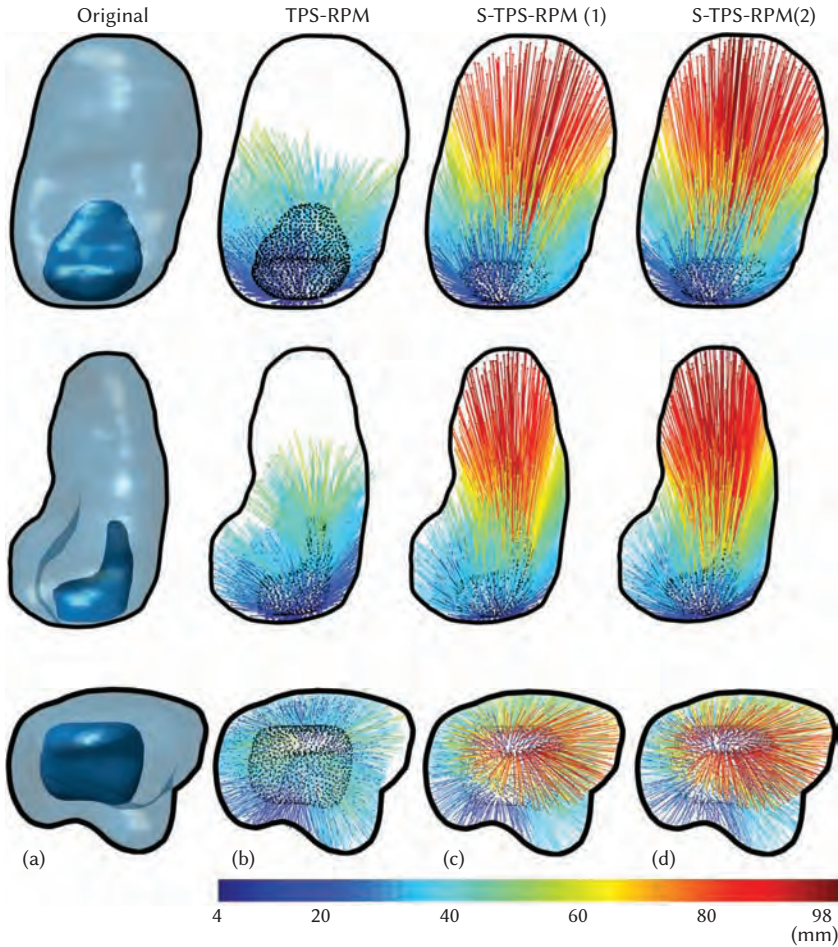


Figure 4.5: Registration of two bladders with a large volume difference. Coronal, sagittal and axial views in the first, second and third row respectively. a) Planning bladder (transparent, black line) and empty bladder (solid color). The volume of the planning bladder is 11 times larger than that of the empty bladder. b-d) Displacement vectors after transforming the empty bladder into the planning bladder with b) TPS-RPM ($SDE=0.7\pm 1.6$ mm, $SCE=17.1$ mm, $ICE=17.3\pm 10.3$ mm, registration time 890s), c) S-TPS-RPM ($SDE=0.3\pm 0.4$ mm, $SCE=1.4$ mm, $ICE=2.0\pm 1.9$ mm, registration time 780s) and d) S-TPS-RPM with better control point distribution ($SDE=0.2\pm 0.3$ mm, $SCE=1.4$ mm, $ICE=1.7\pm 1.3$ mm, registration time 103s). The parameters for b) and c), were $\lambda T^0=1$, $I^0=5$, and $\rho=1/4$ (258 points on the empty bladder and 1373 points on the planning bladder surface). The parameters for d) were $\lambda T^0=1$, $I^0=2$, control point density on full bladder $\rho=1/6$ (699 points), and on empty bladder $\rho=1/3$ (403 points).

highest number of control points).

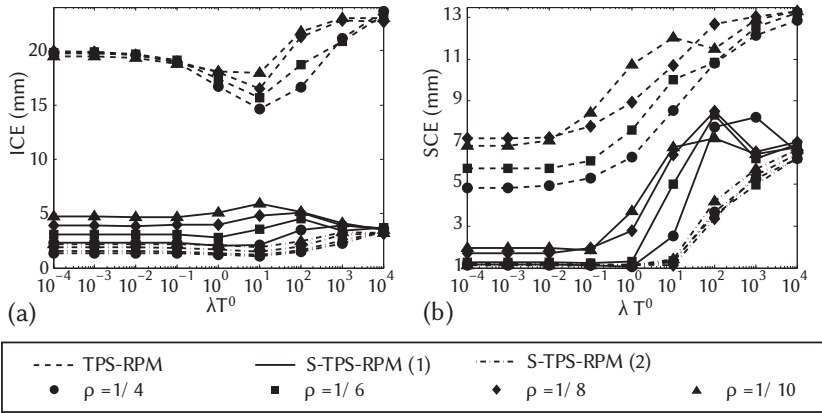


Figure 4.6: a) Patient average ICE for registration of organs with large volume change. b) Patient average SCE of the transformations from empty to full bladders. Line: Dashed, TPS-RPM for $I^0 = 5$; solid, S-TPS-RPM for $I^0 = 5$ and equal point density; and dash-dot, S-TPS-RPM with variable point density and $I^0 = 2$. Symbols represent the density on the largest bladder.

On the interval of flexible transformations ($10^{-4} \leq \lambda T^0 \leq 1$) the range of SDE for the unidirectional TPS-RPM was 0.4-1.5 mm and was larger than the range of SDE for S-TPS-RPM (0.2-1 mm). For both methods, for the remaining range of λT^0 values ($1 < \lambda T^0 \leq 10^4$), the SDE increased with the increase in λT^0 , i.e. the more rigid the registration, the worse the accuracy. For the case of moderate to rigid transformations ($1 < \lambda T^0 \leq 10^4$), the SDE for S-TPS-RPM (range of 0.3-6.5 mm) was slightly worse than the SDE of the unidirectional TPS-RPM (range of 0.3-6 mm).

The magnitude of the ICE, SCE, and SDE depended on the input values of the control point density and of the elasticity parameter. The errors decreased with the increase in control point density. Elastic registrations ($\lambda T^0 \leq 1$) were more accurate than the moderate elastic and rigid registrations ($\lambda T^0 \geq 10$).

Compared to the unidirectional algorithm the symmetric method improved the inverse consistency by $78 \pm 8\%$ (average of percent improvements for all tested parameters). The symmetric algorithm improved the surface coverage of the transformations from empty to full bladders by $49 \pm 27\%$. There was hardly any improvement in the surface coverage of the transformations from full to empty bladders ($19 \pm 20\%$). The improvement in the average of surface coverage errors of the forward and the backward transformations was $46 \pm 24\%$.

The symmetric algorithm could obtain better results with less control points and less internal iterations by distributing control points on the smaller bladder with a density twice as large as on the large bladder, i.e. number of points ratio range of 1-2.2.

Figure 4.6 depicts the behavior of the inverse consistency error (figure 4.6(a)) and of the surface coverage error (figure 4.6(b)) with respect to the change in elasticity parameter and in density for S-TPS-RPM with two internal iterations and improved point distribution. Compared to the initial point distribution the improved distribution reduced the range of the ICE from 2-6 to 1-3 mm and the range of the SCE of the transformations from the empty to the full bladder from 1-8 to 1-6 mm.

The better control point distribution improved the inverse consistency by $43 \pm 20\%$ and the surface distance by $44 \pm 16\%$. There was also a slight improvement of the surface coverage of the transformations from full to empty bladders of $22 \pm 13\%$ and from empty to full bladders of $17 \pm 32\%$. The improved point distribution resulted into stable transformations that were hardly influenced by the change in the number of internal iterations.

For the case of bladders with large volume difference, we recommend flexible registrations with a parameter λT^0 value equal to 1, two internal iterations, and uniformly distributed control points with a number of point ratio between 1 and 2. These values provided submillimeter surface distance and surface coverage errors and low inverse consistency errors. In addition, these parameter values provided low residual values at anatomical markers (see section 4.3.3). The averaged values of the SDE, ICE, and SCE for a number of two internal iterations and λT^0 equal to 1 are given in table 4.2.

Table 4.2: Registration errors for S-TPS-RPM for organs with small volume change for $\lambda T^0 = 1$ and two internal iterations. The indicated density is the control point density on the largest bladder.

Density (ρ)	SDE (mm)	ICE (mm)	SCE (mm)
1/4	0.1 ± 0.2 (1 SD)	1.1 ± 0.9 (1 SD)	0.8 ± 0.1
1/6	0.2 ± 0.2 (1 SD)	1.3 ± 1.1 (1 SD)	0.8 ± 0.1
1/8	0.3 ± 0.3 (1 SD)	1.5 ± 1.4 (1 SD)	0.8 ± 0.1
1/10	0.4 ± 0.4 (1 SD)	2.0 ± 1.7 (1 SD)	0.8 ± 0.1

Anatomical validation

Table 4.3 summarizes the landmark matching results for the cervix and uterus and bladder cases for the recommended parameter values. Compared to rigid alignment, for the case of registration of bladders with large volume change, the unidirectional algorithm and the symmetric method reduced the average marker distance from 70.1 ± 20.1 to 20.7 ± 12.7 and to 3.5 ± 2.4 mm, respectively. The average of the percent of error reduction with respect to rigid alignment was $72 \pm 13\%$ for the unidirectional method and $95 \pm 3\%$ for the symmetric method. For the case of registration of organs with small volume change, the use of nonrigid registration reduced the range of the average marker distance after rigid alignment from $5.8 \pm 2 - 25.8 \pm 14.1$ to a range of $1.8 \pm 0.2 - 9.6 \pm 3.1$ mm for the unidirectional method and to a range of $1.9 \pm 0.2 - 8.5 \pm 5.2$ mm for the symmetric method, respectively. Compared to rigid alignment the average of the percent of error reduction was $44 \pm 37\%$ for the unidirectional algorithm and $48 \pm 37\%$ for the symmetric method.

Table 4.3: Average residual errors for marker registration for rigid alignment, unidirectional (U) TPS-RPM after rigid alignment and symmetric (S) TPS-RPM after rigid alignment.

Residual errors (mm)	Organ / Landmark			
	Bladder	Cervix		
	Top	Tip	Markers	Midline
Planning CT vs 2nd CT scan				
Rigid	70.1 ± 20.1	25.8 ± 14.1	9.2 ± 1.1	12.8 ± 5.1
Rigid + U	20.7 ± 12.7	9.6 ± 3.1	6.8 ± 1.5	4.8 ± 2.2
Rigid + S	3.5 ± 2.4	8.5 ± 5.2	5.7 ± 2.1	4.6 ± 2.1
Planning CT vs 5th CT scan				
Rigid	15.4 ± 10.4	12.1 ± 6.6	5.8 ± 2.0	6.7 ± 2.5
Rigid + U	1.8 ± 0.2	4.5 ± 3.8	6.5 ± 3.6	3.2 ± 1.0
Rigid + S	1.9 ± 0.2	4.9 ± 4.6	6.3 ± 3.6	3.0 ± 0.9

Registration time

Compared to the unidirectional algorithm, for computing both the backward and the forward transformations, the implementation of the symmetric algorithm was computationally efficient, requiring only one correspondence

matrix, whereas the original method needs two. This resulted in an overall $28.5 \pm 10\%$ reduction in the computational time. The average computational time dropped from 275 s for TPS-RPM to 188 s for S-TPS-RPM (in both directions). Compared to the unidirectional method applied in only one direction, the symmetric method required $42 \pm 21\%$ more computational time. A further linear reduction in the computational time was possible for S-TPS-RPM by exploiting the robustness of the algorithm with respect to the number of internal iterations. For example, for the values of the elasticity parameter and density recommended above and two internal iterations, the average registration time of the cervixuterus cases was 35 s (range of 10-75 s) and for bladder 151 s (range of 57-334 s).

4.4. Discussion

4.4.1. Performance of the novel method and recommendations for further use

In this study, we developed, tested, and validated a symmetric point-based nonrigid registration method. The method was used to register the bladder and the cervix and uterus of five cervical cancer patients. Compared to the original unidirectional TPS-RPM method our symmetric algorithm brought three important improvements. First, it allowed the registration of bladders with extreme bladder change for which the unidirectional method failed. Thus, inverse consistency proved to be essential for the case of organs with extreme volume change. Second, a considerable improvement in the geometric accuracy and in the inverse consistency of the registration was achieved. In addition, inverse consistency errors around 1 mm were obtained, indicating that the observed organ changes were independent of the direction of the registration. Third, the efficient implementation and the robustness of the symmetric algorithm allowed for a considerable reduction of the computational time for computing the forward and the backward transformations. This reduction in computational time is important for the applications that can benefit from consistent registration in both directions such as, e.g., dose accumulation for adaptive radiotherapy [142] and allows for a speed up of the quality checks on the consistency of the registration results [133, 132]. The symmetric method was, on average, 42% slower than the unidirectional algorithm applied in only one direction but the symmetric algorithm resulted in more accurate transformations. The developed symmetric algorithm could be used to estimate consistent displacement vectors that describe the direction and the magnitude

of the organ motion in only 35 s for cervix and uterus and 151 s for bladder. This time is well below the computational time requested by biomechanical model-based methods [13] and some intensity-based registration algorithms [21].

In contrast to previous inverse consistent methods [20], our algorithm does not require the additional calculation of the inverses of the forward and the backward transformations. Instead, the symmetric algorithm presented here transforms the two structures toward each other by using a forward and a backward transformation. The correspondence between the landmarks placed on the surface of the two structures is based on the equal contribution of both transformations. A similar principle is employed by the symmetric intensity-based algorithms in which the mean of the intensity gradients of both images drives the registration process [109]. Other symmetric cluster-based versions of the unidirectional TPS-RPM algorithm were implemented for brain registration [27, 26], but experiments to evaluate the inverse consistency were not performed. Moreover, these methods take advantage of specific brain structures and are difficult to be generalized [36].

Since the framework of the TPS-RPM method was fully retained, our algorithm does not require a-priori knowledge of the landmark correspondence. This gives our method an advantage over registration methods for pelvic images that require manual choice of the corresponding landmarks [140, 21]. Moreover, by iteratively updating the correspondence, the issue of extreme organ shape change that could challenge curvature-based algorithms for automatic corresponding landmark selection [13, 64] is avoided. The symmetric algorithm also retained the smoothness constrain imposed on the mappings, i.e., the bending energy, allowing one to express the transformation functions in terms of thin plate splines [10]. Although the bending energy does not have a biological meaning, its associated thin plate splines are widely used to quantify biological shape variations [98]. Alternatively, the mappings could be subjected to other smoothing constrains, e.g. multiple order Laplacian and “stretching energy” [120], or be expressed by using various types of basis functions, e.g. elastic body splines and Wendland functions [63]. Among the abovementioned alternative interpolations, only the generalized splines, based on a multiple order Laplacian, have the potential to be more accurate than the thin plate splines [120, 63]. However, it is unlikely that the best type of generalized spline that would consistently be better than the other splines for all patients and organ deformations can be found [120].

Our method requires as input a homogeneous distribution of control points on the surfaces of the two organs [133]. Although the distribution was

homogeneous, the registration does not result in a homogeneous (uniform) deformation of the organ surface. For example, the method allowed for the registration of empty to full bladder a relatively small expansion of the empty bladder bottom and an extreme expansion of the empty bladder top. The number of points in the sets of control points distributed on the two organs can be different. Here, we found that the accuracy, the inverse consistency, and the computational time were influenced by both the density and the ratio of the number of points of the sets of control points distributed on the two surfaces. The symmetric TPS-RPM gave good inverse consistency results even in the extreme case when the number of points on an organ was five times larger than the number of points on the other organ, i.e., a point ratio equal to 5. This feature gives the symmetric method an advantage over methods that require an equal number of points on the surface of the two organs especially for the case of registration of organs with a large volume difference. However, compared to the case of using large point ratios, better results could be obtained by employing less points and thus in less computational time by using point ratios below 2 (i.e., the recommended number of control points on the surface of the largest organ should be no more than the double of the number of control points on the smaller organ).

Another input of our method is the elasticity parameter λ that indicates the flexibility of the initial organ deformation. This parameter was previously found by repeating the registration process for various values of lambda and by choosing the value that rendered the most accurate results [133]. Tuning the parameter for each case is a tedious task since the organs can show a large inter- and inpatient variability in size, volume, and deformation. To facilitate the search for an optimal input value, we related the flexibility parameter to a variable that is easy to calculate, i.e. the initial temperature (the length of the diagonal of the smallest box encompassing the deforming and the target surfaces). By tuning the method on a set of patient data containing a large interpatient variability in organ shape, volume, and deformation we were able to recommend input elasticity parameters for the two cases of organ registration considered here. For organs with relatively small volume change, i.e. volume ratio smaller than three (which was the case for the large majority of the organ registration tests), a moderate elasticity parameter was recommended. Not surprisingly, the most accurate registrations for bladders with extreme volume change were provided by more flexible registrations.

S-TPS-RPM could easily be applied to other sites, previously registered with TPS-RPM [133], which experience a smaller range of motion and volume

change compared to some of the bladder and cervix-uterus considered here, e.g. head and neck, prostate, and rectum. Currently, the symmetric method is used by our group to simultaneously register multiple structures in head and neck patients observed in CT scans acquired before and after the implantation of brachytherapy catheters [134].

4.4.2. Limitations and further developments

Although our method is computationally inexpensive, implementing algorithms that limit the search for corresponding points to a set of best k neighbors [86] could further accelerate registration. Currently, the applicability of the method for online image guidance is limited by the requirement of segmented structures. However, this is a common limitation of the registration methods that deal with large deformations in the pelvic area [141, 42, 140, 85, 21]. Here, the cervix-uterus and the bladder were manually contoured, which proved a laborious task especially for the case of cervix-uterus (on average, the time required to contour an image set was 1-1.5 h). Autosegmentation algorithms have the potential to reduce the user intervention and to speed up structure extraction in the pelvic area, but are limited by large organ distortion [57]. Although excellent results were obtained for the automatic segmentation of the bladder [57] further research is required to develop and to validate autosegmentation techniques for the rectum and the cervix-uterus.

Our method is a feature-based registration method, which means that the image information away from the contours was not included in the registration. The exclusion of the organ contents by applying imaging manipulation techniques, such as by masking or by image painting, is also employed by intensity-based methods that deal with extreme organ change. Masking the contents of the bladder, rectum [141, 42, 21] or even the prostate [141] and the cervix-uterus [21] is necessary to allow for better mapping of the critical structures. Opposite to the methods that exclude entirely the contents of the organs, the flexible TPS-RPM framework allows for the inclusion in the registration process of a-priori known features (markers, lines, etc.) located inside or outside the critical structures [133]. The validity of the transformation functions away from the surface of the structures included in the registration was not explicitly guaranteed by the symmetric TPS-RPM. In addition, the accuracy of the transformation functions decreases away from the control points used to determine these functions. However, we found that the method performed well in matching anatomical landmarks located inside or on the surface of the registered structures and for the large majority of the cases was better

than the unidirectional method or the rigid alignment. The residual distances that quantify the accuracy of the anatomical markers were affected twofold by the delineation errors. First, the inaccuracies in delineating the organs are carried by the global transformation functions which were used to map the landmarks inside the organs. Second, some of the anatomical landmarks were manually delineated, thus their coordinates contained a residual error prior to registration. However, the landmark matching errors can be further reduced by including the landmarks among the control points used for the registration process [133]. For example, one of our previous studies demonstrated that by using the a-priori information of the correspondence of the anatomical landmarks, the residual errors at those landmarks reduced below 1 mm for head and neck and prostate cancer patients and below 2 mm for cervical cancer patients [133].

Our algorithm could be extended to an intensity-based inverse consistent registration method by employing the methodology of the consistent landmark and intensity-based image registration proposed by Johnson and Christensen [60]. This method matches both landmarks and image areas away from the landmarks, but it relies on a priori defined landmark correspondence [60]. Furthermore, the original unidirectional TPS-RPM method was combined with an intensity-based nonrigid registration algorithm to match images containing a large number of articulated structures [83]. The same methodology could potentially be used to combine our fast symmetric method with an image-based inverse consistent registration algorithm to find a consistent intensity mapping of pelvic images acquired from patients that experience extreme organ deformations.

4.5. Conclusions

A symmetric nonrigid feature-based registration method has been developed, implemented, tested, and validated. Test results demonstrate that our method can successfully be employed to perform fast, accurate, and consistent registrations of organs that exhibit large and complex deformations in cervical cancer patients. Recommendations on the choice of input parameters based on extensive testing and validation on a large set of patient data facilitate the further use of our method.



Chapter 5

Local anatomical changes in parotid and submandibular glands during radiotherapy for oropharynx cancer and correlation with dose, studied in detail with non-rigid registration

Eliana M. Vásquez Osorio, Mischa S. Hoogeman, Abraham Al-Mamgani,
David N. Teguh, Peter C. Levendag and Ben J. M. Heijmen

Published in
International Journal of Radiation Oncology * Biology * Physics
Vol. 70, No. 3, pp. 875-882, 2008

Abstract

Purpose: To quantify the anatomical changes caused by external beam RT (EBRT) in Head and Neck (H&N) cancer patients in full 3D and to relate the local anatomical changes to the planned mean dose.

Methods and Materials: A non-rigid registration method was adapted for RT image registration. The method was applied in 10 H&N cancer patients, who each underwent a planning and a repeat CT scan. Contoured structures (parotid, submandibular glands and tumor) were registered non-rigidly. The accuracy of the transformation was determined. The transformation results were used to summarize the anatomical changes on a local scale for *irradiated* and *spared* glands. The volume reduction of the glands was related to the planned mean dose.

Results: Transformation was accurate with a mean error of 0.6 ± 0.5 mm. The volume of all glands and the primary tumor decreased. The lateral regions of the *irradiated* parotid glands moved inwards (on average 3 mm), while the medial regions tended to remain in the same position. The *irradiated* submandibular glands shrank and moved upwards. The *spared* glands showed only a small deformation (around 1 mm in most regions). Overall, primary tumors shrank. The volume loss of the parotid glands significantly correlated with the planned mean dose ($p < 0.001$).

Conclusions: General shrinkage and deformation of *irradiated* glands was seen. Spared glands showed few changes. These changes were assessed by a non-rigid registration method, which effectively described local changes occurring in the H&N region after EBRT.

5.1. Introduction

Technical improvements in dose delivery and in verification of patient positioning have widened the therapeutic window for radiation treatment of H&N cancer [17, 18, 33, 32, 29, 81]. For example, Intensity Modulated Radiotherapy (IMRT) makes it possible to escalate the dose by conforming the high dose region tightly to the target volume, thereby sparing adjacent normal tissues. In-room imaging devices, such as Cone Beam CT scanners or CT on rails, allow the assessment of non-rigid setup errors in H&N cancer patients [104, 125, 5, 54]. Currently, computer-aided dose optimization is based on a single CT scan, which is acquired prior to the start of treatment. During treatment, significant anatomical changes, including shrinkage of the primary tumor and nodal masses and changes in overall body habitus, have been observed [4, 74, 89]. These changes can cause deviations between the planned and the delivered dose, and may partly undo the benefits of IMRT [49, 71, 30].

So far, mostly global measures, such as volume and position changes, have been used to quantify anatomical changes [4, 49]. Based on a repeat CT study, Robar et al. [108] reported the systematic medial translation of the lateral regions of the parotid glands. This analysis was based on two selected points, one on the lateral and one on the medial border of the gland. In our study, a non-rigid registration method [25] was adapted and used to quantify local soft tissue changes in 10 H&N cancer patients using two CT scans: the planning and a repeat CT scan after 46 Gy EBRT. This method allows soft tissue changes to be assessed in full 3D. Shape and position changes of the primary tumor and the parotid and submandibular glands were quantified. After non-rigid registration, the glands were divided into *irradiated* glands, belonging to a treated neck, and *spared* glands, belonging to a non-treated neck. On the basis of these registrations, in both groups the changes in shape and position during EBRT were summarized on a local scale, by dividing each organ into six regions. Furthermore, volume changes in parotid and submandibular glands were related to planned mean doses.

5.2. Materials and methods

5.2.1. Patient data

Ten consecutive oropharyngeal patients, five men and five women, aged 48-83 (mean 60), treated between November 2004 and December 2005 were

included in this study. Patient characteristic can be found in Table 5.1. The patients first underwent EBRT at a total dose of 46 Gy in 23 fractions (dynamic IMRT), followed by a brachytherapy boost (20 - 22 Gy) [80, 124, 82]. Two intravenous contrast-enhanced CT scans were available for each patient, the planning CT and a repeat CT taken in treatment set-up position two weeks after the end of the EBRT (post-EBRT CT). A posicast mask was used for immobilization during all CT scanning and treatment fractions. The slice spacing was 3 mm for the planning, and 1.5 mm for the post-EBRT scans. Prior to the non-rigid registration, the CT scans were first rigidly matched using the bony anatomy in the region of interest. The primary tumor, parotid and sub-mandibular glands were manually contoured in both CT scans. For consistency, the post-EBRT CT scan was delineated, using the planning CT scan as reference. All delineations were checked by a second observer. The delineated contours were used to create surfaces. These surfaces were defined by a set of triangles joining contours in the consecutive slices.

Table 5.1: *Patients characteristic. Bilateral neck treatment includes both necks, whereas unilateral neck treatment includes only the ipsilateral neck. In all these patients, the ipsilateral neck was located on the right side. Patient 6 received concurrent chemotherapy.*

Patient	TNM stage			Neck treatment	Site
1	T1	N2c	M0	Bilateral	Base of Tongue
2	T3	N2a	M0	Bilateral	Base of Tongue
3	T2	N1	M0	Unilateral (r)	Tonsillar fossa
4	T2	N0	M0	Unilateral (r)	Tonsillar fossa
5	T2	N0	M0	Unilateral (r)	Soft palade
6	T3	N2a	M0	Bilateral	Base of Tongue
7	T2	N0	M0	Unilateral (r)	Tonsillar fossa
8	T1	N1	M0	Unilateral (r)	Tonsillar fossa
9	T3	N3	M0	Bilateral	Base of Tongue
10	T1	N2c	M0	Bilateral	Base of Tongue

5.2.2. Non-rigid registration method

A point-based method for non-rigid registration, known as Thin Plate Splines - Robust Point Matching or TPS-RPM, was modified [25, 131]. This method handles the non-rigid registration as a non-rigid point matching

problem on which the correspondence and the transformation between two points sets, called in this paper *reference* and *deforming* point sets, are optimized iteratively. For an overview of the method see section 3.

We generated sets of points based on the 3D surface of each delineated structure (figure 5.1, step 1, and figure 5.2(a)-(b) for an example). These points defined the boundaries of the structures in the method, and they were distributed nearly homogeneously over the surface using a mean distance of 3 mm. The points were placed within the triangles that described the 3D surfaces. The distance was chosen so that the accuracy of the transformation was adequate to quantify the observed shape and position changes without exceeding the computational resources. Note that the generated points were not restricted to the axial planes of the CT scans.

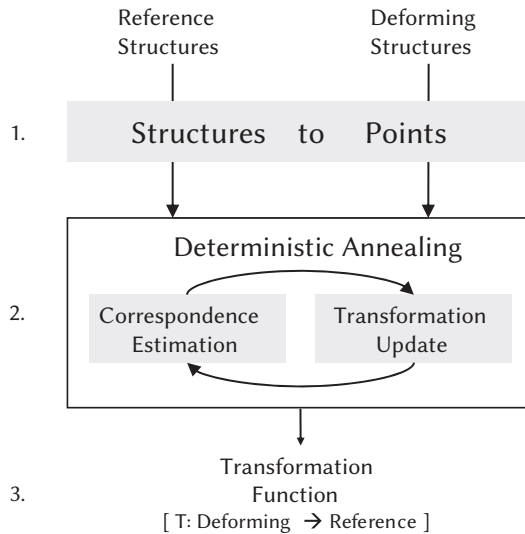


Figure 5.1: Process workflow. Step 1: Generation of points based on input structures' surfaces. Step 2: Non-rigid registration for generating the transformation function. Step 3: Application of generated transformation T to align deforming and reference structures.

The iterative process for generating the transformation function is driven by deterministic annealing (figure 5.1, step 2). This results first in a global and rough approximation, and later in a local and detailed deformation. Each cycle of the process consists of two steps: 1. fuzzy correspondence estimation based on the position of the points, and 2. transformation update based on the correspondence. At the end of each cycle, the positions of the *deforming* points are transformed by the newly found transformation. The annealing process

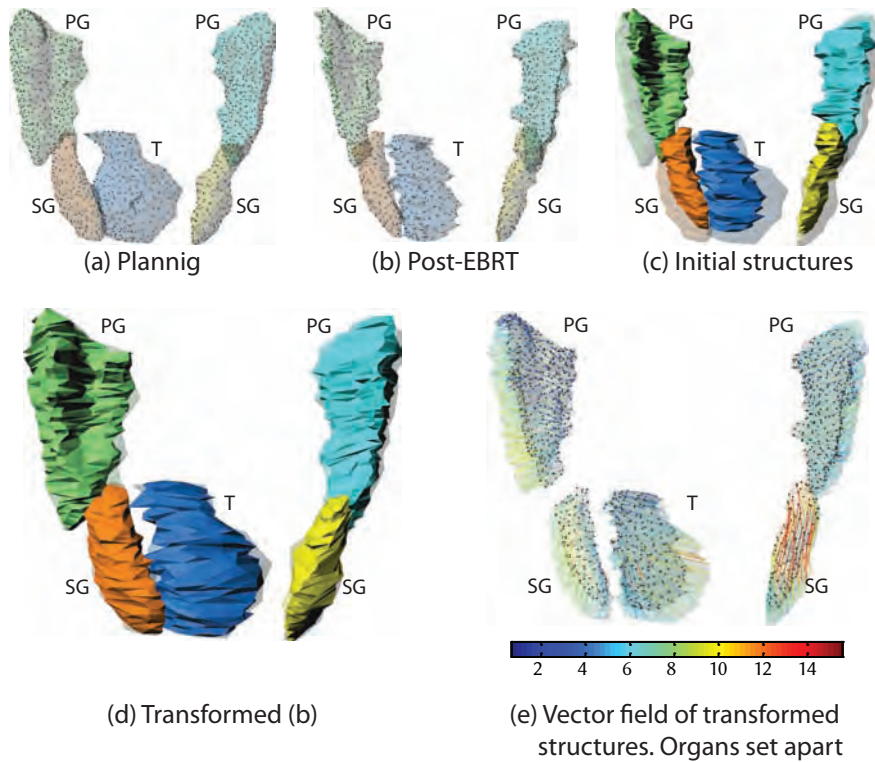


Figure 5.2: Illustration of the steps of the transformation process for one patient (bilateral neck treatment). (a,b): Structures and control points. (c,d): Overlapping structures before and after transformation. Transparent colors: planning, solid colors: post-EBRT. (e) Transformed points (as vectors), organs are separated for visualization. PG: Parotid glands, SG: Sub-mandibular glands, T: tumor.

controls the search range allowed to create the correspondence between the reference and the transformed deforming point sets (global-to-local strategy). At first, every *deforming* point is allowed to correspond to all *reference* points (global fuzzy correspondence). Gradually, the search range is decreased, and as a consequence only *deforming* and *reference* points in close proximity are allowed to correspond. Since the number and precise distribution of the points of the *reference* and *deforming* sets are in general different, no binary one-to-one correspondence is expected to exist between the points of both sets. The correspondence between points is therefore not forced to reach a one-to-one state, but it is limited by the mean distance between the nearest neighbors of the *deforming* points. A pseudo-clustering was implemented to up front avoid

correspondence of points between different organs. The final transformation T transforms the *deforming* point set to resemble the shape of the *reference* point set (figure 5.1, step 3). When the roles of the *reference* and *deforming* point sets are switched in the process, a back-transformation, BT , is generated.

For the final analyses, we created refined surfaces based on the original surfaces. The triangles defining the surfaces were subdivided in smaller triangles, such that their edge length was on average 1.3 mm. Note that the refined surfaces were identical in shape to the original surfaces, but they contained more vertices and these vertices distributed nearly homogeneous.

5.2.3. Patient data analyses

The parotid and submandibular glands were divided into two groups defined by the neck treatment: *irradiated* glands belonging to treated necks, and *spared* glands belonging to non-treated necks. Note that, for each gland type, the *irradiated* glands include five left and five right glands from the bilateral neck treatment, and five right glands from the ipsilateral neck in the unilateral neck treatment. The *spared* glands include five left glands from the contralateral neck in the unilateral neck treatment. Volume changes after treatment were measured. In addition, volume changes of the glands were related to the planned mean dose in the organs.

A transformation T (figure 5.2(d)-(e)), and back-transformation BT were generated for each patient. Note that T and BT are determined for the glands and the tumor of a patient simultaneously, and not for each organ separately. To report the shape and position changes on a local scale, the refined surfaces of each organ were divided into six regions (figure 5.3).

The vertices of the refined surfaces were transformed and back-transformed using the transformations obtained per patient. In order to compare and process the results of the transformation and back-transformation in the same frame of reference, the direction of the resulting displacements of one of the transformations must be inverted (back-transformation in this study). For each of the six regions of an organ surface, all displacements resulting from T and BT were collected, and for each directional component (RL, AP and IS) the average displacement was calculated for each organ region per patient. The displacements per region were then averaged over the patient group, and standard deviations were calculated. Next, results of T and BT were averaged per region. Finally the length of the mean 3D displacement vector was calculated for each region on the basis of the average values of the directional components. These lengths and their corresponding standard deviations,

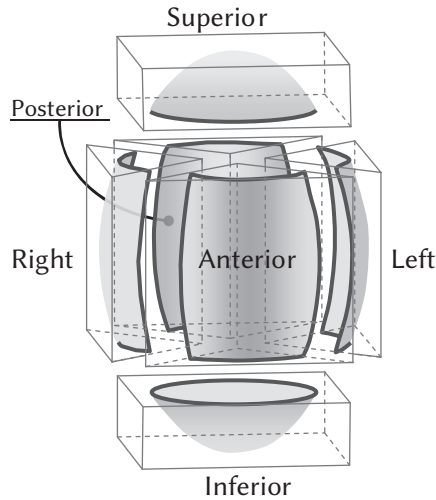


Figure 5.3: Division in 6 regions for a simple ellipsoid. The right, left, anterior, posterior, superior and inferior subvolumes are shown. The superior and inferior boxes contain 20% of the total volume of the bounding box. Four wedges define the remaining (central) volumes. Each subvolume gathers approx. 17% of the total number of organ surface vertices.

describing inter-patient variation, are reported. Note that the changes based on the non-rigid registration, account for deformation and shifts of the glands.

5.2.4. Accuracy of non-rigid registration

The transformation accuracy measures the misalignments between the transformed *deforming* surface and the *reference* surface (figure 5.2(d)). To quantify the transformation accuracy, the distance from each vertex of the transformed refined *deforming* surface to the closest triangle on the *reference* surface was measured and its mean value reported.

There is no explicit drive in the method that makes the back-transformation BT to be the inverse of the original transformation T , but since the input points are the same, this behavior may be expected. Equivalence or near equivalence of the back-projection and the inverse of the original transformation is a minimum condition for application. This equivalence was expressed by the distance between a point and the same point after it was transformed and back-transformed (figure 5.4). In detail, a point P (on the surface) is transformed by the original transformation $T(P) = P^T$. The transformed point P^T is then back-transformed $BT(P^T) = P'$. The distance equivalence d between

P and P' was measured and reported. Note that the distance d also accounts for surface misalignments (due to transformation inaccuracy, see above). When T and BT are inverse functions of each other and there is zero misalignment between the transformed and reference surface, P' and P are mapped to the same position, and d is zero. The equivalence distance d is referred to as the consistency error in other chapters of this thesis.

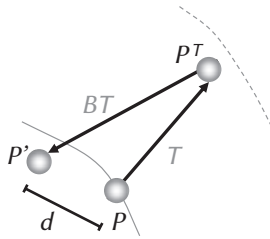


Figure 5.4: Schematic drawing of the transformation and back-transformation of a point P . $P^T = T(P)$ is the transformed P using the transformation T ; $P' = BT(P^T)$ is the back-transformed P^T using the back-transformation BT . d is the distance between P and P' . The distance d is zero when T and BT are the inverse function of each other, and there is no misalignment between transformed and reference surfaces. Deforming surface in solid line and reference surface in dashed line. The equivalence distance d is referred to as the consistency error in other chapters of this thesis.

5.3. Results

Figure 5.5 shows anatomical changes for one of the patients who underwent bilateral neck treatment after EBRT. The space between the skin and the mask in figure 5.5(b) clearly shows anatomical changes possibly caused by weight loss. Also noticeable is the shrinkage and displacement of the contoured organs and tumor (figure 5.5(b)) in comparison with the planning CT scan (figure 5.5(a)). Figure 5.5(c) shows the transformed contoured structures of the planning CT scan together with the post-EBRT structures. The transformed planning structures (shadow) and the Post-EBRT structures (light contours) overlapped accurately.

In all patients, the transformation accuracy (surface misalignment between the *reference* and transformed *deforming* surfaces) was small with an average mean distance of 0.6 ± 0.5 mm (1 SD). These values were independent of organ or direction of the transformation (planning as *reference* and post-EBRT as *deforming* surfaces, or vice versa). The average equivalence distance d (figure

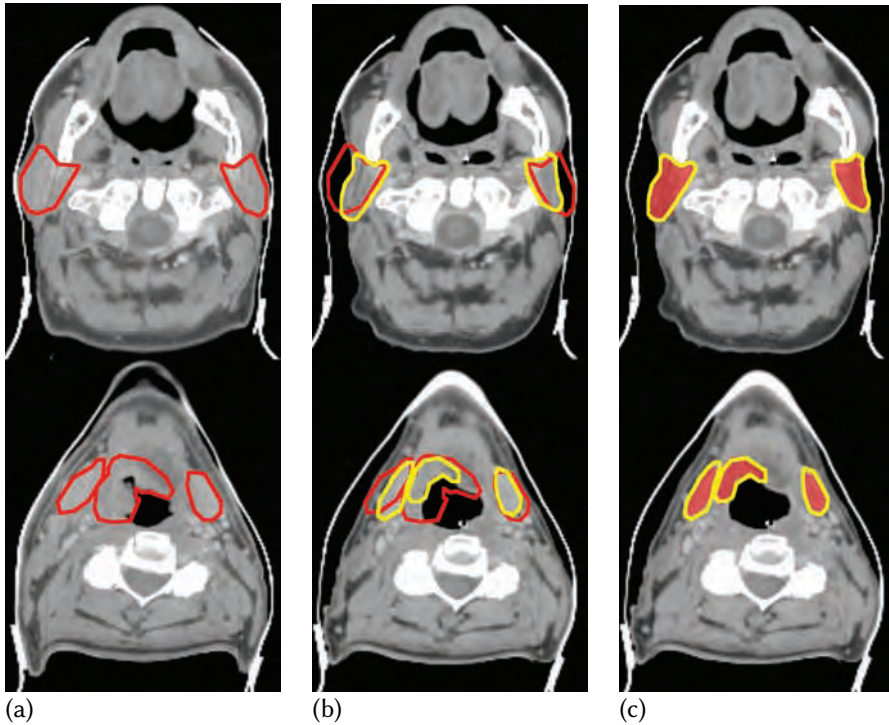


Figure 5.5: Example of observed shape and position changes for a H&N patient (bilateral neck treatment). Shown in the upper slices are the parotid glands and in the lower slices the submandibular glands and primary tumor. (a): planning CT and delineated structures in red. (b): Post-EBRT CT with planning (red contours), and Post-EBRT (yellow contours) delineations. (c): Post-EBRT CT with delineated structures (yellow contours), and transformed planning structures (shadow).

5.4) was also small: 1.5 ± 0.7 mm (1 SD).

5.3.1. Volume reduction

All glands and primary tumors showed a significant reduction in volume. In primary tumors the volume reduction was $25\% \pm 15\%$ (1 SD) on comparison with its original volume ($p < 0.001$, t-test). Volume reductions, as well as average planned mean doses, of the parotid and submandibular glands are summarized in Table 5.2. The volume reduction for *irradiated* glands was significantly larger than the volume reduction of the *spared* glands ($p < 0.001$ for parotid and $p = 0.05$ for submandibular glands, t-test). Also in the unilateral

patients only, the volume reduction of the *irradiated*, or ipsilateral, glands was significantly larger than the volume reduction of the *spared*, or contralateral, glands ($p = 0.02$ for parotid and $p = 0.001$ for submandibular glands respectively, paired t-test). No statistical difference was found in the volume reduction of the *irradiated* glands in patients with unilateral or bilateral neck treatment ($p = 0.6$, t-test).

Table 5.2: Volume reduction with respect to original volume and planned mean dose for irradiated and spared glands. Abbreviations: PARS: parotid glands, SMG: submandibular glands

Gland	Volume Loss		Planned mean dose
	Average \pm 1 SD	p-value	Average \pm 1 SD
Parotid			
<i>Irradiated</i>	17% \pm 7%	< 0.001	25.15 \pm 6.45 Gy
<i>Spared</i>	5% \pm 4%	0.04	6.97 \pm 3.49 Gy
Submandibular			
<i>Irradiated</i>	20% \pm 10%	< 0.001	45.62 \pm 1.87 Gy
<i>Spared</i>	11% \pm 7%	0.03	4.65 \pm 2.49 Gy

When correlating volume changes with planned mean doses, a significant relation was found for the parotid glands ($p < 0.001$, $r = 0.68$, linear regression, figure 5.6). No significant relation was found for the submandibular glands ($p = 0.14$, $r = 0.35$).

5.3.2. Local shape and position changes

The measured average deformations and SD of all ten patients are shown schematically in figure 5.7. The left side of figure 5.7, the solid line, represents the *irradiated* glands; contralateral glands belonging to the *irradiated* group were mapped on the left side of the figure. The *spared* glands are represented on the right side of the figure by the dashed line. The front view (figure 5.7(b)) shows the four glands and the displacement of each visible region after EBRT. Figure 5.7(a) shows the right view (PA-IS projection) of the *irradiated* glands. Figure 5.7(c) shows the left view (AP-IS projection) of the *spared* glands. The arrows represent the direction of the displacement of each region in each projection. The values are the average 3D displacements in mm with standard

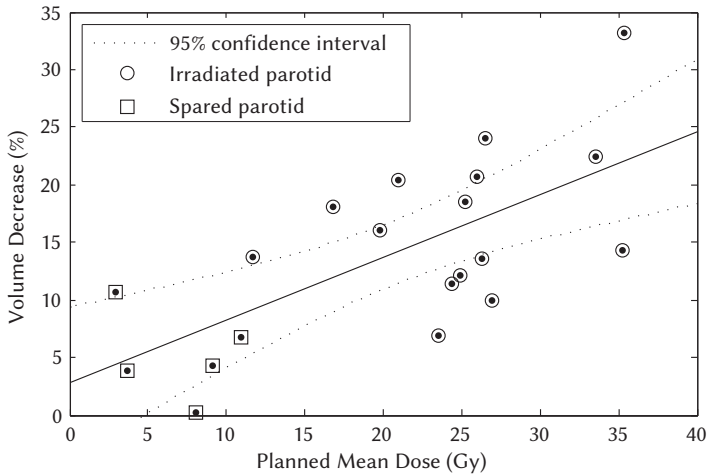


Figure 5.6: Volume changes vs. planned mean dose for parotid glands. Solid line: linear regression ($p < 0.001$, $r = 0.68$).

deviations, where the average was taken over the patient group. The gray areas represent the external lateral walls of the glands.

Shape and position changes of parotid glands

The shape and position changes in all six regions of the *irradiated* parotids were significantly larger than the changes in the *spared* parotids group (max. p-value 0.02, t-test per region, figure 5.7). Within the unilateral group, shape and position changes between the ipsilateral parotid glands were on average larger than the shape and position changes of the contralateral glands, but the differences were not statistically significant. In the *irradiated* group, the parotid glands shrank keeping the regions nearby to bony anatomy as an anchor. All regions showed a tendency to move inwards (right parotid leftwards, and left parotid rightwards). The largest displacements were in the lateral and inferior regions. The region that moved the least was the medial region (partially adjacent to bony structure). *Spared* parotid glands showed translations of on average 1 mm for the superior, lateral and anterior regions, all in a similar direction (inwards and upwards). The posterior region showed zero mean displacement; while the inferior region showed the largest displacement. Figure 5.8 shows a patient who underwent unilateral EBRT, on which the asymmetric shrinkage of the parotids is visible (figure 5.8(b)). There is a clear non-

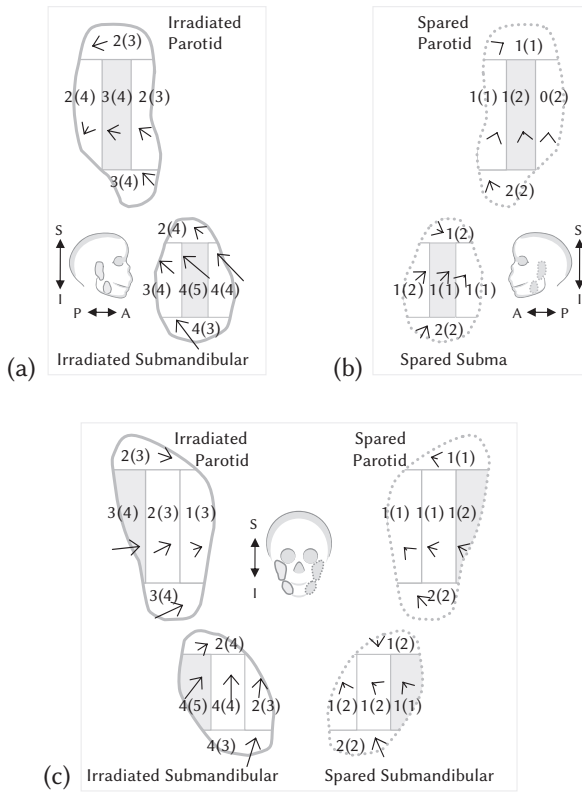


Figure 5.7: 3D lengths of the average 3D vectors and standard deviations for each region in mm. Arrows show the projection of the average 3D deformation vectors in (a) right, (b) frontal, and (c) left views. The solid lines, in (a) and (b), represent irradiated glands (15 parotid and submandibular glands). The dashed lines, in (b) and (c), represent the spared glands (5 parotid and submandibular glands). The external lateral walls of the glands are represented with gray shadows.

symmetrical change in the space between skin and mask.

Shape and position changes of submandibular glands

The shape and position changes in most regions of the *irradiated* submandibular glands were significantly larger than the changes in the *spared* submandibular group (border line significance ($p = 0.06$) for medial region, max p-value 0.05, t-test for other regions, figure 5.7). In the unilateral group, shape and position changes between the ipsilateral and contralateral glands were not

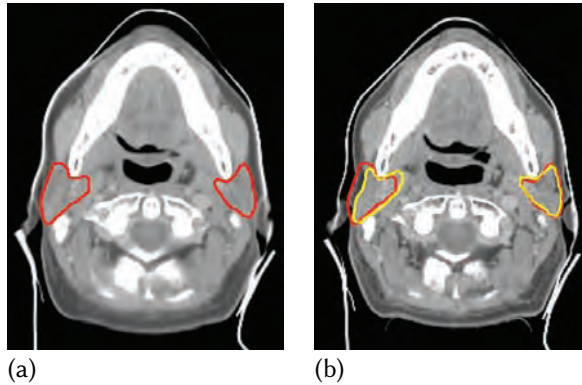


Figure 5.8: Patient with unilateral irradiation (right neck). (a) planning CT scan. Red contours: parotid glands. (b) post-EBRT CT scan. Yellow contours: parotid glands after treatment. Red contours: parotid glands before treatment.

significantly different. In the *irradiated* group, the submandibular glands shrank and moved upwards. The regional displacements in these structures were directed mostly superiorly and posteriorly. The superior and medial regions moved the least. The rest of the regions presented a displacement of between 3 and 4 mm. All regions of *spared* submandibular glands displaced approximately in the same direction as the *irradiated* glands. The magnitude, however, was much smaller: 1 - 2 mm.

Shape and position changes of primary tumor

Results for CTV should be interpreted with care due to the uncertainty related to its localization and the variability of the tumor sites included in the study. The CTV presented a general shrinkage with a pronounced reduction in the posterior region (4 ± 4 mm) mostly in the anterior direction. The displacements in the left region were 3 ± 4 mm rightwards. The region that moved the least was the right region (1 ± 3 mm). The other regions moved on average 2 mm.

5.4. Discussion

The presented non-rigid registration method is a powerful tool to accurately assess local shape and position changes in H&N patients. The measurement accuracy of such changes is determined by the inherent accuracy of the method,

as well as the accuracy and precision of the contouring by the physician. The inherent accuracy was investigated by assessing the transformation accuracy, and the equivalence of the inverse transformation T^{-1} with its corresponding back-transformation BT (expressed as equivalence distance d). The transformation accuracy, defined as the mean distance between *reference* surfaces and corresponding transformed *deforming* surfaces, was 0.6 ± 0.5 mm. The observed small values for d (1.5 ± 0.7 mm) confirm that T^{-1} and BT are nearly equivalent, which is a minimum requirement for clinical application. The displacements found for the *spared* glands have magnitudes in the order of the error of the method.

In an attempt to keep the systematic component of the delineation error small, in this study, the same person delineated both CT scans. Moreover, the planning CT scan was always used as a reference for post-EBRT CT scan delineation. However, some random variations in the contouring of both CT scans are still present. The uncertainty related to contouring mainly affects the CTV, since the contrast between the tumor and its surrounding tissues is very low.

When the found transformation was applied to CT scans, a good alignment between the transformed structures and original contours was found. One should note that the non-rigid registration is controlled by the point sets on the surfaces of the organs. Therefore, the accuracy of the transformation reduces outside the region of interest, since the contribution of the non-rigid components of the transformation decreases further away from the region of interest. Inside the structures only a small misalignment is expected, since the organs are totally enclosed by control points and the volume is relatively small. Kaus et al. [63] showed that for liver, lung and prostate cases, millimeter or even submillimeter accuracy was achieved, measured as the distance between anatomical landmarks. Kaus et al. tested three models, based on thin-plate splines (used in our method), Wendland function and elastic body spline. None of the methods performed consistently better or worse.

The method aligns accurately two sets of structures. When larger areas outside the region of the structure set need to be aligned more structures should be added to the non-rigid process. In theory, the method allows the inclusion of more points, both for defining other organs (such as skin, bony anatomy) or including landmarks. However, the current method is limited by computational resources, such as memory and time, which now is around 1.5 hours per patient on a Pentium IV, 2.8 GHz, with 2 GB RAM. Chui et al. [27] introduced a cluster strategy to increase the amount of information included in the registration

without increasing computational requirements.

Local anatomical changes observed in this study are consistent with the global measurements reported in the literature [4, 49, 108, 75]. Hansen et al. [49] reported a mean change in the volume of 21.5% and 15.6% for left and right parotid respectively, between the planning and second CT scan used for replanning. Volumetric and positional changes for GTVs and normal tissues in relation to the C2 vertebra center of mass were reported by Barker et al. [4], who also found time trends in volume and position of parotid glands. When using the volume decrease rate found by Barker et al. [4] for 23 treatment days, a volume decrease of 13.8% is obtained. The average volume reduction for both parotids in our study was 14%. Barker et al. [4] found a median medial shift of 3.1 mm for the center of mass (COM) of the parotid glands. This medial shift of the COM may partly be explained by our observed asymmetric shifts in parotid gland surfaces, with average displacements of 1 ± 3 mm and 3 ± 3 mm for the medial and lateral regions of the *irradiated* glands, respectively (figure 5.7). Changes in the lateral regions of the parotid were also reported by Robar et al. [108], who found a systematic displacement of a selected point in the lateral region of the parotid glands in the medial direction of 2.6 ± 0.3 mm and -1.9 ± 0.2 mm, for left and right parotid respectively. A selected point in the medial region of the parotid did not show a systematic translation. However, the selection of the same lateral and medial point in a series of CT scans relying on bony anatomy not fully in contact with the parotid gland, may include errors in the measured displacements. In addition, this approach assumes no changes in the inferior-superior or posterior-anterior direction of the parotid glands, which were observed in our patient group (figure 5.7). The full 3D approach used in our study is a more reliable strategy.

Barker et al. [4] found a significant correlation between weight loss and volume change in the parotid glands. Information about weight loss was not collected for this study. However, it is well known that in general patients lose weight during treatment, and we also observed a significant volume loss on the spared glands. Our data show that the planned mean dose is significantly related to the observed parotid gland volume reduction ($p < 0.001$, $r = 0.68$, figure 5.6). Further studies are needed to identify all variables leading to volume reduction.

As suggested by Barker et al., and demonstrated by Hansen et al. [49] and Robar et al. [108], observed anatomical changes may have a dosimetric impact when highly conformal treatment techniques are used. When comparing replanning with no-replanning treatments, Hansen et al. [49] found that doses

to target volumes decreased while doses to normal structures increased. In the particular case of the parotid glands, all dosimetric end points (mean dose, dose to 50% of the volume and volume receiving ≥ 26 Gy) to the right parotid gland significantly increased without replanning, although the changes for left parotid gland were not significant. Robar et al. [108] reported an increase in the mean dose of $2.6\% \pm 4.3\%$ and $0.2\% \pm 4.0\%$ for left and right parotid. The asymmetry in the results between left and right parotid presented by Hansen et al. [49] and Robar et al. [108], show the need to classify the parotid in a way other than left or right; it is possible that the patient groups (14 patients for Hansen et al. and 15 patients for Robar et al.) were not balanced with respect to whether the left and right neck was treated. In our study, a different classification, based on treated or non-treated neck, was used; and we have demonstrated that for *irradiated* parotid glands, the lateral regions (with the lower planning doses) displace inwards, i. e. towards the higher doses; while the *spared* parotid glands present little and near homogeneous deformation.

5.5. Conclusion

The non-rigid registration method accurately described local changes occurring in the H&N region after EBRT in full 3D. The classification of the glands into *irradiated* and *spared* groups, revealed a significant difference in volume reduction and shape and position changes between the groups. Glands belonging to non-treated necks, show few changes. Glands belonging to treated necks showed a general shrinkage and deformation. Non-rigid registration is an ideal tool with which to perform further studies in larger patient series to investigate the relationship between local dose and local shape and position changes in more detail.



Chapter 6

3D dose addition of external beam radiotherapy and brachytherapy for oropharyngeal patients using non-rigid registration

Eliana M. Vásquez Osorio, Mischa S. Hoogeman, David N. Teguh,
Abraham Al-Mamgani, Inger-Karine K. Kolkman-Deurloo, Luiza Bondar,
Peter C. Levendag, Ben J. M. Heijmen

Published in
International Journal of Radiation Oncology * Biology * Physics
Vol. 80, No. 4, pp. 1268-1277, 2011

Abstract

Purpose: To develop and evaluate a method for adding dose distributions of combined external beam radiotherapy (EBRT) and brachytherapy (BT) for oropharyngeal patients.

Methods and Materials: Two CT scans were used for 5 patients: the EBRT CT, used for EBRT planning, and the BT CT, acquired after catheter implantation. For each scan, the salivary glands, chewing and swallowing muscles were contoured, and a dose distribution was calculated. A non-rigid transformation was obtained by registering the organs' surfaces. Then the BT dose distribution was mapped onto the EBRT dose distribution by applying the transformation obtained. To account for differences in fractionation, the physical doses were converted to equivalent dose in 2Gy (EQD_2), and the total dose was found by adding dose voxel by voxel. The robustness of the dose addition was investigated by varying delineations and input parameters of the registration method and by varying the α/β parameter for EQD_2 . The effect of the perturbations was quantified using Dose-Volume Histograms (DVH) and gamma analyses (Distance-To-Agreement/Dose-Difference=1mm/1Gy).

Results: The variations in input parameters and delineations caused only small perturbations in the DVH of the added dose distributions. For most organs the gamma index was low, and moderately elevated for organs lying in areas with a steep gradient (median gamma index ≤ 2.3 for constrictor muscles, ≤ 0.7 for all other organs).

Conclusions: The presented method allows adding dose distributions of combined EBRT and BT for oropharyngeal patients. In general, the method is reliable and robust with respect to uncertainties in organ delineation, perturbations in input parameters of the method and α/β values.

6.1. Introduction

Combination of external beam radiotherapy (EBRT) and brachytherapy (BT) is commonly used in the treatment of head and neck cancer, cervical cancer and prostate cancer [80, 102, 146]. EBRT aims at treating the primary tumor and areas at risk for microscopic disease, while BT is used to boost the primary tumor. However, in current clinical practice, BT boosts are optimized independently, without taking into account the dose already delivered. The reason is that addition of 3-dimensional (3D) dose distributions is challenging due to anatomical changes of the patient, caused by e.g. weight loss, tumor shrinkage, different patient set-ups, implantation of catheters, insertion of applicators or surgical procedures (figure 6.1). Furthermore, to establish dose-effect relationships for tumor control and side effects in combined modality treatments, simple approximations to add dose are often used [3, 123]. Some studies use only the EBRT dose to establish dose-effect relationships [3]. In other studies, the accumulated dose was approximated without taking patient deformations into account. For example, Teguh et al. [123] related the probability of experiencing dysphagia to the dose to the swallowing muscles, where the total dose was found by simply adding the physical EBRT and BT mean doses.

Rigid registration, including rotation and translation, followed by the linear addition of the dose matrices is not accurate to add dose. A rigid transformation does not align deforming anatomy adequately (figure 6.1). Non-rigid registration, on the other hand, allows to better align the anatomy, enabling different dose distributions to be mapped to a common frame of reference. Additionally, different modalities often use different fractionation schemes. Therefore, dose distributions require a conversion to biological equivalent doses before adding the dose in each voxel [119].

In this paper we propose a method for adding 3D EBRT and BT dose distributions, using a non-rigid registration framework developed in-house based on Chui et. al. [25, 133, 7]. To account for the biological effects of the different fractionation schemes, the physical dose distributions were converted to biologically equivalent dose for 2Gy fractions (EQD_2 , [119]) before adding each dose voxel. The method was tested for organs at risk of 5 oropharyngeal patients treated with EBRT, followed by BT boost [80, 123]. The robustness of the dose addition was investigated by variations in input parameters of the registration method, simulating variations in organ delineations around the clinical contours and by varying the α/β value used for EQD_2 .

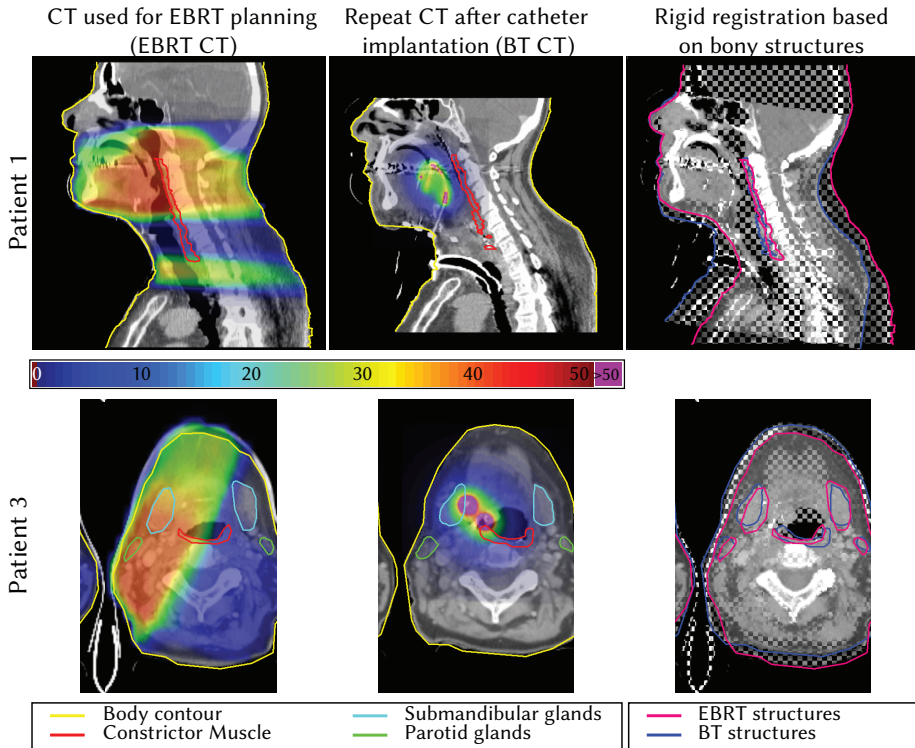


Figure 6.1: Anatomical changes between EBRT and BT for two patients. Rigid registration is not adequate to align both CT scans, as demonstrated by the last column. Large anatomical changes were caused by neck dissection, catheter insertion and different patient positioning for patient 1 (first row), and weight loss for the second patient (second row).

6.2. Material and methods

6.2.1. Patient data

Five oropharyngeal cancer patients were included in this study (table 6.1). These patients belonged to a larger group previously used for quantifying anatomical changes using non-rigid registration [132]. According to the protocol [80, 123], the patients first underwent EBRT to a total dose of 46Gy in 23 fractions (dynamic intensity-modulated RT), followed by a brachytherapy boost two weeks after the end of EBRT (PDR scheme 2Gy+18x1Gy+2Gy, biologically equivalent to HDR scheme 4Gy+4x3Gy+4Gy [68]). N+ patients underwent neck dissection before catheter implantation.

Two intravenous contrast-enhanced CT scans were used for each patient:

Table 6.1: *Patient characteristics.*

Id.	Sex	Age	Site	TNM staging			Notes
1	m	57	Base of tongue	T3	N2a	M0	*†
2	m	48	Tonsillar fossa	T2	N0	M0	‡
3	f	59	Soft palate	T2	N0	M0	‡
4	m	58	Base of tongue	T3	N2a	M0	*†§
5	f	52	Base of tongue	T1	N2c	M0	*†

*both necks treated by EBRT. †patient underwent neck dissection, where among other soft tissue, the submandibular glands were removed. ‡ipsilateral neck treated by EBRT. §patient underwent concomitant chemotherapy.

the CT scan used for planning EBRT (EBRT CT scan), and a repeat CT scan taken two weeks after EBRT, after catheter implantation and just before BT dose delivery (BT CT scan). The slice spacing was 3mm and 1.5mm for the EBRT and BT scans respectively. The catheters were clearly visible in the BT CT since copper wires were inserted before acquisition. The body contour, chewing muscles (masseter, pterygoid and temporalis muscles), swallowing muscles (superior, middle and inferior constrictor, cricopharyngeus, and esophagus inlet muscles) and major salivary glands (parotid and submandibular glands) were contoured in both CT scans. For consistency, the BT organs were delineated, using the EBRT contours as reference. All delineations were checked by a second observer. Surfaces, defined by sets of triangles joining contours in consecutive slices, were created from the delineated structures.

Dose distributions for EBRT and BT were calculated using the treatment planning system used clinically at the time: CadPlan v6.4.7 (Varian Medical Systems, USA) and Plato BPS v14.2 (Nucletron, The Netherlands) respectively. The BT dose distribution was originally calculated based on implant reconstruction from orthogonal X-rays. Here, we reconstructed the BT dose distribution on the BT CT scan. Using the catheters in the BT CT scan, the implant geometry and active dwell positions were determined. The dwell times were copied from the original plan. Finally the BT dose was calculated and the dose grid was exported. Both dose distributions were interpolated to a regular grid (1x1x1mm³).

6.2.2. Dose addition

Figure 6.2 illustrates the steps to add the EBRT and BT dose distributions. First, the triangulated surfaces generated from the delineated structures were used to compute a non-rigid transformation using a non-rigid registration method developed in-house [133, 7]. The non-rigid registration framework was previously validated using anatomical landmarks [133] and was improved to reinforce inverse consistency [7]. The non-rigid transformation, modeled by a regularized thin-plate spline [25], implicitly comprises the changes between the two structure sets by generating a smooth spatial mapping which is constrained by points lying on the organs' surface. Second, we computed the transformed BT dose by inverse mapping using the Insight Toolkit (ITK, [58]). Inverse mapping finds the transformed BT dose in the grid positions of the EBRT dose by transforming each grid position into the BT dose grid using the spatial mapping defined by the EBRT to BT transformation. Then the dose is interpolated at the mapped location using the dose of the closest neighboring BT grid points. Finally, the interpolated value is stored in the EBRT grid position (see figure 6.3). This procedure avoids the creation of empty areas in the transformed dose. Third, the physical doses were converted into biologically equivalent doses for 2Gy fractions (EQD_2) using the linear quadratic model. Finally, the 3D total dose distribution was calculated by adding the converted EBRT dose and the transformed and converted BT dose voxel by voxel.

6.2.3. Simple alternatives to full 3D non-rigid registration

We investigated the validity of approximating the D_1 , mean dose and D_{99} by adding the separate values for the EBRT and BT dose distributions without taking anatomical changes into account. We defined D_1 and D_{99} as the dose received by the 1% and 99% of the organ's voxels respectively, as read from the DVH data. The approximations were converted to EQD_2 and then compared to the values obtained by non-rigid registration.

6.2.4. Robustness of dose addition

As in previous studies [133], each registration produced a non-rigid transformation which aligned the surfaces nicely. This was checked by visual inspection, and by assuring that the transformation error, defined as the mean distance between surfaces, was below 1mm. Previously, we validated the anatomical correspondence of the non-rigid registration framework using identifiable landmarks in CT data sets [133]. The image sets currently used do

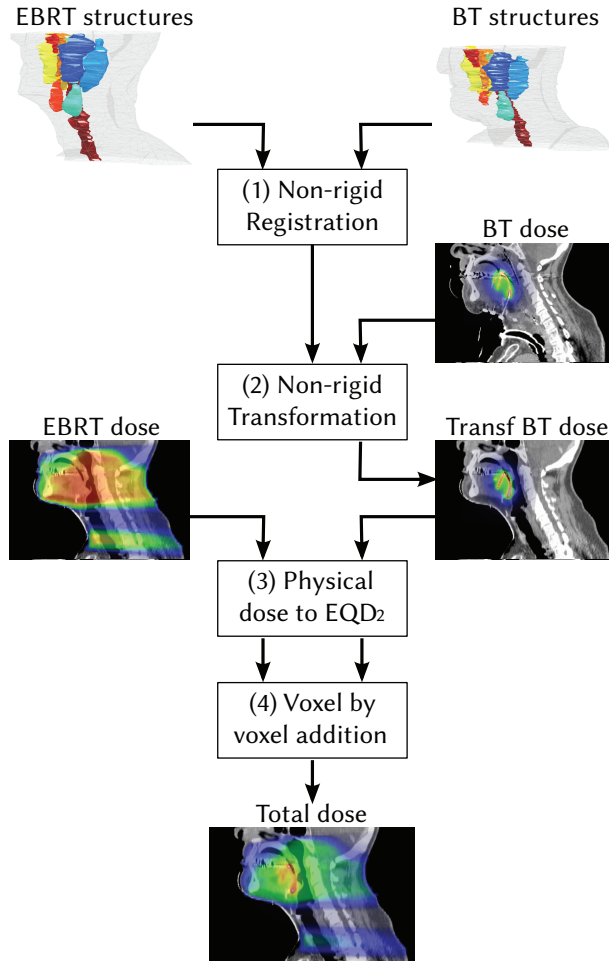


Figure 6.2: Schematic showing the steps for dose addition.

not contain sufficient information to indistinguishably identify corresponding tissue elements on a functional subunit level. Alternatively, we investigated the robustness of the dose addition method with respect to changes in 1) the parameters of the non-rigid registration framework, 2) control point distribution, 3) organ delineation and 4) α/β value used for EQD_2 . To assess the influence of these perturbations, we compared each total dose distribution resulting from each perturbation to a reference total dose distribution using dose-volume histograms (DVH) and the gamma index method [138]. The reference total dose distribution was calculated using the clinical delineations and reference

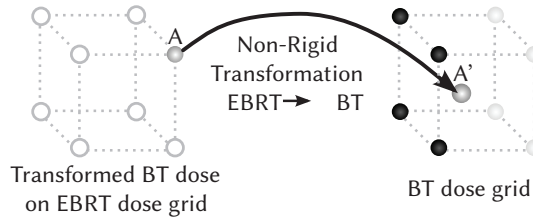


Figure 6.3: Schematic showing the concept of inverse mapping used to map the BT dose to the grid of the EBRT dose. First each grid location (A) is mapped to the BT grid dose (A'). Then, the dose in the mapped location (A') is calculated by interpolating the BT dose in the closest grid points (black and white spheres). Finally, this value is assigned to the grid location A . This procedure avoids the creation of empty areas in the transformed dose.

parameters ($r=5\text{mm}$, $\lambda = 5$ and $\alpha/\beta = 3\text{Gy}$). The gamma index combines the dose-difference (DD) and distance-to-agreement (DTA), to compare two dose distributions (figure 6.4). Gamma index ($\text{DTA}\backslash\text{DD}=1\text{mm}\backslash 1\text{Gy}$) was evaluated in each voxel within the delineated structures. We performed a total of 23 perturbations (see below for details) for each of the 5 patients, including 15 organs per patient, which resulted in 1725 gamma index distributions. We summarized the distributions of gamma indices in box-and-whisker diagrams and reported the percentage of voxels passing the criteria (gamma index ≤ 1).

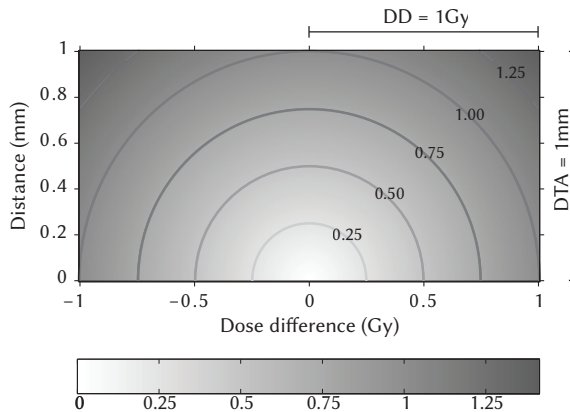


Figure 6.4: Gamma index $1\text{mm}\backslash 1\text{Gy}$ as a function of distance and dose difference between two voxels. Perfect agreement scores zero (same dose and same spatial position). Two voxels with the same dose in locations separated by a distance of DTA (distance-to-agreement), or with the same spatial position and dose difference of DD, scores a gamma index equal to one.

Perturbations of framework parameters

The non-rigid registration framework uses points to represent the structures to be registered. The framework includes a procedure to generate points from surfaces which is controlled by the density radius r . The parameter r determines the density of control points, which affects the computational time and accuracy. Small r means large number of points, longer computational time and, theoretically, more accurate results. Conversely, large r produces few points, shorter computational time and less accurate results. Based on previous experience, we tested $r=5, 6$ and 8mm .

The second framework parameter is λ . This weight parameter controls the degree of deformation of the transformation function by regulating the thin-plate spline used as transformation. Large λ restricts the transformation to be mostly affine, opposite to a small λ , which relaxes the restriction. We tested $\lambda=0.5$ and 5 , which in combination with the used r s (above) produced transformation errors below 1mm in [133].

Perturbations in control point distribution

We investigated the influence of using different control point distributions. As mentioned, the framework includes a procedure to generate control points, which spread pseudo-homogeneously on the surfaces of the delineated structures [133, 7]. In this procedure, a refined surface of the structures is generated by dividing iteratively the triangles that join contours of consecutive slices. The vertices of the triangles already spread pseudo-homogeneously, however registering such a large number of points is beyond the computational resources available. Then, the vertices of the refined triangles are grouped in spheres whose radius is the density radius (r), and the centroid is calculated. Last, the points are replaced by the closest point on the surface to the calculated centroid. By randomly varying the position of the grouping spheres, we generated four control point distributions using $r=6\text{mm}$.

Perturbations in structures delineations

To determine the influence of delineation variations on the non-rigid registration, and consequently on the dose addition, we simulated observer variations of $1, 3$ and 5mm in the delineation of structures. To simulate the variations, random deformations were applied to the surfaces of the EBRT and BT structures (figure 6.5). First, one third of the contour points that constitute the structures' surface was randomly selected. Only points that

were not in close proximity to other organs were considered, in order to avoid overlapping of perturbed contours of neighboring organs. Second, random deformation vectors were generated. In order to simulate the real situation, the deformation vectors were limited to the axial planes where the contours were drawn, and their direction and length was random, to a maximum of the variation simulated (1, 3 or 5mm). Third, the deformation was interpolated to the rest of the structure points using a non-regularized thin-plate spline [10]. Finally, the deformed structures were used in the non-rigid registration framework to generate the non-rigid transformation. We calculated a total of 9 non-rigid transformations per patient, using three random deformations per simulated maximum variation of 1, 3 and 5mm. Calculation of DVHs and gamma analyses were performed using the non-perturbed delineations in order to only assess the perturbations effects on the results of the dose addition.

Perturbations in α/β values

EQD_2 was used to account for differences in the fractionation schemes for EBRT and BT. EQD_2 is based on the linear-quadratic model, and it uses the biological parameter α/β [38]. The α/β value represents the ratio between the radiosensitivity and the repair capacity of a specified tissue. A common value for late reactions is 3Gy, but the precise value is uncertain. We investigated the effect of different α/β values on the dose addition by varying α/β by $\pm 20\%$ and $\pm 10\%$ around the reference 3Gy. We used the non-rigid transformation applied to calculate the reference total dose distribution in order to only assess the effects of α/β variation.

6.3. Results

6.3.1. Total dose

Tables 6.2 and 6.3 summarize the mean doses per organ and patient for EBRT and BT dose distributions, respectively. For all patients, the largest contribution to the total dose came from the EBRT, and most organs at risk received low BT doses. Steep gradients were present in the BT dose distribution, especially within the constrictor muscles (up to 29, 88 and 22Gy/mm for patients 2, 3 and 4 respectively). The gradients were caused by the closeness of implanted catheters to the muscles (figure 6.1).

Figure 6.6 shows the DVHs for the total dose distributions in dashed lines. The largest total doses were found for the constrictor muscles for patients 3 and

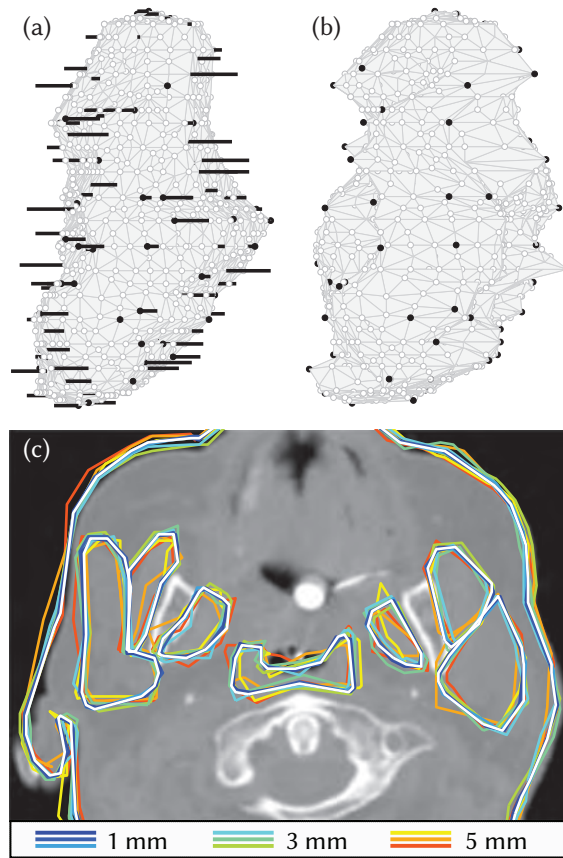


Figure 6.5: Procedure to simulate delineation variations. (a) A set of points is randomly selected (black dots) from the points in the original structure (light triangles). Then deforming vectors, restricted to the axial planes, are generated (thick lines) limiting their lengths to the delineation variation simulated (1, 3 or 5mm). (b) The deformation is interpolated to the rest of the structure using a non-regularized thin-plate spline. (c) BT CT scan of patient 5 showing all 9 delineation variations simulated. The clinical delineation is shown in white.

4, and for the right submandibular gland for patient 3.

We summarized the differences between calculating D_1 , the mean dose and D_{99} taking anatomical changes into account and ignoring anatomical changes in table 6.4. None of the DVH parameters were systematically underestimated or overestimated by the approximation, but large differences were found for D_1 .

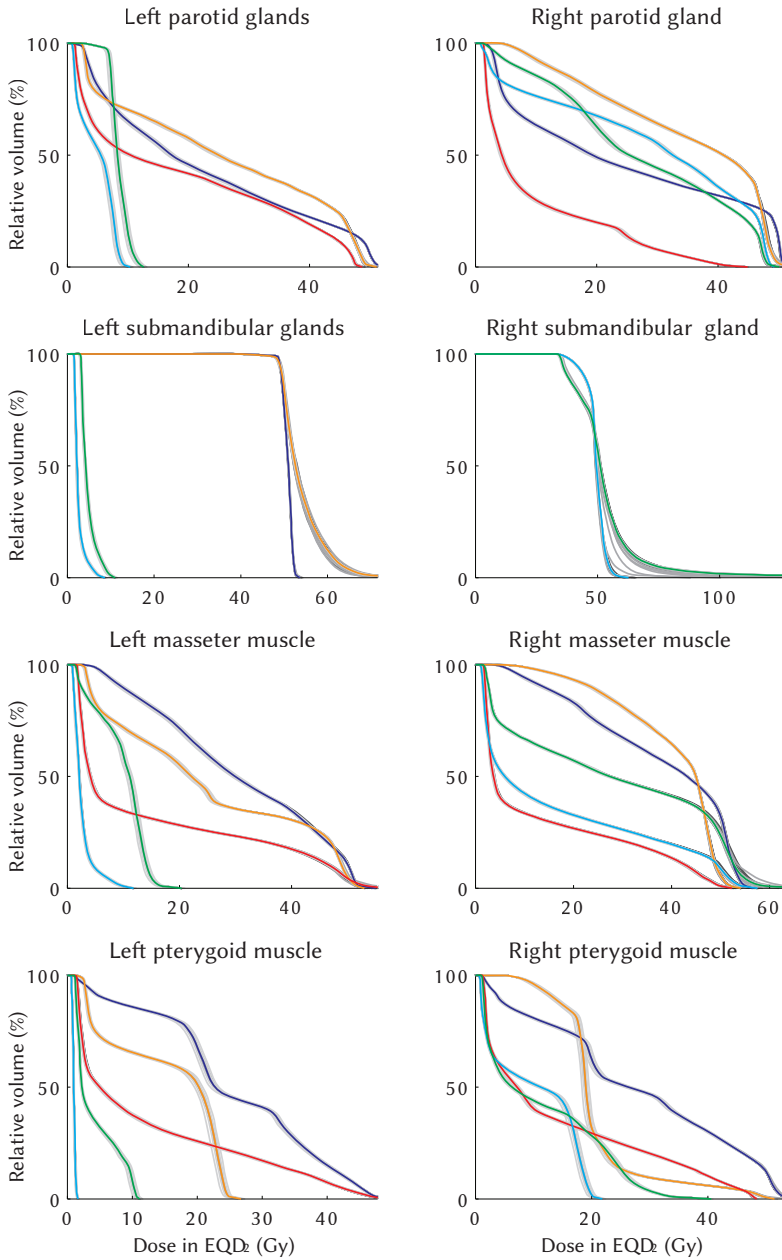


Figure 6.6: Dose volume histograms for the total dose distributions (reference and 23 perturbations). Perturbations on the total dose are shown in different shades of gray, ...

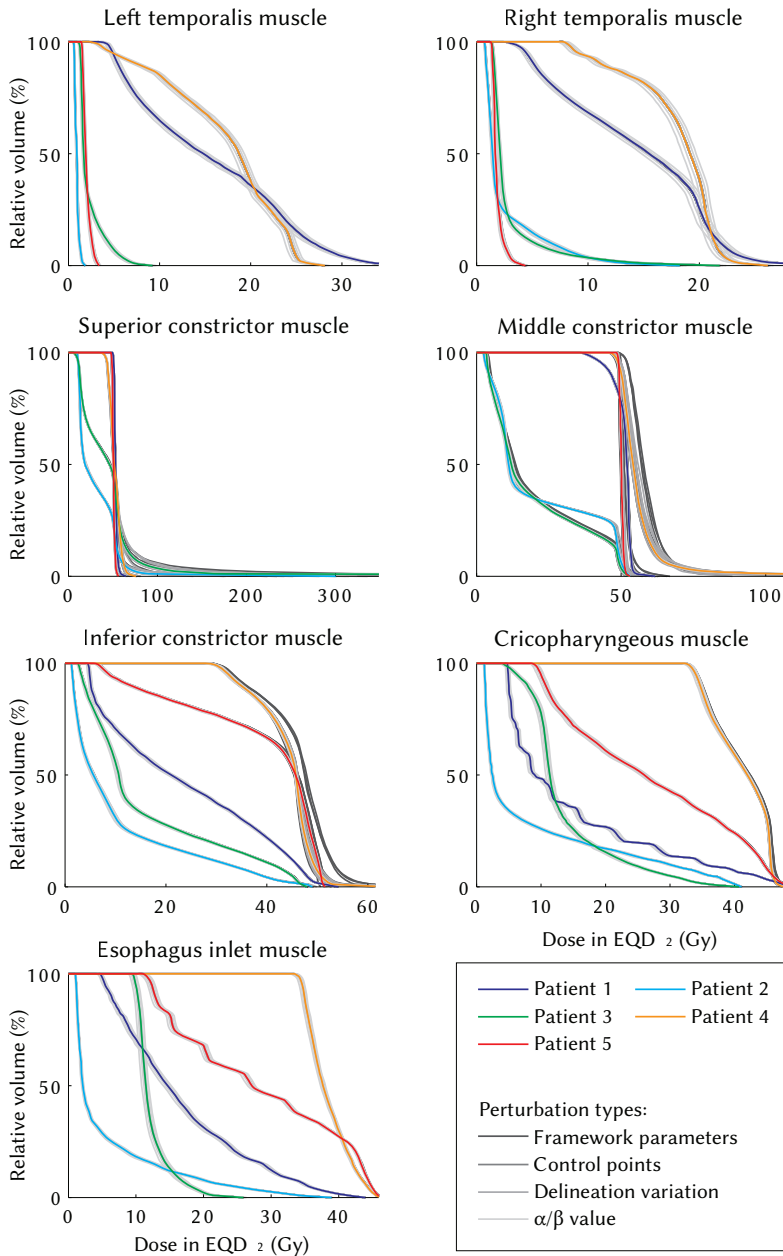


Figure 6.6: ... and most of them blend with the reference DVH curve. Dose axes were cropped to the largest $D_{1\%}$.

Table 6.2: EBRT mean doses for each patient (Pat.), and organ.

	EBRT mean doses physical doses (Gy)				
	Pat.1	Pat.2	Pat.3	Pat.4	Pat.5
Parotid glands					
Left	23.7	6.4	11.4	26.1	19.4
Right	25.3	29.5	29.1	35.3	10.9
Submandibular glands					
Left	47.8	2.5	5.4	44.8	46.5
Right	48.7	45.3	43.6	45.8	46.4
Masseter muscle					
Left	27.1	0.7	5.4	17.6	12.8
Right	28.5	11.4	12.8	23.7	14.8
Pterygoid muscle					
Left	31.1	2.3	12.3	25.6	13.4
Right	36.8	16.1	26.9	39.9	12.7
Temporalis muscle					
Left	18.0	0.5	2.8	20.4	1.3
Right	17.1	2.3	3.0	21.5	1.3
Constrictor muscle					
Superior	47.3	26.7	33.5	44.3	45.7
Middle	47.4	21.4	20.3	44.7	46.7
Inferior	25.1	12.3	18.5	42.4	38.5
Cricopharyngeus	17.5	10.1	17.3	41.6	29.2
Esophagus inlet	20.1	7.4	16.1	39.8	30.7

6.3.2. Perturbations analysis

Besides the DVHs for the reference total dose distributions, figure 6.6 also shows the total dose DVHs for the 23 perturbations in shades of gray. Most perturbations produced only minor deviations with respect to the reference DVHs, to the point that most total dose DVHs blend into one single curve. The largest variations were found for the middle and inferior constrictor muscles for patient 4 (framework parameters perturbation $\lambda = 0.5$), the right submandibular glands for patient 3 (delineation variations of 5mm) and the pterygoid, and temporalis muscles for the α/β perturbations.

Table 6.3: BT mean doses for each patient (Pat.), and organ.

	BT mean doses				
	physical doses (Gy)				
	Pat.1	Pat.2	Pat.3	Pat.4	Pat.5
Parotid glands					
Left	1.4	0.8	0.8	2.5	1.7
Right	1.4	1.5	1.6	2.3	1.5
Submandibular glands					
Left	3.2	1.6	1.9	9.7	9.0
Right	4.6	4.9	9.6	20.7	6.7
Masseter muscle					
Left	2.4	0.9	0.8	2.0	2.7
Right	2.5	2.0	2.0	2.0	2.0
Pterygoid muscle					
Left	3.2	1.7	1.4	2.6	3.8
Right	3.3	3.2	3.7	2.4	3.4
Temporalis muscle					
Left	2.0	1.0	0.8	1.5	1.8
Right	1.9	1.6	1.6	1.4	1.7
Constrictor muscle					
Superior	6.6	7.0	10.6	8.8	6.3
Middle	4.3	4.6	4.7	11.6	4.3
Inferior	2.5	1.9	1.7	6.5	3.4
Cricopharyngeus	1.3	0.8	0.8	2.5	1.8
Esophagus inlet	0.7	0.4	0.6	1.2	1.2

Table 6.4: Differences between approximated $D_{1,}$ mean dose and D_{99} and $D_{1,}$ mean dose and D_{99} calculated using non-rigid registration. All differences in EQD_2 ($\alpha/\beta = 3\text{Gy}$).

Differences (Gy)	DVH parameter		
	D_1	Mean dose	D_{99}
Average (range)	-0.9 (-14.5 - 25.6)	-0.1 (-2.6 - 0.4)	0.1 (-1.7 - 1.5)

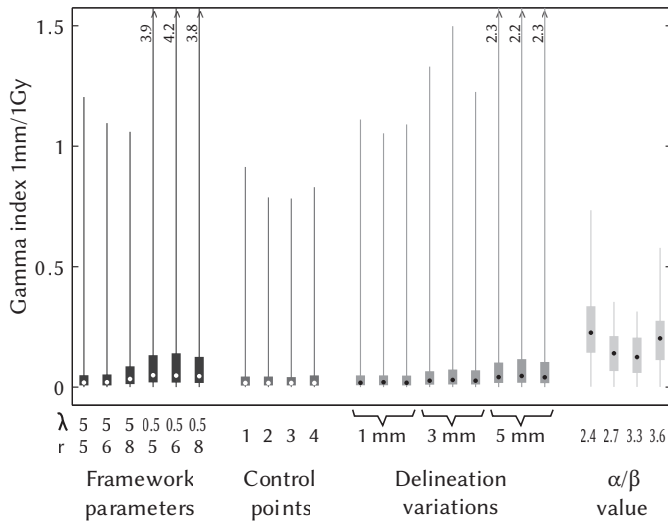


Figure 6.7: Distributions of gamma indices $1\text{mm}/1\text{Gy}$ categorized by perturbation type. The dots represent the median, the boxes extend between the 25th-75th percentiles and the whiskers between 0.1-99.9 percentiles for all voxels of all organs and patients. Whiskers extending beyond the axis are marked with \wedge and their 99.9 percentile is shown next to them.

Figures 6.7 and 6.8 summarizes the distributions of gamma indices of all voxels of all organs and patients (> 21 million voxels) using box-and-whisker diagrams categorizing the data by perturbation type and by organ per patient, respectively. The perturbations in the control point distributions produced the lowest gamma indices. The largest gamma indices were found for $\alpha/\beta = 2.4\text{Gy}$, perturbations using $\lambda=0.5$ and delineation variations of 5mm (medians and boxes in figure 6.7). Results varied among patients. Patient 4 presented the largest variations and patient 1 the smallest, while both were base of tongue cases. All chewing muscles, the parotid glands, the esophagus inlet and the cricopharyngeus muscles, presented small gamma indices for all patients. The organs that presented the most variation were the constrictor muscles and the submandibular glands. Similar results were found when each perturbation was independently analyzed (total 1725 medians, data not shown). The largest gamma indices were found for the middle and inferior constrictor muscle for patient 4, framework parameters $r = 5, \lambda = 0.5$ (medians up to 2.3 and 2.2). For the rest of the organs for all perturbations and patients, the median was below 0.7.

Table 6.5 summarizes the voxels passing the strict criteria of the gamma

Table 6.5: Percentage of voxels passing the strict gamma criteria ($1\text{mm}\backslash\text{Gy}$) for all patients, categorized by perturbation type. Organs that are not shown scored 100(0.0) in all perturbations.

Average(standard deviation) of percentage of voxels which gamma index ($1\text{mm}\backslash\text{Gy}$) ≤ 1 (in %)		Delineation variation				α/β	
Framework parameters		Control	5mm [†]			value [§]	
$\lambda = 5^*$	$\lambda = 0.5^*$	points [†]	1mm [†]	3mm [†]	5mm [†]		
Submandibular glands							
Left	99.4(1.7)	97.7(4.2)	99.6(1.1)	99.5(1.9)	99.2(2.3)	96.2(7.3)	100.0(0.0)
Right	99.2(1.7)	94.2(3.5)	99.8(0.4)	99.0(1.7)	92.2(9.3)	85.3(12.1)	100.0(0.0)
Pterygoid muscle							
Left	100.0(0.0)	99.9(0.2)	100.0(0.0)	100.0(0.0)	100.0(0.1)	99.5(0.9)	100.0(0.0)
Right	100.0(0.1)	98.8(2.3)	100.0(0.0)	100.0(0.0)	99.7(0.7)	99.2(2.4)	100.0(0.0)
Constrictor muscle							
Superior	99.0(2.1)	88.9(11.2)	99.6(0.9)	99.0(1.6)	96.2(3.7)	89.4(10.7)	100.0(0.1)
Middle	98.0(5.3)	69.3(31.3)	99.8(0.5)	98.3(5.4)	99.3(2.5)	89.6(14.9)	100.0(0.0)
Inferior	98.9(2.4)	84.5(29.3)	99.9(0.4)	99.4(1.5)	99.8(0.7)	99.3(1.8)	100.0(0.0)

columns combines ^{*} $r = 5, 6$ and 8mm, [†] $r = 4$ perturbations, [‡] $r = 3$ perturbations, [§] $\alpha/\beta = 2.4, 2.7, 3.3$ and 3.6Gy.

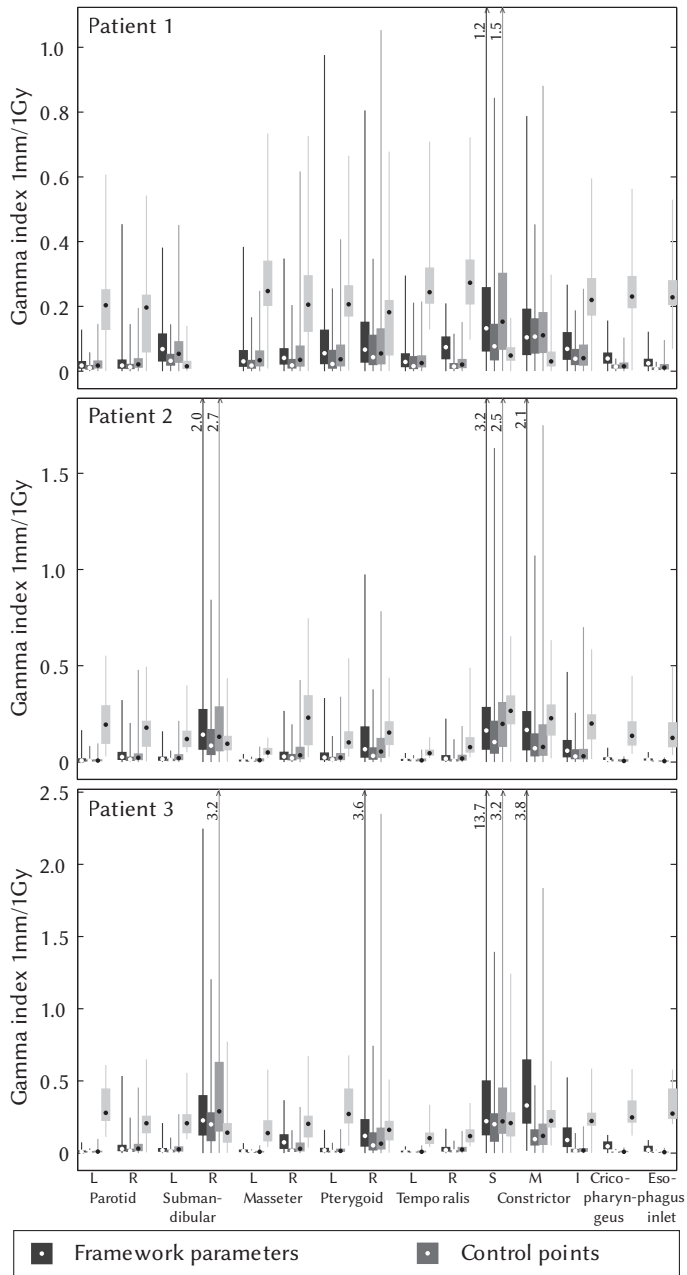


Figure 6.8: Distributions of gamma indices 1mm\1Gy categorized by organs and ...

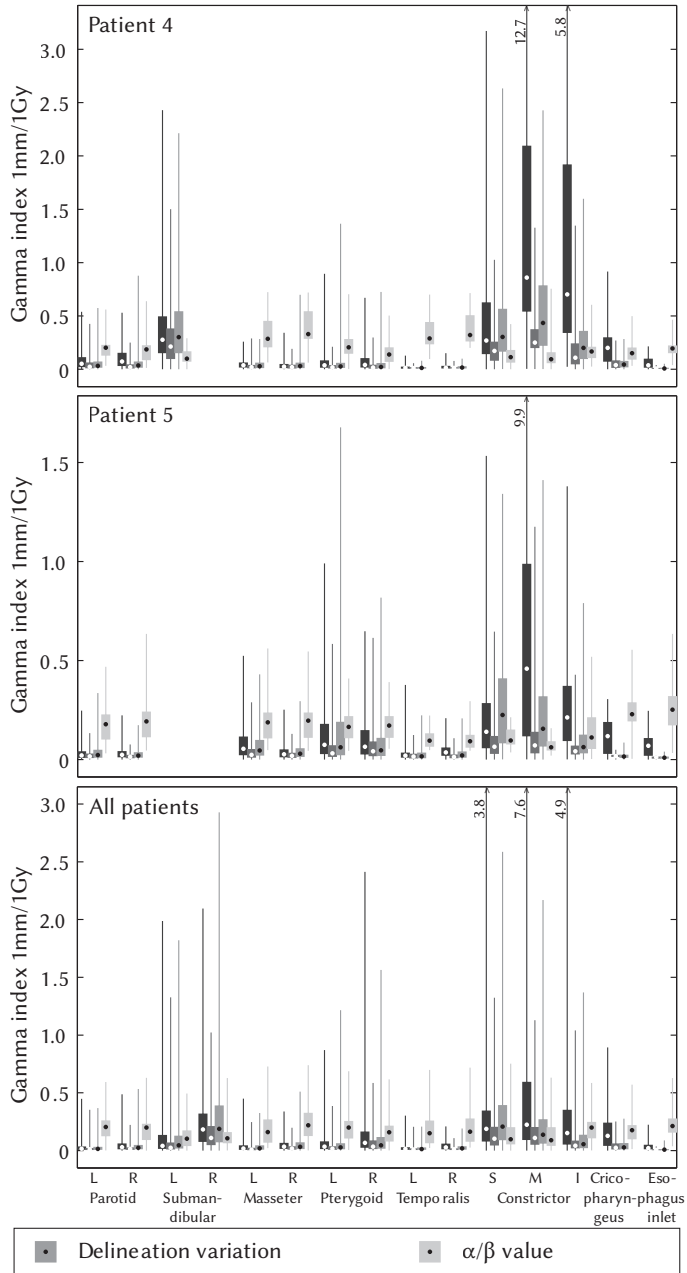


Figure 6.8: ... perturbation type per patient. See figure 6.7 for information on the diagram.

analyses. Most organs score high values. The lowest values were found for the constrictor muscles using $\lambda = 0.5$ and delineation variation of $5mm$, which is in accordance with the data shown in figures 6.7 and 6.8.

6.4. Discussion

We presented a method for adding dose distributions of different modalities taking into account anatomical changes and biological effects. The method was applied to organs at risk of 5 oropharyngeal patients. A robustness analysis was presented as an alternative to validation against ground truth. Overall, the method was robust against perturbations of the input parameters and delineation variations, as demonstrated by the overlapping total dose DVH curves in figure 6.6. Robustness was also investigated by gamma analyses (figures 6.7 and 6.8), comparing perturbed and reference dose distributions using strict criteria, i.e. $1mm\backslash 1Gy$.

Comparing the perturbation types (medians and boxes in figure 6.7), larger gamma indices were found for α/β variations, $\lambda = 0.5$ and for the largest delineation variations ($5mm$). The λ parameter controls the flexibility of the transformation, and a low λ produces a more flexible transformation. Compared to the reference dose distributions, total doses calculated by transformations using $\lambda=0.5$, showed larger local differences, resulting in larger gamma indices (whiskers in figure 6.7). The gamma indices were low for the perturbations in control point distributions, $\lambda = 5$, and delineation variations below $5mm$. Table 6.5 shows similar results for the percentage of voxels passing the gamma criteria, except for the α/β parameter. Although α/β perturbations produced the largest medians and boxes in figures 6.6 and 6.7, they scored 100% of voxels passing the gamma criteria. An explanation is that the α/β perturbation affected the whole dose distribution, but the change was below the criteria used for the gamma analyses ($1mm\backslash 1Gy$). For the organs studied, the variations caused by the α/β perturbations in the total dose distributions were small (below $1Gy$ around $1mm$) and could be seen as clinically not relevant. However, the variations may become greater when adding doses of larger magnitude, due to the quadratic form of EQD_2 .

Large variations were found in the constrictor muscles and some sub-mandibular glands (figures 6.6 and 6.8). These organs were close to the target volume, to the extreme that some catheters run shortly along the swallowing muscles, causing a very steep BT dose gradients within these muscles: up to 29, 88 and $22Gy/mm$ for patients 2, 3 and 4 respectively. The location of these

organs explains the enhanced effect of the perturbations, especially for those where local differences were present (framework parameters and delineation variations), since even small changes in these areas with steep gradients result in very large variations. A possibility to improve the dose addition in areas with steep gradients, is to use a different interpolation method for mapping the BT dose (figure 6.2, step 2), e.g. octant interpolation by Rosu et al. [110].

The concept of accumulating dose using non-rigid registration has been explored in the literature. However to our knowledge, there is no previous attempt to add 3D dose distributions of EBRT and BT taking anatomical changes into account. Few reports are available that address the anatomical validity of dose addition. Schaly et al. [114] proposed to track tissue elements (voxels) between daily CT scans and accumulate their dose distributions using thin-plate spline. In a sensitivity analysis of control point placement, they found dose differences up to 37% for bladder and 27% for rectum. An alternative approach for dose accumulation uses finite element analysis [12]. However, inclusion of anatomical landmarks inside or outside the surfaces is limited, and the mechanical properties for the tissue should be accurate [19].

With respect to the current study, our non-rigid registration method was previously validated using anatomical landmarks [133]. Recently Zhong et al. [149] suggested that using landmark-based evaluation of non-rigid registrations may potentially underestimate registration errors, since large errors can be made in areas with few anatomical features (areas of relatively uniform intensity). In their study, they created a displacement vector field to create phantoms which were registered. The vector field was then used as a ground truth to compare registration results. In clinical practice, or e.g. in our study, such artificial displacement fields are not available for real patient data, and the validation still depends on visual anatomical landmarks. It has been shown in the literature that the registration error increases as its distance from the boundary of organs increases [19, 149]. However, the organs analyzed in the current study are small or narrow, therefore most points are relatively close to the boundary.

The validation for the head and neck cases in [133] used points representing the top and bottom of the glands and lines representing the mandible-parotid gland and styloid process-parotid gland interfaces. These lines lay on the surface, and the points were close to the glands' surface. Therefore, it can be argued that for head and neck cases no validation has been made for points inside the organs. On the other hand, the method was validated for larger organs using internal landmarks (cervix and prostate). Moreover, it

was shown that the results of the method can be improved by incorporating additional anatomical information in the non-rigid registration, such as internal anatomical landmarks, represented by lines or points. As an alternative to anatomical validation, in the current study we investigated the robustness of the dose addition method. To further validate the method, and produce more accurate results, images with better soft-tissue contrast, such as MRI scans could be used. However, it should always be considered that dose addition is an approximation of the true dose accumulation, and that the accuracy of the method should be taken into account when applying it in clinical practice.

In the present study, the total dose to the tumor was not calculated. Besides the large changes happening to the target volume due to catheter implantation, several studies have found that target volumes shrink during EBRT treatment [108]. Dose accumulation for a regressing mass requires further research to handle disappearing tissue properly.

Table 6.4 compiles the differences between approximated D_1 , mean dose and D_{99} (by adding the separate values for EBRT and BT) and D_1 , mean dose and D_{99} using non-rigid registration. Large differences were found for D_1 ($\leq 25.6\text{Gy}$). The differences were smaller for mean dose and D_{99} ($\leq 2.6\text{Gy}$ and 1.7Gy respectively). For large quality of life studies where mean doses are summed up, such as [123], differences of this scale of magnitude are probably negligible. However, this approximation assumes modest deformations which may not hold for other sites. Due to the low number of patients, these results should be interpreted with caution.

Apart from head and neck cases [132], our non-rigid registration framework has been used in other studies to analyze the deformation of the prostate and the seminal vesicles in prostate cancer patients [129] and for cervix cancer patients experiencing extreme deformations as a result of bladder filling variations [8]. Based on this experience and the results described in this paper, we expect our method for dose addition to be applicable to other sites treated with combined modality treatment, e.g. prostate and gynecological sites.

The method can also accumulate dose distributions from other radiation modalities. Dose accumulation can also be used to optimize radiation treatment plans considering dose previously delivered to the patient, e.g. optimizing BT plans taking the EBRT dose into account. Also, using a better total dose approximation, treatment related toxicity and dose-effect relationships can be determined more accurately.

6.4.1. Conclusion

We presented a reliable and robust method that allows adding 3D dose distributions of combined EBRT and BT for organs at risk in oropharyngeal patients. Further improvements, for example in areas with steep dose gradient, can be expected if structures inside the organs can be extracted in the images and used in the non-rigid registration. Optimization of BT plans while taking into account the EBRT dose already delivered, and re-planning in adaptive strategies are promising new possibilities.



Chapter 7

Accurate CT/MR vessel-guided non-rigid registration of
largely deformed livers

Eliana M. Vásquez Osorio, Mischa S. Hoogeman, Alejandra Méndez Romero,
Piotr Wielopolski, András Zolnay and Ben J. M. Heijmen

Submitted to
Medical Physics

Abstract

Purpose: Computer tomography (CT) scans are used for designing radiotherapy treatment plans. However, the tumor is often better visible in magnetic resonance (MR) images. For liver Stereotactic Body Radiation Therapy (SBRT), the planning CT scan is acquired while abdominal compression is applied to reduce tumor motion induced by breathing. However, diagnostic MR scans are acquired under voluntary breath-hold. The resulting large differences in liver shape hinder the alignment of CT and MR image sets, which severely limits the integration of the information provided by these images. The purpose of the current study is to develop and validate a non-rigid registration method to align breath-hold MR images with abdominal-compressed CT images, using vessels that are automatically segmented within the liver.

Methods and Materials: Contrast-enhanced MR and CT images of 7 patients with liver cancer were used for this study. The registration method combines automatic vessel segmentation with an adapted version of thin-plate spline robust point matching. The vessel segmentation uses a multi-scale vesselness measure, which allows vessels of various thicknesses to be segmented. The non-rigid registration is point based, and progressively improves the correspondence and transformation between two point sets. Moreover, the non-rigid registration is capable of identifying and handling outliers (points with no counterpart in the other set). We took advantage of the strengths of both methods and created a multi-scale registration algorithm. First, thick vessels are registered, then with each new iteration thinner vessels are included in the registration (strategy A). We compared strategy A to a straightforward approach where vessels of various diameters are segmented and subsequently registered (strategy B). Residual distances for vessel bifurcations and additional anatomical landmarks were calculated to assess transformation accuracy and for anatomical validation, respectively. To estimate the extent of deformation, the residual distances for the aforementioned anatomical points were calculated after rigid registration.

Results: Liver deformations in the range of 2.8-10.7 mm were found after rigid registration of the CT and MR scans. Low residual distances for vessel bifurcations (average 1.6, range 1.3-1.9 mm) and additional anatomical landmarks (1.5, 1.1-2.4 mm) were found after non-rigid registration. A large amount of outliers were identified (25%-55%) caused by vessels present in only one of the image sets and false positives in the vesselness measure. The non-rigid registration was capable of handling these outliers as demonstrated by the low residual distances. Both strategies yielded very similar results in registration accuracy, but strategy A was faster than strategy B (>2.0).

Conclusion: An accurate CT/MR vessel-guided non-rigid registration for largely deformed livers was developed, tested and validated. Our method, combining vessel segmentation and point matching, was robust against differences in the segmented vessels. We conclude that non-rigid registration is required for accurate alignment of abdominal-compressed and uncompressed liver anatomy. Alignment of breath-hold MR and abdominal-compressed CT images can be used to improve tumor localization for liver SBRT.

7.1. Introduction

Computer tomography (CT) scans play a crucial role in the design of radiation therapy (RT) treatment plans. CT scans are used to localize the tumor and organs at risk, and for dose calculation purposes. However, the structures that need to be included in the optimization process of a treatment plan, are often better visible in magnetic resonance (MR) scans. These structures could be delineated in a MR scan, and transferred to the CT scan under the condition that both image sets are properly aligned. However, aligning the scans is not trivial due to anatomical differences appearing in the image sets. For liver Stereotactic Body Radiation Therapy (SBRT) in particular, cancer lesions are better recognizable and defined in MR scans [95] and considerable anatomical differences occur caused by the use of abdominal compression during CT acquisition and treatment. The abdominal compression is used to reduce the tumor motion that is produced by breathing. For MR scanning, no abdominal compression is applied due to space limitation of the MR scanner. Apart from abdominal compression, inherent anatomical changes caused by physiological reasons, e.g. differences in bowel and stomach filling and weight loss, challenge the aligning of CT and MR scans. Rigid registration, including rotation and translation is not sufficient to align images of deformed anatomy. Non-rigid registration, with more degrees of freedom, has the potential to better accomplish this task.

Inconsistency in image intensities between image modalities adds to the complexity of the registration. The range of intensity values can vary, and the same tissue can be visualized in a completely different way in CT and MR scans, e.g. bony structures. Although non-rigid registration guided by intensity values is commonly used, image quality and resolution may limit its applicability. Alternatively, features present in the images can be extracted and used to align the image sets. By extracting different types of features, different results can be achieved, allowing ‘important’ features to be selected and aligned. Furthermore, users can influence the registration results directly by adding sets of corresponding features, such as delineated organs or anatomical landmarks [133]. In the case of liver, blood vessels can be visualized in different modalities, and they reflect clearly the deformation present in the liver. Especially interesting is the possibility to automate the segmentation of the vessels [78].

In the current study, we propose a method to non-rigidly register CT and MR scans, guided by vessels automatically segmented within the liver. A vesselness measure is used to segment vessels [111]. The registration is based on a modified version of the algorithm previously described in references

[133, 7, 25]. Two strategies for vessel segmentation and registration were investigated (figure 7.1). *Strategy A* is a multi-scale process which starts registering only vessels of large diameter. With each new iteration of the registration, vessels (or parts of vessels) of smaller diameter are segmented and included in the process, and the registration is updated. In *Strategy B*, vessels of all diameters are segmented and registered at once. The strategies were tested and validated using data from seven liver cancer patients. Rigid registration using multi-resolution mutual-information was used to estimate the extent of deformation and the improvement after non-rigid registration.

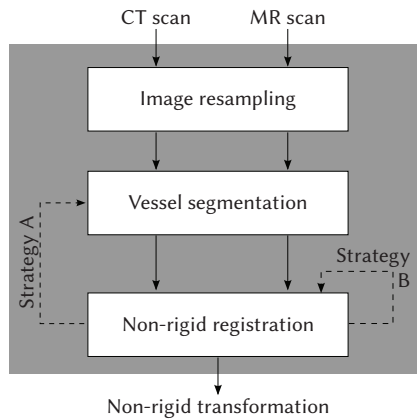


Figure 7.1: Basic schematic of the method. Strategy A segments and registers vessels from thick to thin incrementally. Strategy B segments and registers vessels of varying diameter at once.

In section 7.2.1, the patient data used is described. In section 7.2.2, an overview of the method is given, after which each step is described in more detail; the two strategies are explained in section 7.2.2. Section 7.2.3 describes the validation approach used. In sections 7.3 and 7.4 results are presented and discussed. Finally, conclusions are presented in section 7.5.

7.2. Material and methods

7.2.1. Patient data

CT and MR image data from seven patients with colorectal liver metastases were used. The number of metastases varied from one to three per patient. Three patients underwent liver resection of different segments in the past.

Patient 3 underwent resection of the lateral lobe (segments II and III). Three patients underwent concurrent chemotherapy. All patients were treated with external beam radiation in a stereotactic body frame (SBF) [139, 96, 97, 128]. MR scans were acquired for diagnostic purposes, and were later used to assist tumor delineation in the CT scan. MR scans were acquired after gadolinium administration and carried out in breath hold position (exhale) [95]. Five patients had a dynamic MR series, each MR series resulted in a total of six image sets. The image set where the vessels and lesions were the most visible was chosen. A contrast-enhanced CT scan in venous phase was acquired approximately two weeks after the MR scan. All CT scans were acquired under abdominal compression.

The in-plane resolution of the images varied between 0.98×0.98 and 1.27×1.27 mm² for the CT and 0.64×0.64 and 1.88×1.88 mm² for the MR scans. The inter-slice resolution was 2.5 mm for the CT and varied between 2.0 and 4.0 mm for the MR scans. CT image quality was compromised by high levels of noise (for all patients except patient 4), low contrast-to-noise ratio (especially for patients 2 and 3) and streak artefacts caused by metal markers (for patients 3-6). For MR scans, very strong gradients (especially intense for patients 1, 2 and 5) and artefacts produced by residual respiratory motion (patients 4) were present (see figure 7.2).

7.2.2. Segmentation and non-rigid registration

A basic schematic of the method is shown in figure 7.1. In general terms, vessels inside the liver were automatically segmented and then registered. To mask the liver in the CT and MR scans, coarse contours were manually delineated and used. Vessel segmentation was done using a multi-scale vesselness measure [111]. The midlines of the vessels were registered using an adapted version of the non-rigid registration method previously described in references [133, 7]. The transformation function obtained was used to align the image sets.

The vesselness measure can identify vessels of a given diameter or vessels of varying diameters. Based on this characteristic, two strategies were implemented and evaluated: *Strategy A* and *Strategy B*. *Strategy A* starts segmenting and registering only ‘thick’ vessels, and with each new iteration, vessels (or parts of vessels) of smaller diameter are included in the process. In contrast, *Strategy B* segments vessels of all diameters and then registers them. Detailed schematics of the strategies are depicted in figure 7.3 and more information is given in section 7.2.2. Each component is explained in more

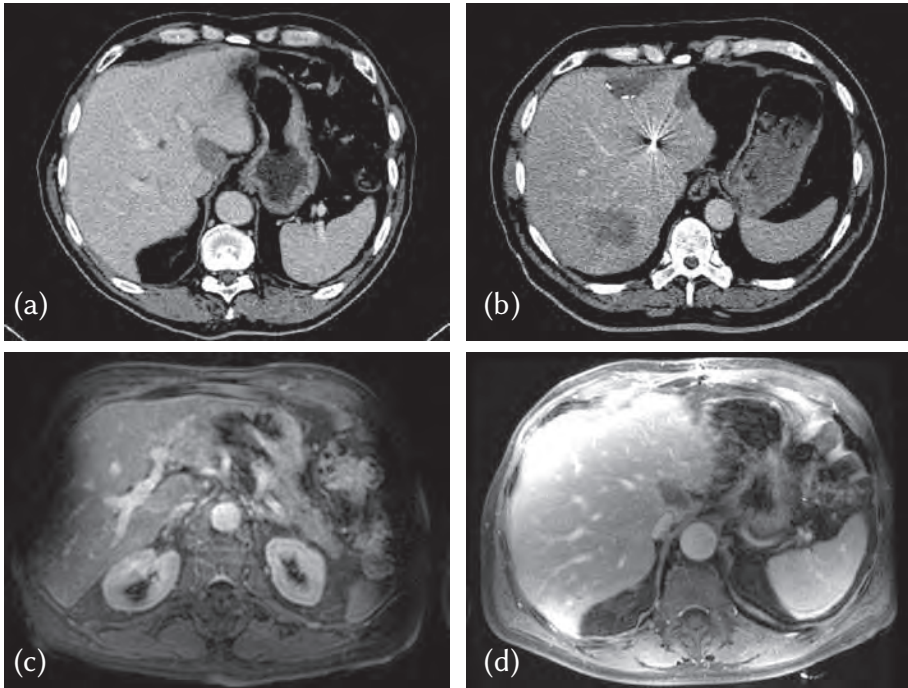
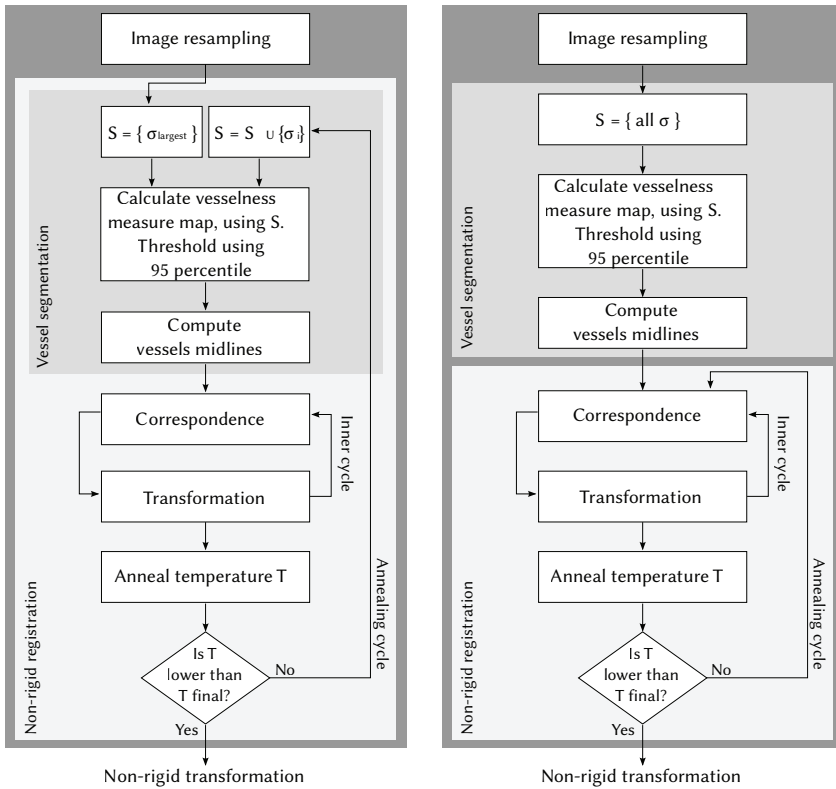


Figure 7.2: Examples of artefacts present in (a,b) CT and (c,d) MR scans. (a) Low contrast-to-noise ratio making the vessels poorly visible, (b) streak artefacts caused by metal markers. (c) and (d) strong gradients in image intensity within the liver.

detail in the following sections. The components were implemented in Matlab and the insight toolkit (ITK), and interfaces between them were file-based. Execution times are reported.

Image resampling

The region that included the liver in the CT and MR scans was interpolated to a grid with a resolution of $1 \times 1 \times 1 \text{ mm}^3$. We used the windowed sinc function, which provides minimum aliasing artefacts in contrast to linear interpolation [94]. The Lanczos was chosen as kernel function, and the window radius was set to five.



(a) Strategy A: from thick to thin

(b) Strategy B: all vessels at once

Figure 7.3: Detailed overview of the method. Two strategies were designed: (a) from thick to thin vessels. (b) all vessels at once.

Multi-scale vesselness measure

We used a multi-scale vesselness measure to segment the vessels in the liver for both the CT and MR images [111]. Intuitively, the vesselness measure indicates how similar the surroundings of a given voxel are to a tube. When the vesselness measure is calculated for each voxel of an image, these compose the vesselness measure map.

Several vesselness measures have been proposed in the past [111, 39, 91]. These measures have in common that they are based on the relationship of eigenvalues of the Hessian matrix. The Hessian is a square matrix, $n \times n$, of second-order partial derivatives of a function f of n variables, and it describes the local curvature of f . In the case of image data, the Hessian

matrix describes the second-order structures of local intensity variations. The eigenvalues/eigenvectors of the Hessian matrix identify the principal curvatures of f , which can tell the directions and magnitude of maximum and minimum intensity variations for image data. When inside a tubular structure, the intensity variation along the tube is small (e_1 in figure 7.4), whereas the variations are large in the other two orthogonal directions (e_2 and e_3 in figure 7.4).

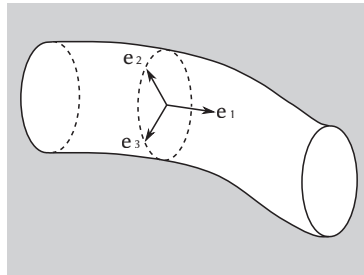


Figure 7.4: Relationship of the eigenvectors of the Hessian matrix inside a tubular structure. The eigenvector (e_1) pointing to the direction of the vessel corresponds to the smallest eigenvalue. The other eigenvectors (e_2 and e_3) lie on the cross-sectional plane. The vesselness measure is calculated by combining the three eigenvalues.

For 3D images, the Hessian matrix can be computed using the convolution of the image with the second and cross derivative of a Gaussian function, which uses the parameter σ as standard deviation [31, 88]. By varying the σ parameter, the vesselness measure for different vessel thickness can be computed (see figure 7.5). Small σ values identifies thin vessels while large σ values finds thick vessels (first and second columns in figure 7.5). Furthermore, vessels of varying diameter can be identified when vesselness measures of different σ s are combined ([111], last column in figure 7.5). Notice that the vesselness measure for small σ s (first column in figure 7.5) produces more false positives and is more sensitive to noise. Also, small vessels can be lost after combining different vesselness measure maps (last column in figure 7.5). For information about segmenting vessels from a vesselness measure map, please refer to section 7.2.2.

We experimented with different vesselness measures, and found that Sato's vesselness [111], as implemented in ITK¹, behaved the best for our data. All results were obtained using five σ values, between 2 and 4 mm. To cope with the large noise, the images and resulting vesselness measure maps were smoothed

¹ Hessian3DToVesselnessMeasureImageFilter class

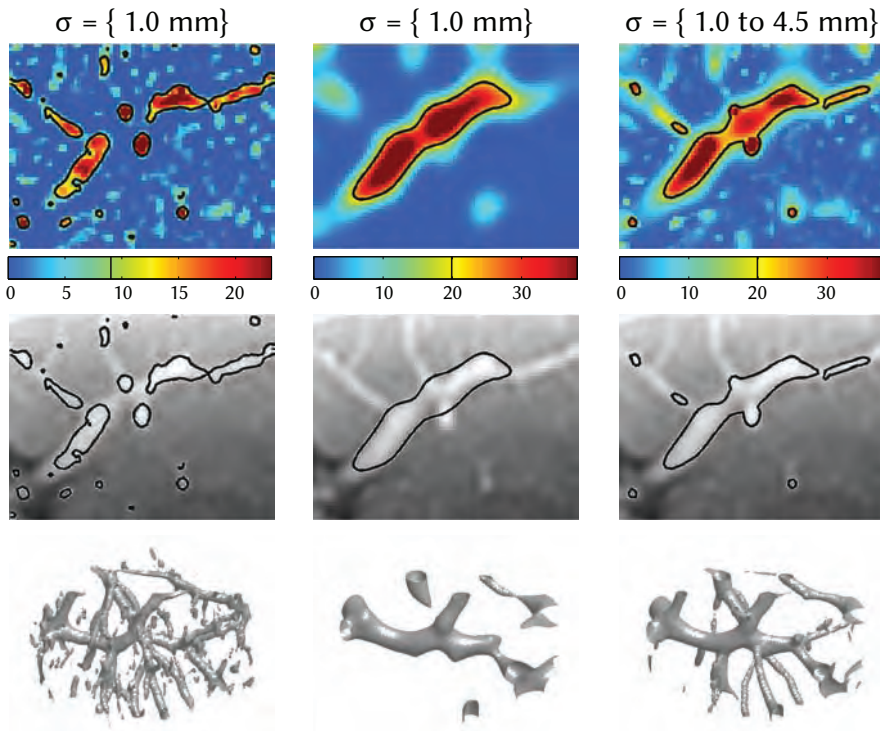


Figure 7.5: Multiscale vesselness measure maps (first row) and segmented vessels (second and third rows) using different σ s for a small region of the MR scan of patient 5. ‘Thin’ vessels can be segmented using small σ as depicted in the first column, while ‘thick’ vessels require a larger σ , second column. Vessels with varying diameters can be segmented by combining vesselness measure maps of different σ s, as shown in the last column using five σ values between 1.0 and 4.5 mm.

using a Gaussian filter with standard deviation of $\sigma/2$. The vesselness measure maps were only computed inside the liver.

From vesselness measure to vessel surface

After calculating the vesselness measure map for one or more σ values, the vessels were segmented by applying a threshold to this map. As threshold, we used the 95 percentile of the vesselness measures within the liver. Following this procedure, most vessels were segmented (see contours and 3D surfaces in figures 7.5 and 7.6). False positives were found for areas close to the organ’s surface but still inside the mask for both CT and MR scans (see arrows in figure

7.6(f)). Moreover, false positives were found at streak artefacts of implanted markers and in areas close to the falciform ligament in the CT scans (see arrows in figure 7.6(c) and (e)). For some areas with a very high gradient and a high intensity value in the MR scans, false positives were observed as well (see arrows in figure 7.6(d) and (f)). For two patients with very strong marker artefacts in the CT scans, the marker and the streak artefacts were filtered out from the image data beforehand.

From vessel surfaces to midlines

Vessels can look different in the CT and MR scans. Apart from the inherent differences between CT and MR, e.g. modality-specific artefacts and soft-tissue contrast, other differences arise from differences in contrast enhancement. These differences lead to a variation in the apparent diameter of the vessels between both modalities. To avoid misleading the registration, but also to simplify the registration, we used the midlines of the vessels instead of the vessel surfaces for the registration (see figure 7.7).

The vessel midlines were generated by thinning binary images. The binary images are the direct result of applying the threshold of 95 percentile to the vesselness measure map (see section 7.2.2). The general idea is to iteratively erode the binary image until only the skeleton is left [77]. We used the implementation in ITK [53]. The result of this filter is a binary image, where the voxels belonging to the midline are marked as '1', and the rest '0'. The voxel coordinates were extracted and used as input for the non-rigid registration.

Non-rigid registration

The method used is an adapted version of the method described in references [25, 133, 7]. It is a point-based non-rigid registration, which iteratively estimates the point correspondence and updates the non-rigid transformation. The structures to be registered are represented by two sets of points: the *reference* and the *deforming* point sets. The point correspondence is modeled by soft-assignment, which allows n reference points correspond to m deforming points. The transformation is defined by a thin-plate spline, which is regularized by the parameter λ to avoid unnatural transformations. The correspondence and transformations for both directions (reference to deforming set and deforming to reference set) are calculated simultaneously. The non-rigid registration procedure is fully automatic and does not require user interaction or any manual initialization.

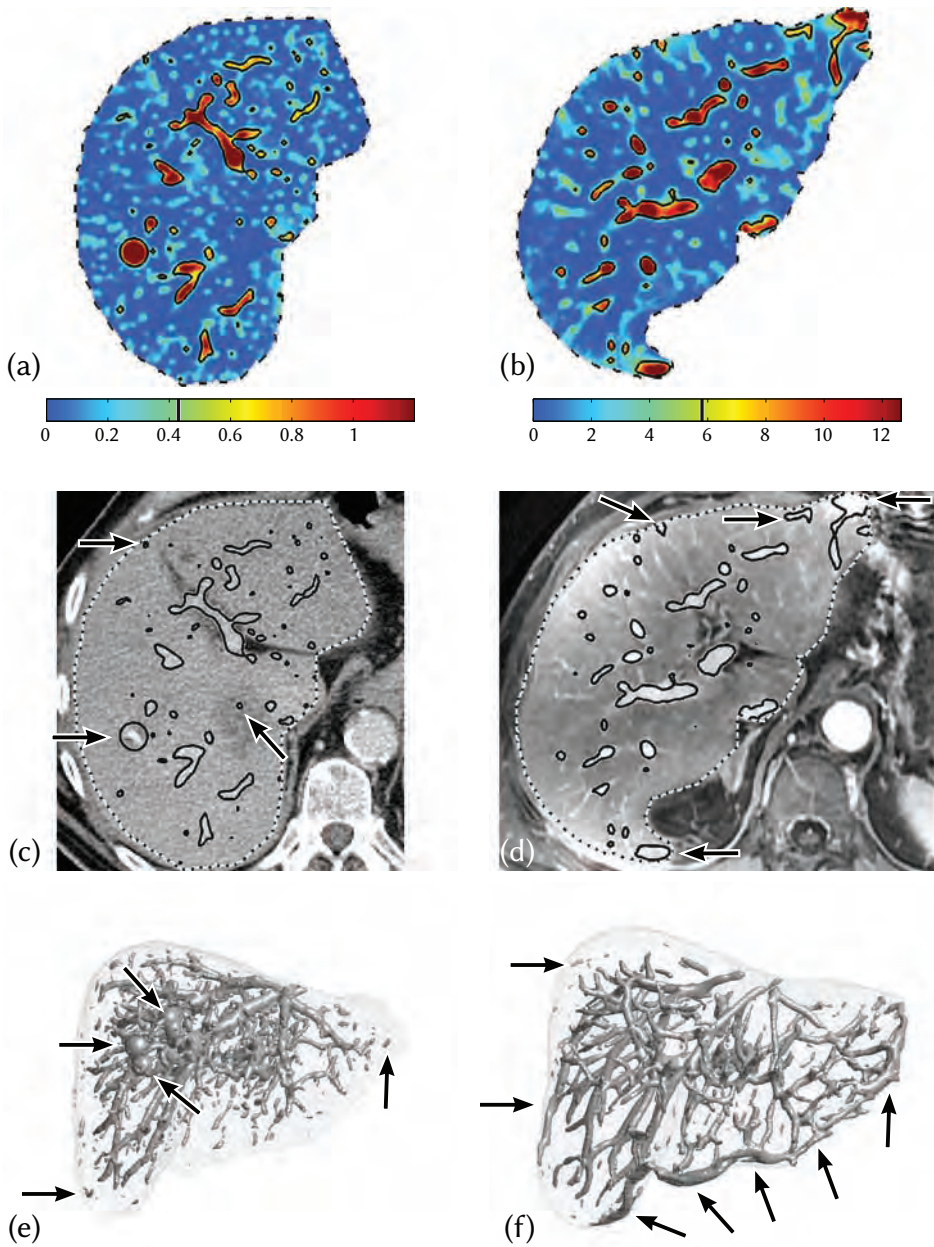


Figure 7.6: Vessel segmentation for CT (a,c,e) and MR (b,d,f) scans for patient 6. a-b) vesselness measure maps and 95 percentile contours. The 95 percentile value is indicated with a vertical line on the colorbar. c-d) input images and segmented vessels. e-f) 3D vessel surfaces using 95 percentile as threshold. Liver delineations are shown in dashed lines and wireframe. Arrows point out some false positives.

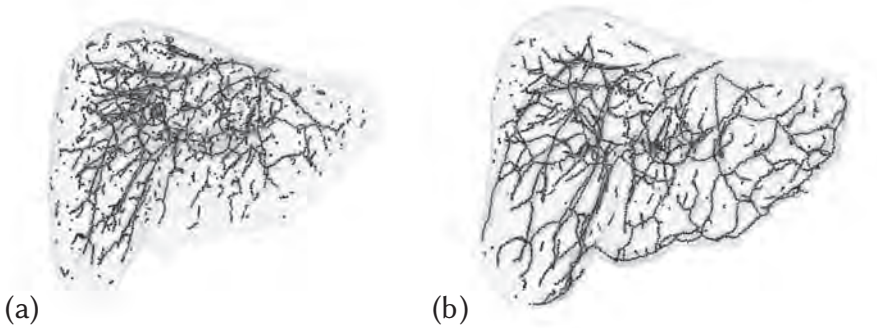


Figure 7.7: Midlines of the vessels shown in figure 7.6, (a) CT scan and (b) MR scan.

The registration procedure is performed in a deterministic annealing framework. Two cycles can be distinguished: the annealing cycle and the inner cycle. The annealing cycle controls the parameters used in the inner cycle, such as temperature and λ , and is commanded by the annealing rate, the initial and the final temperature. Each new iteration of the annealing cycle, allows the transformation to be more flexible (by reducing λ) and reduces the scope where points from the reference (or deforming) set can ‘search’ for corresponding points in the deforming (or reference) set (by reducing the temperature). The aim of the inner cycle is to allow the correspondence and transformation converge under a certain temperature. In practical terms, it estimates correspondences and updates the transformation for a given number of iterations. After several tests, we found empirical parameter values that worked optimally for the current application (initial temperature = 6, final temperature = 1, annealing rate = 0.7 and 10 iterations for the inner cycle).

Due to missing vessels in both scans and false positives, it is likely that a large number of points does not have a corresponding point in the other point set. These points, or outliers, were identified automatically by the method after the correspondence between points was calculated and were not included in the computation of the transformation. The correspondence is represented as a matrix m , where $m_{i,j}$ represents the correspondence between points i and j in the reference and deforming point sets, and two vectors for outliers. The points with very few corresponding points in the other set were identified as outliers, i.e. $\sum_j m_{i,j}$ for a point i or $\sum_i m_{i,j}$ for a point j was $< 10^{-6}$. These points were not used to update the non-rigid transformation. The temperature for calculating the outlier vector was kept high, as suggested by Chui and

Rangarajan [25].

Strategies

The multi-scale vesselness measure allows implementing a multi-level strategy for the vessel segmentation and registration (*strategy A*, figure 7.3(a)). At first only midlines of thick vessels, segmented using the largest σ , are registered. With each new iteration of the annealing cycle, thinner vessels are added to the registration by including smaller σ s in the vesselness measure map. In this way, aligning the thick vessels at first allows for general pose estimation, and incrementally, more detail is added to the registration. As an alternative, *strategy B* segments vessels of all diameters and registers all midlines at once (figure 7.3(b)). Notice that there is a clear distinction between vessel segmentation and non-rigid registration in strategy B, while the vessel segmentation is integrated within the non-rigid registration process for strategy A.

7.2.3. Validation

Measuring the residual distance after transformation of corresponding landmarks is often used as validation for non-rigid registration of the liver [11, 34, 135]. Common landmarks include vessel bifurcations identified by an expert. In our case, the bifurcations are implicitly included in the registration, since the midlines of the vessels are used in the registration. However, the bifurcation points are not actively aligned, since no one-to-one correspondence is enforced. Therefore, we regard the residual distances between vessel bifurcations as a transformation accuracy measure. For an independent anatomical validation, we identified additional anatomical landmarks within the liver tissue. They include cysts, markers and bifurcations of the biliary tree. The distances between these anatomical points and the vessel's midlines varied largely. For example, the bifurcations of the biliary tree are relatively close to the vessels surfaces, while cysts and markers were in arbitrary locations, occasionally in close proximity of vessels.

Identification of vessel bifurcations in CT and MR data is not straightforward. Many bifurcations are not clearly visible in an axial slice, since the orientation of a bifurcation may lie in any arbitrary plane. In order to maximize the number of vessel bifurcations used to validate the registration, bifurcations were automatically identified from the midlines previously segmented (see section 7.2.2), after which bifurcation pairs were manually selected and

their precise location manually refined. The bifurcations were automatically identified using a voting filter. All midline voxels that have more than two neighbors were marked as bifurcations. Notice that several marked voxels can belong to the same bifurcation. The marked voxels were then projected to the closest CT/MR scan slice. Then an observer selected pairs of bifurcations in the CT and MR scans and fine-tuned their locations. Notice that the location of the bifurcations was not limited to the marked voxels, and in many occasions, the observer deviated from the marked voxels to improve the agreement with the underlying anatomy. Ten to 15 vessel bifurcations and 4 to 6 additional anatomical landmarks were identified per patient. Additionally, the images resulting from applying non-rigid transformations were visually checked.

7.2.4. Rigid registration to estimate the extent of deformation

Livers in MR and CT scans were also aligned using a rigid registration, including rotations and translations. In the literature, intensity-based registration using mutual information of masked images is often referred to produce the best results for rigid registration between CT and MR scans for liver [73, 22]. In our study, the implementation in the MultiResMIRegistration of ITK² was used. The residual distances between the vessel bifurcation and additional anatomical landmarks after rigid transformation give an estimative of the extent of deformation present in the liver (breath-hold vs. abdominal compressed). These residual distances were compared to the non-rigid transformation results. Additionally, the images resulting from applying rigid transformations were visually checked.

We report the rotation angles of the rigid registration, which were found by decomposing the rotation matrix into primary rotations along three fixed Cartesian axes in the order AP, LR, CC in the right-handed coordinate system complying with the IEC standard (EN61217). For this purpose we implemented the algorithm described by Herter and Lott [51].

7.3. Results

Visual inspection of the results showed that the non-rigid transformations aligned the CT and MR images correctly for all patients, while moderate alignments were achieved by rigid registration. This can be clearly seen in figure 7.8. Notice that the rigid transformation is not able to align the

²<http://www.itk.org/ITK/applications/MutualInfo.html>

images/vessels properly (figures 7.8(a) and (b)). Conversely, the non-rigid transformation aligned correctly the images/vessels. Furthermore, it improved the global alignment of the liver contours, even though the liver surface was not included in the registration (figures 7.8(c) and (d)).

Figure 7.9 and table 7.1 show that for all patients, vessel-guided non-rigid registration improved notably the alignment of the CT and MR image sets compared to rigid registration. The extent of deformation of the liver was in the range of 2.8-10.7 mm, (figure 7.9, table 7.1). After non-rigid registration, the mean residual distances dropped to a range of 1.3-1.9 mm for the vessel bifurcations and 1.1-2.3 mm (*Strategy A*) for the additional anatomical landmarks. The large differences between the residual distances after rigid and non-rigid registration suggest that the liver suffers a considerable deformation, most likely caused by the abdominal compression used during the acquisition of the CT scan.

Table 7.1: Mean residual distance after transformation per registration type. Non-rigid A: Strategy A, from thick to thin vessels, Non-rigid B: Strategy B, all vessels at once. Rigid: ITK’s MultiResMIRegistration.

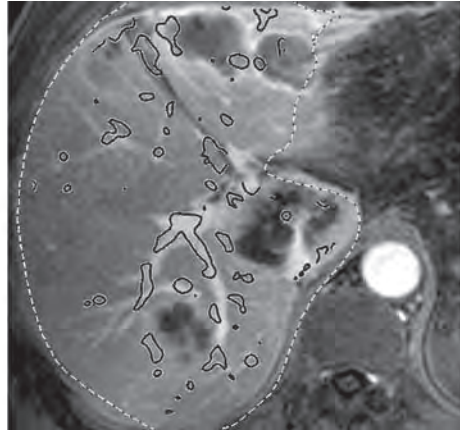
	Mean residual distance after transformation average (range) in mm		
	Rigid	Non-rigid A	Non-rigid B
Vessel bifurcations	5.4 (2.8, 10.2)	1.6 (1.3, 1.9)	1.7 (1.3, 1.9)
Additional landmarks	6.0 (3.5, 10.7)	1.5 (1.1, 2.3)	1.5 (1.1, 2.4)
All landmarks	5.5 (3.0, 10.3)	1.6 (1.3, 2.0)	1.6 (1.3, 2.0)

The differences in the residual distances between strategies A and B were small (less than 1 mm) and not significant. A substantial difference, however, was observed in the execution time. Strategy A was more than two times faster than strategy B (rates between execution times ranged between 2.0 and 3.0). The execution time varied widely among patients, and it was 22-74 minutes for strategy A and 51-218 minutes for strategy B. The execution time was related to the liver volume (figure 7.10).

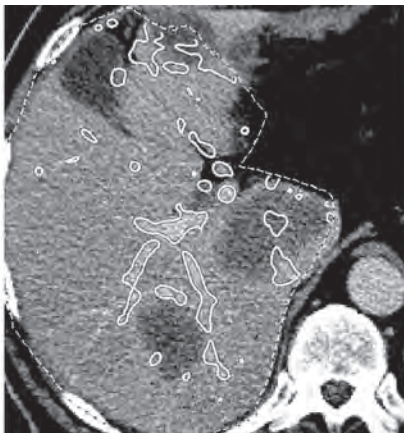
During the non-rigid registration, points that had a very low correspondence with points in the other point set were identified as outliers and were not considered in the computation of the transformation function. The number of outliers identified during the last iteration varied between 25 and 55%. Even though the number of outliers was large, the non-rigid registration produced



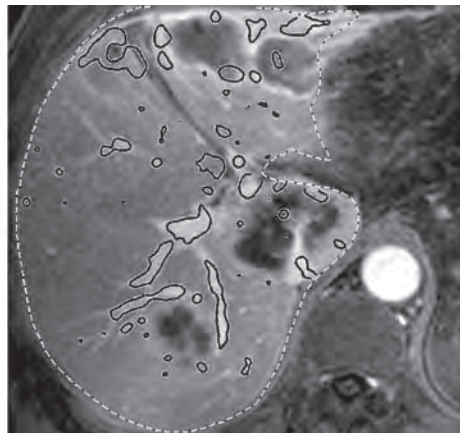
(a) CT scan and MR vessels transformed rigidly.



(b) MR scan and CT vessels transformed rigidly.



(c) CT scan and MR vessels transformed non-rigidly.



(d) MR scan and CT vessels transformed non-rigidly.

Figure 7.8: Results for rigid and non-rigid registration for patient 3. (a,c) Selected CT scan and transformed MR vessels, as white lines, using (a) the rigid transformation and (c) the non-rigid registration. (b,d) Selected MR scan and transformed CT vessels, as black lines, using (b) the rigid transformation and (d) the non-rigid registration. Notice that, even though the liver surface (shown as dashed contours) was not included in the non-rigid registration, its global alignment improves.

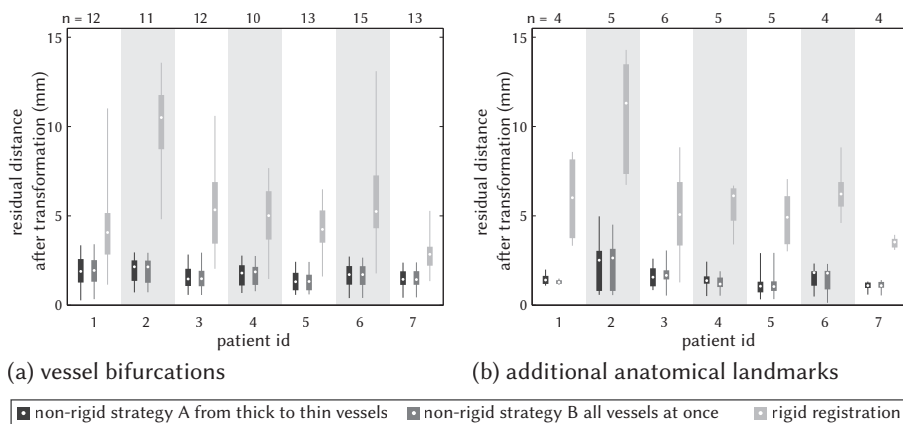


Figure 7.9: Residual distances after transformation for (a) vessel bifurcations and (b) additional anatomical landmarks. The dots represent the median, the boxes extend between the 25th-75th percentiles and the whiskers extend between minimum and maximum residual distance. For each patient, n is the number of analyzed bifurcations and landmarks.

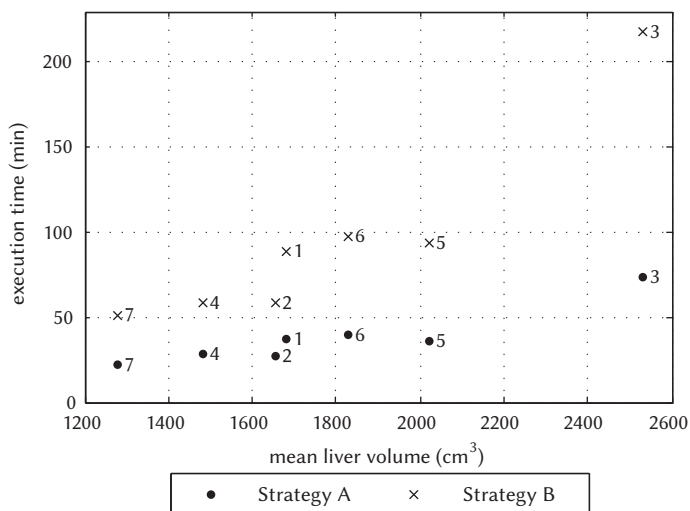


Figure 7.10: Execution time versus mean liver volume. The patient number is shown next to each data point.

very good alignments between the CT and the MR. This, in turn, demonstrated the robustness of the algorithm.

For the rigid registration, large rotations were found; average (range) - 3.9° (-11.2° to 4.3°), 1.6° (-3.8° to 9.0°) and -3.1° (-13.1° to 5.9°) in the AP, LR, CC directions respectively. These rotations may be caused by the applied abdominal compression applied during the acquisition of the CT scan.

7.4. Discussion

7.4.1. Non-rigid registration

We developed and validated a non-rigid registration method to align liver CT and MR scans, guided by vessels that are automatically segmented. Despite limitations in image quality and large difference in liver shapes, the image sets were registered successfully. Mean residual distance ranged between 1.1 and 2.4 mm for both non-rigid strategies. These values were considerably lower than those for rigid registration, demonstrating that non-rigid registration is better suitable to cope with large deformations such as deformations caused by abdominal compression.

Mean residual distance ranging between 1.1 and 2.4 mm are lower than the accuracy reported in most studies for MR/CT non-rigid registration for the liver. Table 7.2 summarizes some recent studies for multimodality non-rigid registration. Notice that due to the diversity of methods to measure accuracy, direct comparisons are not always possible. Furthermore, ours is the only study that registered CT images acquired under abdominal compression and breath-hold MR images. For Brock et al. [11], Voroney et al. [135], and presumably Elhawary et al. [34] and Archip et al. [2], less deformation is expected between the CT and MR scans since the scans were taken under more similar conditions. The studies that reported errors defined as residual distances of corresponding landmarks after transformation counted with a relatively low number of points (up to 7) in comparison to our study (10-15 vessel bifurcations and 4-6 additional anatomical landmarks). The only study that reported a lower error than our mean registration error is Archip et al. [2]. However, as mentioned before, no direct comparison is possible since different methods were used to measure accuracy: 95% Hausdorff distance between edges automatically extracted from images vs. residual distances between anatomical landmarks.

Table 7.2: Errors reported by recent studies for multimodality non-rigid registration for liver. Due to the diversity of methods to measure accuracy, direct comparisons are not always possible. All studies used contrast-enhanced CT, except for Elhawary et al. [34] and Archip et al. [2]. Abbreviations: Ref.: reference. N.pat.: number of patients. 10v: 10 volunteers.

Ref.	Error (mm)	N. pat.	Error definition and notes.
CT - MR registrations			
Current study	1.6	7	Mean residual distance between 10 to 15 vessel bifurcations and 4 - 6 additional anatomical landmarks.
Brock et al. [11]	(3.9 - 6.5)	1	Residual distances between 7 vessel bifurcations. 3 different methods.
Elhawary et al. [34]	4.1	9	Target registration error defined as distances between 3 correspondent points. B-splines based method.
Archip et al. [2]	1.6	13	95% Hausdorff distance between edges extracted from images. Finite-element method.
Voroney et al. [135]	4.2	17	Residual distances between 5 anatomical landmarks. Finite-element model-based method.
3D Ultrasound - CT registrations			
Lee et al. [76]	2.4	10v + 5	Fiducial registration error defined as mean-square of distance between 4 to 6 vessel bifurcations. B-spline free-form deformation.
Lange et al. [72]	(2.6 - 4.9)	3	Residual distances between corresponding points in dense vessel mid-lines. Image gradient and corresponding anatomical landmarks.

Non-rigid registration strategies

We expected *strategy A* to behave more robustly than *strategy B*, since *strategy A* starts the registration at a coarse level (only thick vessels) and refines

the transformation after each annealing iteration. However, the two non-rigid registration strategies yielded very similar results (less than 1mm difference between residual distances). Based on these results, both strategies could be used indistinctly.

We found large differences in execution time between the strategies: Strategy A was more than 2 times faster than strategy B. Execution time is determined by image resampling, vessel segmentation and non-rigid registration. The vessel segmentation includes the vesselness measure maps calculation, applying the 95 percentile threshold and thinning. The non-rigid registration includes the inner cycle and annealing cycle. The execution time for image resampling and vessel segmentation is proportional to the number of voxels in the input images, while the execution time for the registration increases cubically with the number of points to be registered (complexity order $O(n^3)$). For strategy A (from thick to thin vessels), the vessels are segmented once every iteration of the annealing cycle. Every iteration includes vessels with smaller diameters, therefore the number of points to register increases. Taking into account the cubic execution time of the registration, it is easy to realize that the first iteration takes considerably less time than the last one. For strategy B (all vessels at once), vessels are segmented only once and then registered. Consequently, the execution time of each annealing iteration is constant (same number of points). However, notice that the vessels segmented for the strategy B corresponds to the vessels segmented for the last iteration of strategy A, therefore the execution time of each iteration for strategy B corresponds to the slowest iteration for strategy A. Notice, that the execution time can be reduced considerably after code integration and optimization, since, as mentioned before in section 7.2.2, the current implementation relies heavily on file interfaces between Matlab and applications based on ITK.

Non-rigid registration robustness

For the current application, a large number of outliers was identified in both sets, between 25 and 55% during the last iteration. The outliers were successfully managed by encouraging points to be outliers (using a high temperature to calculate the outlier correspondence vector) and by not including the identified outliers in the transformation update. We found that this approach to manage outliers was sufficient, and we did not feel the need to implement a different outlier management such as proposed by [143].

Similar methods

To our knowledge, no method similar to *strategy A* (from thick to thin vessels) has been published in the past. Hu et al. [55] published a method which shares similarities with *strategy B*. However, MR data of only one volunteer was used to evaluate their method. To obtain two different anatomies, the MR image was transformed mimicking deformation due to respiratory motion. Errors of 2.6 mm were reported, which were calculated as the root mean square differences between points transformed by the a-priori known transformation and the resulting transformation.

Vessels were also used in registrations in other studies. Lee et al. [76] registered 3D ultrasound and contrast-enhanced CT in two sequential steps: first the vessels within the liver were registered, and last, the liver surfaces were aligned. The method minimized a similarity measure based on intensity values and gradients per voxel. Lange et al. [72] used image gradients and corresponding landmarks. The corresponding landmarks were used to initialize a TPS transformation, which was then refined using the image gradients. However, the gain of using non-rigid registration in the three cases that were studied was not clear, and even the non-rigid registration did not improve the rigid alignment in one of the cases. In an older study from the same group, [73], the improvement gained by the non-rigid registration was also low, and Lange et al. concluded that masked rigid registration was sufficient for liver surgery in many cases.

Limitations

The proposed method is based on segmenting and registering vessels in the liver. The segmentation based on vesselness can be a limitation of the method. For cases with extreme artefacts caused by markers, the segmentation of the vessels could be sub-optimal. Due to the strong contrast of the marker artefacts, the vesselness measure of the marker artefacts can overshadow that of the real vessels, since the segmentation is based on the 95 percentile. Also, when the contrast-to-noise ratio of the images is too low, large parts of the vessel tree can be lost, especially those areas where only small vessels are present.

Quantitative validation of non-rigid registration is difficult to implement since no ground truth is available when using real patient data. Some studies [22, 55] validate their methods using an a-priori known transformation. Unfortunately, in clinical practice, such transformation is unknown. Another possibility is to use phantoms where the deformation can be controlled

and the transformation can be known beforehand. The disadvantage of such an approach is that the deformation of the phantom may have little resemblance with the deformation in real patients. A common approach used by many groups (see section 7.4.1) is to report the residual distances after transformation of anatomical landmarks. Here, it is important to distinguish between registration accuracy and independent validation. In our study, the registration accuracy was assessed by vessel bifurcations, and the independent validation was performed using additional anatomical landmarks in the liver. Identification of vessel bifurcations is not straightforward. To maximize the number of vessel bifurcation, the bifurcations were detected automatically based on the segmented midlines, the bifurcation pairs were selected manually and their location fine-tuned. Although the process was done with care, the manual processing can be a source of error. Furthermore, since the identification of bifurcations and landmarks was limited to the axial slices of the CT and MR scans, the position established in the CC direction could be of lower accuracy.

7.4.2. Future work

In the current application bright vessels are identified and segmented. However, the vesselness measure can also be used to identify dark vessels on a bright background. Therefore, the method can be used to register other image modalities, such as 3D ultrasound, other MR sequences and images without contrast enhancement. Blood vessels and other tubular structures, such as ducts, can be found anywhere in the body. Consequently, when these vessels or tubular structures are visible, our segmentation-registration method could be used to register other areas, such as brain and lung. Moreover, the vesselness measure has been generalized to recognize other shapes as well, such as plates and blobs [112, 1].

In the current study, liver contours were used to define the region of interest. These contours were manually delineated, and although coarse, it required user interaction. In future applications, the liver contour could be autosegmented [92, 118]. Alternatively, smaller regions of interest, for example a small box around the tumor, can be selected and registered.

7.5. Conclusion

An accurate CT/MR vessel-guided non-rigid registration method for largely deformed livers was developed. Thinned blood vessels that were used as input

for the non-rigid registration, were segmented automatically in the CT and MR image sets. Validation was performed for cases with large differences in MR and CT liver shapes, related to application of abdominal compression during acquisition of CT scans. For seven patients, residual distances for well-defined landmarks were on average 1.6 mm, ranging from 1.3 to 2.0 mm. The method successfully handled falsely identified vessels and non-matching vessel structures. Alignment of MR images to abdominal-compressed CT images can be used to delineate the tumor in CT/MR images for stereotactic-body radiotherapy of the liver.



Chapter 8

Discussion

This thesis describes important improvements of a feature-based non-rigid registration method which were essential for its application in radiotherapy. In addition, this thesis describes the investigation related to three applications of the method. The method, thin-plate splines robust point matching (TPS-RPM) which was originally proposed by Chui and Rangarajan [25] (see chapter 2), is point-based, meaning that the structures to be registered are represented by two sets of points: the reference and the deforming point sets. The method iteratively estimates point correspondence between the two sets, and updates a non-rigid transformation modeled by a thin-plate spline.

One of the most interesting aspects of this PhD research is that in parallel to the method improvements, practical applications were investigated, of which some are nowadays applied clinically to improve the treatment of patients. The work related to three applications is described in chapters 5, 6 and 7. An application which is not included in this thesis is the analysis of residual geometric uncertainties of the prostate and seminal vesicles after online corrections with implanted markers using non-rigid registration. The obtained geometrical uncertainties were used to determine accurate safety margins for the treatment of prostate and the flexible seminal vesicles [129]. Another application not described in this thesis is the pre-treatment modeling of the large deformation of the cervix-uterus. Currently, motion models established before the treatment, are applied in a plan-of-the-day online adaptive strategy that reduces dose to healthy tissue [8, 6, 9].

In the following sections, the characteristics and improvements of the method are discussed. In section 8.2, the three applications in radiotherapy investigated in this thesis are addressed. The discussion ends with the current limitations of this method and alternative approaches, which is followed by an outline of future work to further improve the method and the conclusions.

8.1. Method characteristics and improvements

8.1.1. Inclusion of a priori information for registration of multiple structures

In the original point matching method, the correspondence cannot be restricted such that correspondence between point subsets can be excluded or forced. For example, if multiple organs are matched simultaneously and the organs are adjacent to each other, then points of organ A might be aligned to points belonging to organ B, resulting in unrealistic transformations. For applications in radiotherapy, it is often the case that organs of interest lie in

close proximity of each other and their location is inter-related, which is the case for the uterus-cervix and the bladder, and for the interlocking chewing muscles (chapters 3 and 6).

The a priori information is introduced in the registration method by applying a label to each point. The label identifies the organ or structure that the point belongs to. During the correspondence estimation, only correspondences of points with the same labels are kept, and those of mismatching labels are eliminated (see chapter 3). As a result, the transformation can be kept global, smooth and continuous while local details of each individual organ or structure are aligned. Besides using labels to identify to which organ a point belongs to, they can also be used to classify points. It allows different types of features to be registered simultaneously. For example, single points and lines representing unmistakable anatomical landmarks (see chapter 3), or points representing vessel midlines, bifurcations, and surfaces.

8.1.2. Inverse consistency

Consistency in the results of non-rigid registration is a pre-requisite for clinical applications; that is the registration from the reference set to the deforming set should be close to the inverse of the back-transformation. Assuring that deformations identified by non-rigid registration are independent of the registration direction is a challenge that not always can be met. The method presented in this thesis enforces consistency by calculating transformations for both directions simultaneously, based on a common correspondence matrix, (chapter 4). By enforcing consistency, the inverse consistency error reduced to around 1 mm even for extreme deformations for the points on the surface of the organs. The symmetric registration consistently aligned organs with large scale deformations, such as the uterus-cervix and the bladder. Inverse consistency, however, does not guarantee that the obtained back-transformation is equal to the inverse of the forward-transformation [48, 47]. Away from the organ's surface the inverse consistency is not assured. To overcome this limitation, alternative transformation functions can be used from which the inverse can be calculated directly (see section 8.5).

8.1.3. Outlier handling

In point-based non-rigid registration, outliers are points that are present in one of the point sets with no counterpart in the other point set. For example, vessel segmentation in MR scans may result in a more detailed vessel tree

than vessel trees segmented from a CT scan. Also, falsely identified vessels in one of the image sets increase the level of dissimilarity (see chapter 7). If handled improperly, these outliers may misguide the registration and produce low quality transformations. The registration method presented in this thesis is capable of identifying outliers, which are then excluded from the estimation of the transformation. Even though a relatively high percentage of outliers in the point sets were present in the registration of segmented vessels (25 to 55%), the resulting transformations aligned the underlying anatomy successfully, as was demonstrated by the low residual errors (≤ 2.0 mm) in chapter 7. It has been argued that the original method is limited when dealing with outliers in both point sets simultaneously [143]. However, the accuracy of the resulting transformation is adequate to be used in clinical applications. Currently, new heuristics are being tested to further improve outlier handling.

8.1.4. Correspondence estimation

One of the strongest points of TPS-RPM, is that it estimates the correspondence between the point sets automatically as part of the registration procedure, and furthermore, the number of points in the input sets can be different. Many feature-based methods for non-rigid registration rely on landmarks, and a fixed correspondence that should be established before the registration starts [13, 113, 63]. Often these landmarks require manual identification, which can be a labor-intensive and error-prone. Note that a wrong correspondence will result in an erroneous transformation. Few methods solve the correspondence problem automatically [84, 100]. Liang and Yan [84] adjust dynamically the locations of the corresponding points by minimizing a strain energy function obtained from a finite element simulation. This method is limited to an equal number of points in both sets and it is computationally expensive, since every iteration requires a complete solution of the finite element analysis. The method proposed by Myronenko and Song [100] is discussed in section 8.4.

8.1.5. Point density

In order to register structures correctly, a sufficient amount of detail should be included in the point sets. The level of detail included in the registration is controlled by the density of the points representing the input structures. The method presented in this thesis includes a procedure to generate points on the surfaces of organs (see chapter 3 and 4). The point density should be enough to capture all the details that are relevant in the registration for both sets.

However, experimental results indicated that using approximately the same number of points for organs that underwent large-scale deformations, such as the bladder, may improve results and accelerate the registration (chapter 4). Note, that in this situation the point density is substantially different between the deforming and reference set, since the volume of the bladder can increase by up to 11-fold.

8.2. Applications in radiotherapy

The improvements of the registration method described in thesis made possible the use of this point-based non-rigid registration method in radiotherapy. In chapters 5, 6 and 7, three applications within radiotherapy were investigated, i.e. a 3D analysis of local anatomy changes in the head and neck region, dose addition taking into account deformations, and the non-rigid alignment of largely deformed livers. In particular, the latter two applications have a direct positive impact on the treatment of the patient. Each application is briefly discussed in the following paragraphs.

Chapter 5 describes the application of the non-rigid registration method to track the anatomical changes of salivary glands and the tumor in patients with head and neck cancer. The results that were found for the salivary glands were consistent with results reported by other groups [4, 49, 108, 75]. The advantage of using non-rigid registration to track anatomical changes, is that detailed 3D information was obtained. For example, it was shown that during the course of treatment, the parotid glands shrank towards the target area where the lethal tumor dose was delivered. As a consequence, the actual dose received by the glands was higher than expected based on the planning CT scan. The increase in dose might result in more treatment-related side effects, and even, in complete malfunction of the organ. The radiation treatment of these kind of tumors may be improved by including population statistics of organ deformations in probabilistic treatment planning [45]. In chapter 5, only two time points, i.e. at planning and after 23 treatment fractions were available for analysis. Therefore, possibly not all anatomical changes were captured. Further research using images acquired at various time points is recommended.

Chapter 6 describes the use of the non-rigid registration to take into account anatomical changes for adding dose distributions of two treatment modalities: external beam radiotherapy and brachytherapy. The dose was added for organs at risk of five oropharyngeal patients, including biological effects to account for fractionation differences. The method was robust against perturbations

in the input parameters and against moderate errors in the delineations of the organs of interest. Correspondence filtering allowed the inclusion of anatomical landmarks. Therefore if subunit information of an organ would be available, it could be included in the registration as well. Being able to calculate the total dose expected to be delivered to a patient opens the possibility for a simultaneous optimization of the combined treatments. Also, treatment-related toxicity and dose-volume-effect relationships of combined treatments can be determined more accurately. The method can be improved in areas where extremely steep dose gradients are present, which is often the case in brachytherapy. Additionally, establishing the correct α/β ratio is important.

Chapter 7 describes the application of the non-rigid registration method to align largely deformed livers in CT and MR scans, guided by automatically segmented vessels. This study was motivated by the fact that tumors in the liver are often better visible in MR images [95] compared to CT scans. However, CT images are used to design the treatment plan. The high variability in image quality was an important challenge in this study. Simple segmentation methods, such as thresholding or region growing algorithms, were not suitable for segmenting the vessels in the image. Therefore, a vesselness measure [111] was applied to segment vessels automatically. Due to the difference in vessel contrast between CT and MR image sets and false positives in the vesselness measure, a large number of outliers was generated (25% - 55%). The method was able to identify and handle these outliers correctly (see section 8.1.3). Residual errors between unmistakable anatomical reference points after transformation were low (≤ 2.0 mm). Drawbacks of the current implementation are the computational time and the manual contouring of the liver outline. The latter can be avoided by using a rectangular shaped region-of-interest.

8.3. Method limitations

The objective of this thesis was to improve a non-rigid registration method in order to make it suitable for its use in the field of radiotherapy and to investigate practical applications. The performance in terms of computational time was not an objective. As pointed out in the discussion sections of chapters 3, 6 and 7, the method is currently not suitable to be used for online applications for which registrations should be calculated within a few seconds. However, there is room for code optimization and integration. Currently, the method is being ported to a software development platform (Matterhorn) developed at the radiation oncology department of Erasmus MC. As part of the integration, the

code is being rewritten in C++, revised and optimized.

The non-rigid registration method is point-based. The structures to be aligned are represented by points. These structures can be manually delineated, as in chapters 3, 4, 5 and 6, or automatically segmented as in chapters 6 (uterus mid-line) and 7 (vessels in the liver). The manual segmentation or contouring of organs of interest, is currently a required step in the radiotherapy workflow. However, it is time consuming and is affected by inter-observer and intra-observer variability. That is, the same organ can be delineated differently by different persons, and even, the same person can delineate the same organ differently every time. In chapter 6, the impact of differences in contouring on dose addition was studied by simulating delineation errors.

Quantitative anatomical validation of non-rigid registration is still a challenge, since the ground truth is often not available. Some studies validate their methods using a-priori known transformations [22, 55, 149]. Unfortunately, in clinical practice, such transformations are unknown. Another possibility is to use phantoms where the deformation can be controlled and the transformation can be known beforehand. The disadvantage of such an approach is that the deformation of the phantom may have little resemblance with the deformation in real patients. A common approach used by many groups [13, 135, 63, 11] is to report the residual distances after the transformation of anatomical landmarks. This approach was also used to validate the resulting transformations in chapters 3, 4 and 7. In chapter 6, a robustness analysis was presented as an alternative to validation against ground truth.

The correspondence between points is mainly driven by the distance between points and the temperature variable (see 2). Furthermore, the transformation function used to align the data is based in a simple physical model: the bending of a thin sheet of metal under certain local constraints. Biomechanical properties cannot be included in the registration method. The only parameter that is available to fine-tune the registration is the stiffness parameter λ . However, there is no direct link between λ and any biomechanical property.

The transformation resulting from the registration is controlled by the input points. However, other locations in the patient that are not represented by the point sets can be transformed as well, such as the interior of the organs for dose addition or image mapping. In order to warp these locations, the interpolation provided by the transformation function is used. Even though the anatomical validation has shown good results for the applications investigated in this thesis, it is not possible to assure that the results based on surface

matching, can always be accurately applied to locations other than the surface or landmark points.

8.4. Similar non-rigid registration methods

The original TPS-RPM algorithm [25, 23] shares several similarities with methods proposed by Myronenko and Song [100] and Jian and Vemuri [59]. These algorithms are point-based, and iteratively improve the alignment between the reference and deforming point sets. The main difference between these methods and TPS-RPM is that TPS-RPM follows an optimizational approach, while Myronenko and Song [100] and Jian and Vemuri [59] follow a probabilistic approach. Myronenko and Song [100] consider point matching as a probability density estimation in which the likelihood between data (one of the point sets) and Gaussian mixture model centroids (the secondary point set) is maximized. This approach is commonly used in object recognition for template matching. The correspondence is implicitly modeled as a membership probability of the data (the points in one point set) to clusters defined by the centroids (points in the secondary point set). The resulting non-rigid transformation is a linear combination of Green's function centered on each Gaussian centroid. Jian and Vemuri [59] models each point set as a mixture of Gaussians. In this approach, point correspondence is not established, but the Gaussian mixtures are aligned by minimizing the L_2 distance between the Gaussian distributions. It is assumed that the mixtures are statistically similar to each other when the points are properly aligned. The method also models the transformation as a thin-plate spline. In terms of execution time, the method from Jian and Vemuri [59], reported that registering more than 300 points in both sets becomes computationally expensive, but no specific values were given. A fast numerical scheme such as the fast Gauss Transform applied by Myronenko and Song [100] can be used to speed up the registration. In addition, Myronenko and Song [100] used a low-rank matrix approximation to speed up the solution of the linear system of equations for the non-rigid transformation. Registration times of less than 2 seconds for 453 points and 10 minutes for more than 35000 points were reported.

Many feature-based registration methods used in radiotherapy are based on finite element analysis (FEA, [15, 13, 84]). FEA is often used in structural analysis to calculate the effects of applying certain forces on the boundaries of objects of a given material. In order to apply FEA to track anatomical changes in radiotherapy, surface meshes representing the organs of interest are generated

from the reference and deforming images. A volumetric mesh of the organ in the reference image is created using small elements (often cubes or tetrahedra). The elements are assigned a material, characterized by its properties (Poisson's ratio and Young's modulus). Then, several corresponding points on the boundaries of the organs are identified, for example based on the curvature of the organ's surface [13]. Next, the displacements of these corresponding points are converted to forces, which can be applied to the boundaries of the volumetric mesh. Finally, the deformation of the organ is computed using FEA. As a result, the deformed organ resulting from the FEA calculation, resembles the organ in the 'deforming' image. Errors, defined as residual distances of anatomical landmarks inside the organs after registration, are reported to range 1.7 and 2.8 for the different directions for lung and liver deformations [13]. An important factor that influences the quality of the registration is the choice of material properties [19]. Given 30% in material uncertainty, the registration error can reach 1.3 mm for hollow organs and 4.5 mm for solid organs. Since FEA-based methods are computational intensive, the time requirements needed for clinical applications may limit their applicability [15]. Although the current implementation of the method described in this thesis results in large computational times, it is expected that lower execution times can be achieved by further optimization (see section 8.5). Another advantage with respect to FEA-based methods, is that the inclusion of unstructured points (e.g. loose points in the space representing anatomical landmarks) in the registration does not require any modification or complex modeling (see chapter 3).

8.5. Future work

The method described in this thesis has been successfully applied in a number of applications in the field of radiotherapy. However, there is still room for improvement. As mentioned before in section 8.3, execution time can be improved by optimization and integration of the code. Additionally, low-rank matrix approximation to solve the linear system of equations for the non-rigid transformation can be used to speed-up the registration, as was applied by Myronenko and Song [100]. Besides code optimization, new heuristics for handling outliers are currently under investigation (section 8.1.3). Also, complementary heuristics for correspondence estimation can be interesting for improving the registration. For example, connectivity information could be used to reinforce correspondence between neighbors in the point sets. Connectivity information can be derived from the surface mesh that represents

the organ. The mesh is composed by elements, usually triangles, that connect points in space. Connectivity information can easily be used to identify the neighbors of a given point, which then can be used in the correspondence estimation.

Currently, a single λ value to regulate the transformation function is used. A large λ value restricts the transformation to be mostly affine, while a low λ value allows a more non-rigid transformation. However, if multiple organs with different properties are registered simultaneously, a single λ value could be inadequate to capture the nature of the deformation of each organ. For example, if a bladder and a prostate are being registered simultaneously, the bladder would require a more flexible λ value, while for the prostate a more conservative λ would suffice. Another example, for which more than one λ value could improve the performance of the method, is the registration of the bladder with a tumor in the bladder wall. Here, the tumor locally changes the mechanical properties of the bladder wall. Currently, the inclusion of multiple λ values is being investigated.

Up to this point, only points that distribute pseudo-homogeneously on the surfaces or in the vessels midlines have been used. In this way, all regions of the surfaces or vessels are equally represented in the non-rigid registration. Adaptive point generation [69, 62] is a method by which critical areas that need a more detailed representation can be described with denser point clouds than areas that are less critical for the registration. In this way, the total number of points might be reduced, and thus the computational time, without loss in registration accuracy.

Other improvements could be achieved by using a different transformation function to align the point sets. The method described in this thesis uses thin plate splines. However, the robust point matching framework, from which the TPS-RPM originates, was designed in such a way that other transformation types, other than thin plate splines, can be used (see chapter 2). A promising alternative would be using diffeomorphisms [61, 14, 48]. A diffeomorphism is a map between two topological spaces, which is differentiable and has a differentiable inverse. In other words, a diffeomorphism would allow aligning image data, while assuring smooth and consistent transformations. In theory, the organs can be registered in one direction, e.g. deforming to reference. The transformation for the other direction, or back-transformation, can be calculated from the inverse of the transformation, which always exists. Note, however, that there is no guarantee that if you start the registration in the opposite direction, the resulting transformation and backtransformation are the

same as if you start the registration in the original direction.

Automatic segmentation [79], as was demonstrated in chapter 7, may open new application possibilities of the method. In chapter 7, a vesselness measure was used to segment vessels automatically. The measure has been generalized to recognize other shapes, such as plates and blobs [112, 1]. Automatic feature segmentation could overcome an important limitation of the current method, which is the manual contouring of structures. Alternatively, the use of atlas-based auto-segmentation [79], could also be used to generate input structures for the non-rigid registration method developed in this PhD thesis.

8.6. Conclusions

The feature-based non-rigid registration method presented in this thesis registers single or multiple organs in an accurate, consistent, and anatomically coherent way. Furthermore, the method is currently used for clinical applications. Currently, code optimization and integration is extending the method applicability by reducing its execution time. The method is a useful tool that is supporting new developments in high-precision image-guided adaptive radiotherapy.

Bibliography

- [1] L. Antiga. Generalizing vesselness with respect to dimensionality and shape. *The Insight Journal* [<http://insight-journal.org>], 08 2007.
- [2] N. Archip, S. Tatli, P. Morrison, F. Jolesz, S. K. Warfield, and S. Silverman. Non-rigid registration of pre-procedural mr images with intra-procedural unenhanced ct images for improved targeting of tumors during liver radiofrequency ablations. *Int Conf Med Image Comput Comput Assist Interv*, 10(Pt 2):969–977, 2007.
- [3] C. Ares, Y. Popowski, S. Pampallona, P. Nouet, G. Dipasquale, S. Bieri, O. Ozsoy, M. Rouzaud, H. Khan, and R. Miralbell. Hypofractionated boost with high-dose-rate brachytherapy and open magnetic resonance imaging-guided implants for locally aggressive prostate cancer: A sequential dose-escalation pilot study. *Int J Radiat Oncol Biol Phys*, 75(3):656–663, Nov 2009.
- [4] J. L. Barker, A. S. Garden, K. K. Ang, J. C. O’Daniel, H. Wang, L. E. Court, W. H. Morrison, D. I. Rosenthal, K. S. Chao, S. L. Tucker, R. Mohan, and L. Dong. Quantification of volumetric and geometric changes occurring during fractionated radiotherapy for head-and-neck cancer using an integrated ct/linear accelerator system. *Int J Radiat Oncol Biol Phys*, 59(4):960–970, 2004.
- [5] J. Boda-Heggemann, C. Walter, A. Rahn, H. Wertz, I. Loeb, F. Lohr, and F. Wenz. Repositioning accuracy of two different mask systems-3d

revisited: comparison using true 3d/3d matching with cone-beam ct. *Int J Radiat Oncol Biol Phys*, 66(5):1568–1575, Dec 2006.

- [6] L. Bondar, M. Hoogeman, J. W. Mens, G. Dhawtal, I. de Pree, R. Ahmad, S. Quint, and B. Heijmen. Toward an individualized target motion management for imrt of cervical cancer based on model-predicted cervix–uterus shape and position. *Radiotherapy and Oncology*, 99(2):240–245, 2011.
- [7] L. Bondar, M. S. Hoogeman, E. M. Vásquez Osorio, and B. J. M. Heijmen. A symmetric nonrigid registration method to handle large organ deformations in cervical cancer patients. *Med Phys.*, 37(7):3760–3772, 2010.
- [8] M. Bondar, M. Hoogeman, G. Dhawtal, J. Mens, E. Vasquez Osorio, I. de Pree, S. Quint, R. Ahmad, and B. Heijmen. Tu-d-brc-06: Towards online image guided radiotherapy for cervical cancer: Accurate cervix-uterus prediction based on measured bladder volumes. *AAPM*, 36(6):2735–2735, 2009.
- [9] M. Bondar, M. Hoogeman, J. Mens, S. Quint, R. Ahmad, G. Dhawtal, and B. Heijmen. Individualized nonadaptive and online-adaptive imrt treatment strategies for cervical cancer patients based on pre-treatment acquired variable bladder filling ct-scans. *International Journal of Radiation Oncology*Biological*Physics*, In press:–, 2011.
- [10] F. L. Bookstein. Principal warps: thin-plate splines and the decomposition of deformations. *IEEE Transactions on Pattern Analysis and Machine Intelligence*, 11(6):567–585, 1989.
- [11] K. K. Brock and Deformable Registration Accuracy Consortium. Results of a multi-institution deformable registration accuracy study (midras). *Int J Radiat Oncol Biol Phys*, 76(2):583–596, 2010.
- [12] K. K. Brock, D. L. McShan, R. K. Ten Haken, S. J. Hollister, L. A. Dawson, and J. M. Balter. Inclusion of organ deformation in dose calculations. *Med Phys*, 30(3):290–295, Mar 2003.
- [13] K. K. Brock, M. B. Sharpe, L. A. Dawson, S. M. Kim, and D. A. Jaffray. Accuracy of finite element model-based multi-organ deformable image registration. *Med Phys*, 32(6):1647–1659, 2005.

-
- [14] V. Camion and L. Younes. Geodesic interpolating splines. In *Proceedings of the Third International Workshop on Energy Minimization Methods in Computer Vision and Pattern Recognition*, EMMCVPR '01, pages 513–527, London, UK, 2001. Springer-Verlag.
- [15] X. Chai, M. van Herk, J. B. van de Kamer, M. C. C. M. Hulshof, P. Remeijer, H. T. Lotz, and A. Bel. Finite element based bladder modeling for image-guided radiotherapy of bladder cancer. *Medical Physics*, 38(1):142–150, 2011.
- [16] K. S. Chao, S. Bhide, H. Chen, J. Asper, S. Bush, G. Franklin, V. Kavadi, V. Liengswangwong, W. Gordon, A. Raben, J. Strasser, C. Koprowski, S. Frank, G. Chronowski, A. Ahamad, R. Malyapa, L. Zhang, and L. Dong. Reduce in variation and improve efficiency of target volume delineation by a computer-assisted system using a deformable image registration approach. *Int J Radiat Oncol Biol Phys*, 68(5):1512–1521, Aug 2007.
- [17] K. S. Chao, D. A. Low, C. A. Perez, and J. A. Purdy. Intensity-modulated radiation therapy in head and neck cancers: The mallinckrodt experience. *Int J Cancer*, 90(2):92–103, Apr 2000.
- [18] K. S. Chao, G. Ozyigit, B. N. Tran, M. Cengiz, J. F. Dempsey, and D. A. Low. Patterns of failure in patients receiving definitive and postoperative imrt for head-and-neck cancer. *Int J Radiat Oncol Biol Phys*, 55(2):312–321, Feb 2003.
- [19] Y. Chi, J. Liang, and D. Yan. A material sensitivity study on the accuracy of deformable organ registration using linear biomechanical models. *Med Phys*, 33(2):421–433, 2006.
- [20] G. Christensen and H. Johnson. Consistent image registration. *IEEE Transactions on Medical Imaging*, 20(7):568 – 582, 2001.
- [21] G. E. Christensen, B. Carlson, K. S. Chao, P. Yin, P. W. Grigsby, K. Nguyen, J. F. Dempsey, F. A. Lerma, K. T. Bae, M. W. Vannier, and J. F. Williamson. Image-based dose planning of intracavitary brachytherapy: registration of serial-imaging studies using deformable anatomic templates. *Int J Radiat Oncol Biol Phys*, 51(1):227–243, 2001.
- [22] W. C. Christina Lee, M. E. Tublin, and B. E. Chapman. Registration of mr and ct images of the liver: comparison of voxel similarity and

-
- surface based registration algorithms. *Comput Methods Programs Biomed*, 78(2):101–114, 2005.
- [23] H. Chui. *Non-Rigid Point Matching: Algorithms, Extensions and Applications*. PhD thesis, Yale University, 2001.
- [24] H. Chui, J. Rambo, J. S. Duncan, R. Schultz, and A. Rangarajan. Registration of cortical anatomical structures via robust 3d point matching. In *Proceedings of the 16th International Conference on Information Processing in Medical Imaging*, IPMI '99, pages 168–181, London, UK, 1999. Springer-Verlag.
- [25] H. Chui and A. Rangarajan. A new point matching algorithm for non-rigid registration. *Computer Vision and Image Understanding*, 89:114–141, 2003.
- [26] H. Chui, A. Rangarajan, J. Zhang, and C. M. Leonard. Unsupervised learning of an atlas from unlabeled point-sets. *IEEE Transactions on Pattern Analysis and Machine Intelligence*, 26:160–172, 2004.
- [27] H. Chui, L. Win, R. Schultz, J. S. Duncan, and A. Rangarajan. A unified non-rigid feature registration method for brain mapping. *Med Image Anal*, 7(2):113–130, 2003.
- [28] W. R. Crum, T. Hartkens, and D. L. G. Hill. Non-rigid image registration: theory and practice. *Br J Radiol*, 77(supplement 2):S140–153, 2004.
- [29] L. A. Dawson, Y. Anzai, L. Marsh, M. K. Martel, A. Paulino, J. A. Ship, and A. Eisbruch. Patterns of local-regional recurrence following parotid-sparing conformal and segmental intensity-modulated radiotherapy for head and neck cancer. *Int J Radiat Oncol Biol Phys*, 46(5):1117–1126, Mar 2000.
- [30] W. J. de Kruijf, B. J. Heijmen, and P. C. Levendag. Quantification of trade-off between parotid gland sparing and planning target volume underdosages in clinically node-negative head-and-neck intensity-modulated radiotherapy. *Int J Radiat Oncol Biol Phys*, 68(1):136–143, May 2007.
- [31] R. Deriche. Recursively implementating the Gaussian and its derivatives. Research Report RR-1893, INRIA, 1993.

- [32] A. Eisbruch, J. A. Ship, H. M. Kim, and R. K. Ten Haken. Partial irradiation of the parotid gland. *Semin Radiat Oncol*, 11(3):234–239, Jul 2001.
- [33] A. Eisbruch, R. K. Ten Haken, H. M. Kim, L. H. Marsh, and J. A. Ship. Dose, volume, and function relationships in parotid salivary glands following conformal and intensity-modulated irradiation of head and neck cancer. *Int J Radiat Oncol Biol Phys*, 45(3):577–587, Oct 1999.
- [34] H. Elhawary, S. Oguro, K. Tuncali, P. R. Morrison, S. Tatli, P. B. Shyn, S. G. Silverman, and N. Hata. Multimodality non-rigid image-registration for planning, targeting and monitoring during ct-guided percutaneous liver tumor cryoablation. *Academic Radiology*, 17(11):1334 – 1344, 2010.
- [35] P. M. Evans. Anatomical imaging for radiotherapy. *Physics in Medicine and Biology*, 53(12):R151–R191, 2008.
- [36] J. Feng, H. H. S. Ip, L. Y. Lai, and A. Linney. Robust point correspondence matching and similarity measuring for 3d models by relative angle-context distributions. *Image Vision Comput.*, 26:761–775, June 2008.
- [37] M. Foskey, B. Davis, L. Goyal, S. Chang, E. Chaney, N. Strehl, S. Tomei, J. Rosenman, and S. Joshi. Large deformation three-dimensional image registration in image-guided radiation therapy. *Phys Med Biol*, 50(24):5869–5892, Dec 2005.
- [38] J. F. Fowler. Sensitivity analysis of parameters in linear-quadratic radiobiologic modeling. *Int J Radiat Oncol Biol Phys*, 73(5):1532–1537, Apr 2009.
- [39] A. F. Frangi, R. F. Frangi, W. J. Niessen, K. L. Vincken, and M. A. Viergever. Multiscale vessel enhancement filtering. In *MICCAI*, pages 130–137. Springer-Verlag, 1998.
- [40] N. Gagvani and D. Silver. Parameter-controlled volume thinning. *CVGIP: Graph. Models Image Process.*, 61:149–164, May 1999.
- [41] D. Geiger and F. Girosi. Parallel and deterministic algorithms from mrfs: surface reconstruction. *IEEE Transactions on Pattern Analysis and Machine Intelligence*, 13(5):401–412, 1991.
- [42] A. Godley, E. Ahunbay, C. Peng, and X. A. Li. Automated registration of large deformations for adaptive radiation therapy of prostate cancer. *Medical Physics*, 36(4):1433–1441, 2009.

-
- [43] S. Gold and A. Rangarajan. Softmax to softassign: neural network algorithms for combinatorial optimization. *J. Artif. Neural Netw.*, 2(4):381–399, August 1996.
- [44] S. Gold, A. Rangarajan, C.-P. Lu, S. Pappu, and E. Mjolsness. New algorithms for 2d and 3d point matching: pose estimation and correspondence. *Pattern Recognition*, 31(8):1019–1031, 1998.
- [45] J. Gordon and J. Siebers. 258 oral probabilistic planning reduces normal tissue complication probabilities in prostate imrt plans. *Radiotherapy and Oncology*, 99(Supplement 1):S101 – S102, 2011.
- [46] T. Guerrero, G. Zhang, T. C. Huang, and K. P. Lin. Intrathoracic tumour motion estimation from ct imaging using the 3d optical flow method. *Phys Med Biol*, 49(17):4147–4161, Sep 2004.
- [47] H. Guo and A. Rangarajan. Diffeomorphic point matching with applications in biomedical image registration. *International Journal of Tomography and Statistics*, 15(F10):42–57, 2010.
- [48] H. Guo, A. Rangarajan, S. C. Joshi, and L. Younes. Non-rigid registration of shapes via diffeomorphic point matching. In *IEEE International Symposium on Biomedical Imaging (ISBI)*, pages 924–927, 2004.
- [49] E. K. Hansen, M. K. Bucci, J. M. Quivey, V. Weinberg, and P. Xia. Repeat ct imaging and replanning during the course of imrt for head-and-neck cancer. *Int J Radiat Oncol Biol Phys*, 64(2):355–362, 2006.
- [50] J. M. Hensel, C. Ménard, P. W. Chung, M. F. Milosevic, A. Kirilova, J. L. Moseley, M. A. Haider, and K. K. Brock. Development of multiorgan finite element-based prostate deformation model enabling registration of endorectal coil magnetic resonance imaging for radiotherapy planning. *Int J Radiat Oncol Biol Phys*, 68(5):1522–1528, Aug 2007.
- [51] T. Herter and K. Lott. Algorithms for decomposing 3-d orthogonal matrices into primitive rotations. *Computers & Graphics*, 17(5):517 – 527, 1993.
- [52] T. Hofmann and J. M. Buhmann. Pairwise data clustering by deterministic annealing. *IEEE Transactions on Pattern Analysis and Machine Intelligence*, 19(1):1–14, 1997.

-
- [53] H. Homann. Implementation of a 3d thinning algorithm. *The Insight Journal* [<http://insight-journal.org>], 10 2007.
- [54] T. S. Hong, W. A. Tomé, R. J. Chappell, P. Chinnaiyan, M. P. Mehta, and P. M. Harari. The impact of daily setup variations on head-and-neck intensity-modulated radiation therapy. *Int J Radiat Oncol Biol Phys*, 61(3):779–788, Mar 2005.
- [55] Y. Hu, E.-J. Rijkhorst, R. Manber, D. Hawkes, and D. Barratt. Deformable vessel-based registration using landmark-guided coherent point drift. In *Proceedings of the 5th international conference on Medical imaging and augmented reality*, MIAR'10, pages 60–69, 2010.
- [56] T. C. Huang, G. Zhang, T. Guerrero, G. Starkschall, K. P. Lin, and K. Forster. Semi-automated ct segmentation using optic flow and fourier interpolation techniques. *Comput Methods Programs Biomed*, 84(2-3):124–134, Dec 2006.
- [57] D. P. Huyskens, P. Maingon, L. Vanuytsel, V. Remouchamps, T. Roques, B. Dubray, B. Haas, P. Kunz, T. Coradi, R. Bühlman, R. Reddick, A. V. Esch, and E. Salamon. A qualitative and a quantitative analysis of an auto-segmentation module for prostate cancer. *Radiotherapy and Oncology*, 90(3):337 – 345, 2009.
- [58] L. Ibanez, W. Schroeder, L. Ng, and J. Cates. *The ITK Software Guide*. Kitware Inc, NY, 2nd edition, 2005.
- [59] B. Jian and B. C. Vemuri. A robust algorithm for point set registration using mixture of Gaussians. *10th IEEE International Conference on Computer Vision (ICCV)*, 2:1246–1251, 2005.
- [60] H. J. Johnson and G. E. Christensen. Consistent landmark and intensity-based image registration. *IEEE Transactions on Medical Imaging*, 21(5):450–461, 2002.
- [61] S. Joshi and M. I. Miller. Landmark matching via large deformation diffeomorphisms. *IEEE Transactions on Image Processing*, 9(8):1357 – 1370, 2000.
- [62] T. Karkanis and A. J. Stewart. Curvature-dependent triangulation of implicit surfaces. *IEEE Computer Graphics and Applications*, 21:60–69, 2001.

-
- [63] M. R. Kaus, K. K. Brock, V. Pekar, L. A. Dawson, A. M. Nichol, and D. A. Jaffray. Assessment of a model-based deformable image registration approach for radiation therapy planning. *Int J Radiat Oncol Biol Phys*, 68(2):572–580, Jun 2007.
- [64] M. R. Kaus, V. Pekar, C. Lorenz, R. Truyen, S. Lobregt, and J. Weese. Automated 3-d pdm construction from segmented images using deformable models. *IEEE Transactions on Medical Imaging*, 22(8):1005–1013, 2003.
- [65] E. M. Kerkhof, B. W. Raaymakers, U. A. van der Heide, L. van de Bunt, I. M. Jürgenliemk-Schulz, and J. J. Lagendijk. Online mri guidance for healthy tissue sparing in patients with cervical cancer: An imrt planning study. *Radiotherapy and Oncology*, 88(2):241 – 249, 2008.
- [66] E. M. Kerkhof, R. W. van der Put, B. W. Raaymakers, U. A. van der Heide, I. M. Jürgenliemk-Schulz, and J. J. Lagendijk. Intrafraction motion in patients with cervical cancer: The benefit of soft tissue registration using mri. *Radiotherapy and Oncology*, 93(1):115 – 121, 2009.
- [67] M. L. Kessler. Image registration and data fusion in radiation therapy. *Br J Radiol*, 79(Special Issue 1):S99–108, 2006.
- [68] I.-K. Kolkman-Deurloo. *Intraoperative HDR Brachytherapy: Present and Future*. PhD thesis, Erasmus MC, Rotterdam, 2006.
- [69] N. Krahnstoever and C. Lorenz. Computing curvature-adaptive surface triangulations of three-dimensional image data. *The Visual Computer*, 20(1):17–36, 2004.
- [70] H. W. Kuhn. The Hungarian method for the assignment problem. *Naval Research Logistic Quarterly*, 2:83–97, 1955.
- [71] Y. C. Kuo, T. H. Wu, T. S. Chung, K. W. Huang, K. S. Chao, W. C. Su, and J. F. Chiou. Effect of regression of enlarged neck lymph nodes on radiation doses received by parotid glands during intensity-modulated radiotherapy for head and neck cancer. *Am J Clin Oncol*, 29(6):600–605, Dec 2006.
- [72] T. Lange, N. Papenberg, S. Heldmann, J. Modersitzki, B. Fischer, H. Lamecker, and P. M. Schlag. 3d ultrasound-ct registration of the liver using combined landmark-intensity information. *Int J Comput Assist Radiol Surg*, 4(1):79–88, 2009.

- [73] T. Lange, T. H. Wenckebach, H. Lamecker, M. Seebass, M. Hünnerbein, S. Eulenstein, B. Gebauer, and P. M. Schlag. Registration of different phases of contrast-enhanced ct/mri data for computer-assisted liver surgery planning: evaluation of state-of-the-art methods. *Int J Med Robot*, 1(3):6–20, 2005.
- [74] M. Larsson, B. Hedelin, I. Johansson, and E. Athlin. Eating problems and weight loss for patients with head and neck cancer: a chart review from diagnosis until one year after treatment. *Cancer Nurs*, 28(6):425–435, Nov-Dec 2005.
- [75] C. Lee, K. Langen, P. Kupelian, S. Meeks, c. R.R. Ma W. Lu, J. Haimerl, and G. Olivera. Positional and volumetric changes in parotid glands during head and neck radiation therapy assessed using deformable image registration. *Int J Radiat Oncol Biol Phys*, 69(3):S203 – S204, november 2007. Abstract.
- [76] D. Lee, W. H. Nam, J. Y. Lee, and J. B. Ra. Non-rigid registration between 3d ultrasound and ct images of the liver based on intensity and gradient information. *Phys Med Biol*, 56(1):117–137, 2011.
- [77] T.-C. Lee, R. L. Kashyap, and C.-N. Chu. Building skeleton models via 3-d medial surface/axis thinning algorithms. *CVGIP: Graph. Models Image Process.*, 56:462–478, November 1994.
- [78] D. Lesage, E. D. Angelini, I. Bloch, and G. Funka-Lea. A review of 3d vessel lumen segmentation techniques: Models, features and extraction schemes. *Medical Image Analysis*, 13(6):819–845, 2009.
- [79] P. Levendag, M. Hoogeman, D. Teguh, T. Wolf, L. Hibbard, O. Wijers, B. Heijmen, P. Nowak, E. Vásquez Osorio, and X. Han. Atlas based auto-segmentation of ct images: Clinical evaluation of using auto-contouring in high-dose, high-precision radiotherapy of cancer in the head and neck. *International Journal of Radiation Oncology*Biology*Physics*, 72(Supplement 1):S401 –, 2008.
- [80] P. Levendag, W. Nijdam, I. Noever, P. Schmitz, M. van de Pol, D. Sipkema, C. Braat, M. de Boer, and P. Jansen. Brachytherapy versus surgery in carcinoma of tonsillar fossa and/or soft palate: late adverse sequelae and performance status: can we be more selective and obtain better tissue sparing? *Int J Radiat Oncol Biol Phys*, 59(3):713–724, Jul 2004.

-
- [81] P. C. Levendag, D. N. Teguh, and B. Heijmen. *Principle and practice of radiation oncology*, chapter 42. Oropharynx. Lippincott Williams and Wilkins, 5th edition, 2007. (in press).
- [82] P. C. Levendag, D. N. Teguh, P. Voet, H. van der Est, I. Noever, W. J. de Kruijf, I.-K. Kolkman-Deurloo, J.-B. Prevost, J. Poll, P. I. Schmitz, and B. J. Heijmen. Dysphagia disorders in patients with cancer of the oropharynx are significantly affected by the radiation therapy dose to the superior and middle constrictor muscle: A dose-effect relationship. *Radiotherapy and Oncology*, 85(1):64 – 73, 2007.
- [83] X. Li, T. E. Yankeelov, T. E. Peterson, J. C. Gore, and B. M. Dawant. Automatic nonrigid registration of whole body ct mice images. *Medical Physics*, 35(4):1507–1520, 2008.
- [84] J. Liang and D. Yan. Reducing uncertainties in volumetric image based deformable organ registration. *Med. Phys.*, 30(8):2116–2122, Aug 2003.
- [85] K. Lim, V. Kelly, J. Stewart, J. Xie, Y.-B. Cho, J. Moseley, K. Brock, A. Fyles, A. Lundin, H. Rehbinder, and M. Milosevic. Pelvic radiotherapy for cancer of the cervix: Is what you plan actually what you deliver? *International Journal of Radiation Oncology*Biology*Physics*, 74(1):304 – 312, 2009.
- [86] Y. Liu. Automatic 3d free form shape matching using the graduated assignment algorithm. *Pattern Recogn.*, 38:1615–1631, October 2005.
- [87] X. Lu, S. Zhang, H. Su, and Y. Chen. Mutual information-based multimodal image registration using a novel joint histogram estimation. *Comput Med Imaging Graph*, 32(3):202–209, Apr 2008.
- [88] I. Macía. Generalized computation of gaussian derivatives using itk. *The Insight Journal* [<http://insight-journal.org>], 10 2007.
- [89] R. Mahdavi, E. Faramarzi, M. Mohammad-Zadeh, J. Ghaemmaghami, and M. V. Jabbari. Consequences of radiotherapy on nutritional status, dietary intake, serum zinc and copper levels in patients with gastrointestinal tract and head and neck cancer. *Saudi Med J*, 28(3):435–440, Mar 2007.
- [90] J. A. Maintz and M. A. Viergever. A survey of medical image registration. *Medical Image Analysis*, 2(1):1 – 36, 1998.

-
- [91] R. Manniesing, M. A. Viergever, and W. J. Niessen. Vessel axis tracking using topology constrained surface evolution. *IEEE Transactions on Medical Imaging*, 26:309–316, 2007.
- [92] L. Massoptier and S. Casciaro. Fully automatic liver segmentation through graph-cut technique. In *Conf Proc IEEE Eng Med Biol Soc*, pages 5243–5246, 2007.
- [93] G. J. Meijer, J. de Klerk, K. Bzdusek, H. A. van den Berg, R. Janssen, M. R. Kaus, P. Rodrigus, and P. P. van der Toorn. What ctv-to-ptv margins should be applied for prostate irradiation? four-dimensional quantitative assessment using model-based deformable image registration techniques. *Int J Radiat Oncol Biol Phys*, 72(5):1416–1425, Dec 2008.
- [94] E. H. W. Meijering, W. J. Niessen, J. P. W. Pluim, and M. A. Viergever. Quantitative comparison of sinc-approximating kernels for medical image interpolation. In *MICCAI*, pages 210–217, 1999.
- [95] A. Méndez Romero, J. Verheij, R. S. Dwarkasing, Y. Seppenwoolde, W. K. Redekop, P. E. Zondervan, P. J. Nowak, J. N. Ijzermans, P. C. Levendag, B. J. Heijmen, and C. Verhoef. Comparison of macroscopic pathology measurements with magnetic resonance imaging and assessment of microscopic pathology extension for colorectal liver metastases. *International Journal of Radiation Oncology*Biological*Physics*, In Press, Corrected Proof(-):-, 2010.
- [96] A. Méndez Romero, W. Wunderink, R. M. van Os, P. J. Nowak, B. J. Heijmen, J. J. Nuyttens, R. P. Brandwijk, C. Verhoef, J. N. Ijzermans, and P. C. Levendag. Quality of life after stereotactic body radiation therapy for primary and metastatic liver tumors. *Int J Radiat Oncol Biol Phys*, 70(5):1447–1452, Apr 2008.
- [97] A. Méndez Romero, R. T. Zinkstok, W. Wunderink, R. M. van Os, H. Joosten, Y. Seppenwoolde, P. J. Nowak, R. P. Brandwijk, C. Verhoef, J. N. Ijzermans, P. C. Levendag, and B. J. Heijmen. Stereotactic body radiation therapy for liver tumors: impact of daily setup corrections and day-to-day anatomic variations on dose in target and organs at risk. *Int J Radiat Oncol Biol Phys*, 75(4):1201–1208, Nov 2009.
- [98] P. Mitteroecker and P. Gunz. Advances in geometric morphometrics. *Evolutionary Biology*, 36:235–247, 2009.

-
- [99] M. J. Murphy, Z. Wei, M. Fatyga, J. Williamson, M. Anscher, T. Wallace, and E. Weiss. How does ct image noise affect 3d deformable image registration for image-guided radiotherapy planning? *Med Phys*, 35(3):1145–1153, Mar 2008.
- [100] A. Myronenko and X. Song. Point set registration: Coherent point drift. *IEEE Transactions on Pattern Analysis and Machine Intelligence*, 32:2262–2275, 2010.
- [101] J. Orban de Xivry, G. Janssens, G. Bosmans, M. De Craene, A. Dekker, J. Buijsen, A. van Baardwijk, D. De Ruyscher, B. Macq, and P. Lambin. Tumour delineation and cumulative dose computation in radiotherapy based on deformable registration of respiratory correlated ct images of lung cancer patients. *Radiother Oncol*, 85(2):232–238, Nov 2007.
- [102] A. Pearce, P. Craighead, I. Kay, L. Traptow, and C. Doll. Brachytherapy for carcinoma of the cervix: a canadian survey of practice patterns in a changing era. *Radiother Oncol*, 91(2):194–196, May 2009.
- [103] C. A. Perez and L. W. Brady, editors. *Principles and Practice of Radiation Oncology*. Lippincott - Raven Publishers, Philadelphia, USA, 3rd edition, 1998.
- [104] B. Polat, J. Wilbert, K. Baier, M. Flentje, and M. Guckenberger. Nonrigid patient setup errors in the head-and-neck region. *Strahlenther Onkol*, 183(9):506–511, Sep 2007.
- [105] A. Polo, C. Salembier, J. Venselaar, and P. Hoskin. Review of intraoperative imaging and planning techniques in permanent seed prostate brachytherapy. *Radiotherapy and Oncology*, 94(1):12 – 23, 2010.
- [106] K. Price. Relaxation matching techniques - a comparison. *IEEE Trans Pattern Anal Mach Intell*, 7(5):617–623, September 1985.
- [107] D. Ragan, G. Starkschall, T. McNutt, M. Kaus, T. Guerrero, and C. W. Stevens. Semiautomated four-dimensional computed tomography segmentation using deformable models. *Med Phys*, 32(7):2254–2261, Jul 2005.
- [108] J. L. Robar, A. Day, J. Clancey, R. Kelly, M. Yewondwossen, H. Hollenhorst, M. Rajaraman, and D. Wilke. Spatial and dosimetric variability of organs at risk in head-and-neck intensity-modulated radiotherapy. *Int J Radiat Oncol Biol Phys*, 68(4):1121–1130, Jul 2007.

- [109] P. Rogelj and S. Kovačič. Symmetric image registration. *Medical Image Analysis*, 10(3):484 – 493, 2006.
- [110] M. Rosu, I. J. Chetty, J. M. Balter, M. L. Kessler, D. L. McShan, and R. K. Ten Haken. Dose reconstruction in deforming lung anatomy: dose grid size effects and clinical implications. *Med Phys*, 32(8):2487–2495, Aug 2005.
- [111] Y. Sato, S. Nakajima, N. Shiraga, H. Atsumi, S. Yoshida, T. Koller, G. Gerig, and R. Kikinis. 3d multi-scale line filter for segmentation and visualization of curvilinear structures in medical images. *Medical Image Analysis*, 2(2):143–168, 1998.
- [112] Y. Sato, C. Westin, A. Bhalerao, S. Nakajima, N. Shiraga, S. Tamura, and R. Kikinis. Tissue classification based on 3d local intensity structures for volume rendering. *IEEE Transactions on Visualization and Computer Graphics*, 6:160–180, 2000.
- [113] B. Schaly, G. Bauman, J. Battista, and J. Van Dyk. Validation of contour-driven thin-plate splines for tracking fraction-to-fraction changes in anatomy and radiation therapy dose mapping. *Phys. in Medicine and Biology*, 50(3), Feb 2005.
- [114] B. Schaly, J. A. Kempe, G. S. Bauman, J. J. Battista, and J. Van Dyk. Tracking the dose distribution in radiation therapy by accounting for variable anatomy. *Phys Med Biol*, 49(5):791–805, Mar 2004.
- [115] I. Schoenberg. Contributions to the problem of approximation of equidistant data by analytic functions. *Quart. Appl. Math.*, 4:45 – 99 and 112 – 141, 1946.
- [116] M. Sharpe and K. K. Brock. Quality assurance of serial 3d image registration, fusion, and segmentation. *International Journal of Radiation Oncology*Biography*Physics*, 71(1, Supplement):S33 – S37, 2008.
- [117] R. Sinkhorn. A Relationship Between Arbitrary Positive Matrices and Doubly Stochastic Matrices. *The Annals of Mathematical Statistics*, 35(2):876–879, 1964.
- [118] L. Soler, H. Delingette, G. Malandain, J. Montagnat, N. Ayache, C. Koehl, O. Dourthe, B. Malassagne, M. Smith, D. Mutter, and J. Marescaux. Fully automatic anatomical, pathological, and functional segmentation from ct scans for hepatic surgery. *Comput Aided Surg*, 6(3):131–142, 2001.

-
- [119] G. G. Steel, editor. *Basic clinical radiobiology*. Hodder Arnold, London, 2nd edition, 2002.
- [120] D. Suter and F. Chen. Left ventricular motion reconstruction based on elastic vector splines. *IEEE Trans. Med. Imaging*, 19(4):295–305, 2000.
- [121] G. Taubin. Curve and surface smoothing without shrinkage. In *Proceedings of the Fifth International Conference on Computer Vision, ICCV '95*, pages 852–, Washington, DC, USA, 1995. IEEE Computer Society.
- [122] G. Taubin. A signal processing approach to fair surface design. In *Proceedings of the 22nd annual conference on Computer graphics and interactive techniques, SIGGRAPH '95*, pages 351–358, New York, NY, USA, 1995. ACM.
- [123] D. N. Teguh, P. C. Levendag, I. Noever, P. van Rooij, P. Voet, H. van der Est, D. Sipkema, A. Sewnaik, R. J. Baatenburg de Jong, D. de la Bijde, and P. I. Schmitz. Treatment techniques and site considerations regarding dysphagia-related quality of life in cancer of the oropharynx and nasopharynx. *Int J Radiat Oncol Biol Phys*, 72(4):1119–1127, Nov 2008.
- [124] D. N. Teguh, P. C. Levendag, P. Voet, H. van der Est, I. Noever, W. de Kruijff, P. van Rooij, P. I. M. Schmitz, and B. J. Heijmen. Trismus in patients with oropharyngeal cancer: Relationship with dose in structures of mastication apparatus. *Head & Neck*, 30(5):622–630, 2008.
- [125] C. Thilmann, S. Nill, T. Tücking, A. Höss, B. Hesse, L. Dietrich, R. Bendl, B. Rhein, P. Häring, C. Thieke, U. Oelfke, J. Debus, and P. Huber. Correction of patient positioning errors based on in-line cone beam cts: clinical implementation and first experiences. *Radiat Oncol*, 1:16, 2006.
- [126] J. P. Thirion. Image matching as a diffusion process: an analogy with maxwell's demons. *Med Image Anal*, 2(3):243–260, 1998.
- [127] N. Ueda and R. Nakano. Deterministic annealing em algorithm. *Neural Networks*, 11(2):271 – 282, 1998.
- [128] A. E. van der Pool, A. Méndez Romero, W. Wunderink, B. J. Heijmen, P. C. Levendag, C. Verhoef, and J. N. Ijzermans. Stereotactic body radiation therapy for colorectal liver metastases. *Br J Surg*, 97(3):377–382, Mar 2010.

- [129] G. J. van der Wielen, T. F. M. L. Incrocci, W. J. Kirkels, E. M. Vásquez Osorio, M. S. Hoogeman, B. J. Heijmen, and H. J. de Boer. Deformation of the prostate and seminal vesicles relative to intraprostatic fiducial markers. *Int J Radiat Oncol Biol Phys*, 72(5):1604–1611, Dec 2008.
- [130] M. van Herk. Different styles of image-guided radiotherapy. *Seminars in Radiation Oncology*, 17(4):258 – 267, 2007.
- [131] E. Vásquez Osorio, M. Hoogeman, A. Al-Mamgani, D. Teguh, P. Levendag, and B. Heijmen. Non-rigid point matching and its application in radiotherapy. *ICCR: Proceedings of the XVth International Conference on the Use of Computers in Radiation Therapy*, 2:413–417, June 2007.
- [132] E. M. Vásquez Osorio, M. S. Hoogeman, A. Al-Mamgani, D. N. Teguh, P. C. Levendag, and B. J. Heijmen. Local anatomic changes in parotid and submandibular glands during radiotherapy for oropharynx cancer and correlation with dose, studied in detail with nonrigid registration. *Int J Radiat Oncol Biol Phys*, 70(3):875–882, Mar 2008.
- [133] E. M. Vásquez Osorio, M. S. Hoogeman, L. Bondar, P. C. Levendag, and B. J. Heijmen. A novel flexible framework with automatic feature correspondence optimization for nonrigid registration in radiotherapy. *Med Phys*, 36(7):2848–2859, Jul 2009.
- [134] E. M. Vásquez Osorio, M. S. Hoogeman, D. N. Teguh, A. Al-Mamgani, I.-K. K. Kolkman-Deurloo, L. Bondar, P. C. Levendag, and B. J. Heijmen. Three-dimensional dose addition of external beam radiotherapy and brachytherapy for oropharyngeal patients using nonrigid registration. *International Journal of Radiation Oncology*Biological*Physics*, 80(4):1268 – 1277, 2011.
- [135] J. P. Voroney, K. K. Brock, C. Eccles, M. Haider, and L. A. Dawson. Prospective comparison of computed tomography and magnetic resonance imaging for liver cancer delineation using deformable image registration. *Int J Radiat Oncol Biol Phys*, 66(3):780–791, 2006.
- [136] G. Wahba. *Spline models for observational data*, volume 59 of *CBMS-NSF Regional Conference Series in Applied Mathematics*. Society for Industrial and Applied Mathematics (SIAM), 1990.
- [137] W. M. Wells III. Statistical approaches to feature-based object recognition. *International Journal of Computer Vision*, 21:63–98, 1997.

-
- [138] M. Wendling, L. J. Zijp, L. N. McDermott, E. J. Smit, J. J. Sonke, B. J. Mijnheer, and M. van Herk. A fast algorithm for gamma evaluation in 3d. *Med Phys*, 34(5):1647–1654, May 2007.
- [139] W. Wunderink, A. Méndez Romero, W. de Kruijf, H. de Boer, P. Levendag, and B. Heijmen. Reduction of respiratory liver tumor motion by abdominal compression in stereotactic body frame, analyzed by tracking fiducial markers implanted in liver. *Int J Radiat Oncol Biol Phys*, 71(3):907–915, 2008.
- [140] L. Xiong, A. Viswanathan, A. J. Stewart, S. Haker, C. M. Tempany, L. M. Chin, and R. A. Cormack. Deformable structure registration of bladder through surface mapping. *Medical Physics*, 33(6):1848–1856, 2006.
- [141] D. Yang, S. R. Chaudhari, S. M. Goddu, D. Pratt, D. Khullar, J. O. Deasy, and I. E. Naqa. Deformable registration of abdominal kilovoltage treatment planning ct and tomotherapy daily megavoltage ct for treatment adaptation. *Medical Physics*, 36(2):329–338, 2009.
- [142] D. Yang, H. Li, D. A. Low, J. O. Deasy, and I. E. Naqa. A fast inverse consistent deformable image registration method based on symmetric optical flow computation. *Physics in Medicine and Biology*, 53(21):6143–6165, 2008.
- [143] J. Yang. The thin plate spline robust point matching (tps-rpm) algorithm: A revisit. *Pattern Recognition Letters*, 32(7):910 – 918, 2011.
- [144] A. L. Yuille and J. Kosowsky. Statistical physics algorithms that converge. *Neural Computation*, 6(3):341–356, 1994.
- [145] L. Zagorchev and A. Goshtasby. A comparative study of transformation functions for nonrigid image registration. *IEEE Trans Image Process*, 15(3):529–538, Mar 2006.
- [146] M. J. Zelefsky, M. A. Nedelka, Z. L. Arican, Y. Yamada, G. N. Cohen, A. M. Shippy, J. J. Park, and M. Zaider. Combined brachytherapy with external beam radiotherapy for localized prostate cancer: reduced morbidity with an intraoperative brachytherapy planning technique and supplemental intensity-modulated radiation therapy. *Brachytherapy*, 7(1):1–6, Jan-Mar 2008.

- [147] G. G. Zhang, T. C. Huang, K. M. Forster, K. P. Lin, C. Stevens, E. Harris, and T. Guerrero. Dose mapping: validation in 4d dosimetry with measurements and application in radiotherapy follow-up evaluation. *Comput Methods Programs Biomed*, 90(1):25–37, Apr 2008.
- [148] Z. Zhang, Y. Jiang, and H. Tsui. Consistent multi-modal non-rigid registration based on a variational approach. *Pattern Recognition Letters*, 27(7):715 – 725, 2006.
- [149] H. Zhong, J. Kim, and I. J. Chetty. Analysis of deformable image registration accuracy using computational modeling. *Med Phys*, 37(3):970–979, 2010.
- [150] B. Zitová and J. Flusser. Image registration methods: a survey. *Image and Vision Computing*, 21(11):977 – 1000, 2003.

Summary

Technical improvements in treatment planning, dose delivery and image-guided patient positioning have substantially extended the possibilities for treating cancer with radiation. However, changes in patient anatomy currently limit the full exploitation of these techniques. As long as these changes are rigid, the anatomy changes can be accounted for by a relatively simple rigid alignment of two images. However, often anatomical changes are non-rigid and a rigid alignment is not sufficient. Some examples are the organ deformation caused by variations in the filling of the bladder, rectum and other parts of the intestine, the deformation in head and neck patients due to shrinkage of the tumor and other tissue, and the deformation of the liver if abdominal compression is applied to limit respiratory motion. At all stages of the radiotherapy process, i.e. target delineation, treatment planning, and dose delivery, these non-rigid deformations may negatively influence the treatment accuracy. Typically, safety margins around the target are used to compensate the loss of accuracy, which often results in a considerable amount of healthy tissue being irradiated. To further improve radiation treatments, anatomical changes need to be modeled and accounted for. The feature-based non-rigid registration method presented in this thesis intends to help advance radiotherapy in this direction.

This thesis describes the improvements of a feature-based non-rigid registration method which were essential to make it suitable for radiotherapy, and presents three practical applications in this field. The original method, thin-plate splines – robust point matching (TPS-RPM) proposed by Chui and Rangarajan in [25], is point-based, meaning that the structures to be registered are represented by two sets of points. The method iteratively estimates point correspondence between the two sets, and updates a non-rigid transformation modeled by a thin-plate spline, (chapter 2). The method was improved to register multiple organs simultaneously and to include a-priori information in the form of anatomical landmarks and corresponding structures (chapter 3). Furthermore, the method was extended in order to generate consistent results that are independent of the direction of the registration (chapter 4).

The quality of the transformation resulting from the registration was assessed via different methods. The average distance between the transformed surface and the reference surface was used to determine the transformation accuracy. In chapters 3 and 4, method parameters were tuned for cases with different degrees of deformation: head and neck, prostate and cervix. Transformation accuracies below 1 mm were achieved for a subset of the parameter values.

Another metric used to assess the transformation quality was the transformation consistency error. When a set of points A is registered to a set of points B, the non-rigid transformation $T_{A \rightarrow B}$ is obtained. Similarly, the transformation $T_{B \rightarrow A}$ is found when set B is registered to set A. Given that the point sets are kept the same in both registrations, it is expected that $T_{B \rightarrow A}$ is the inverse of $T_{A \rightarrow B}$. The consistency error aims to measure the agreement between the transformations on the organ's surfaces. More formally, the consistency error is the average of $d(p, T_{B \rightarrow A}(T_{A \rightarrow B}(p)))$ for all points p on the surface of the point set A. A value of zero indicates perfect agreement, that is, that $T_{B \rightarrow A}$ is the inverse of $T_{A \rightarrow B}$ for the points on the surface of the organs. Values for the transformation consistency error ranged between 1.0 and 1.7 mm for the prostate and head and neck cases (chapters 3 and 5), and between 4.0 and 4.6 mm for the cervix cases (chapters 3). In chapter 4, after reinforcing transformation consistency, the consistency error reduced to around 1 mm for cervix cases with extreme deformation.

As mentioned above, the method can be tuned by setting different values for internal parameters. The 'non-rigidity' of the transformation can be changed by varying the value of λ . Chapters 3 and 4 explore the influence of this parameter on the transformation accuracy and consistency. Large values of λ restrict the transformation to be mostly affine, while low values relax this restriction. Optimal values for λ for different sites and levels of deformation were found and subsequently applied. The level of detail of the registration can be set by selecting the density of the points (parameter r for density radius, or ρ for point density in chapter 4). Using many points results in transformations with low transformation errors, but requires a large computational time. Conversely, using very few points accelerates the transformation, but local deformations may not be properly aligned. In chapters 3 and 4 several point set densities were evaluated, and recommendations are given for different sites and degrees of deformation.

Safe application of non-rigid registration in radiotherapy requires anatomical validation. However, a quantitative anatomical validation is still a challenge, since ground truth is hardly available. In this thesis, the transformations were validated by assessing the residual distances after transformation of anatomical landmarks and structures. In chapter 3, 4 and 7 points and lines were used to mark anatomical features. Table S.1 lists the anatomical features used per site in these chapters. In chapter 6, a robustness analysis was used as an alternative to validation against ground truth data.

Table S.1: *Anatomical landmarks and structures used for validation.*

Site	Anatomical feature
Head and neck	Parotid gland - Mandible interface (line)
	Parotid gland - Styloid process interface (line)
	Parotid gland: top and bottom
	Submandibular gland: top and bottom
Prostate	Implanted gold markers (line)
	Prostate apex
	Vesicles tips
Cervix	Uterus midline (line)
	Uterus tip
	Calcifications in the Uterus
	Implanted markers
	Bladder top and bottom
Liver	Vessel bifurcations
	Cysts
	Implanted markers
	Biliary tree bifurcations

In addition to the technical improvements on the original method and the validation experiments, this thesis presents three successful applications of the improved method in radiotherapy: quantification of anatomical changes in 3 dimensions for head and neck cancer patients, addition of dose distributions for two radiation therapy modalities (external beam radiotherapy and brachytherapy) for head and neck cancer patients and registration of largely deformed livers by automatically segmenting and registering vessels.

In chapter 5, non-rigid registration was used to quantify the anatomical changes after external beam radiotherapy (EBRT) in head and neck (H&N) cancer patients. The method was applied to data of 10 H&N cancer patients. Two CT scans were available per patient: the planning CT and a repeat CT scan after the dose delivery of 46 Gy. The salivary glands (parotid and submandibular glands) and the tumor were first contoured and then registered non-rigidly. Each gland was labeled as either 'spared' (if it did not belong to a treated neck), or 'irradiated' (if it belonged to a treated neck), resulting in 15 irradiated glands and 5 spared glands. Deformation patterns were found after summarizing the

registration results of all the patients. The lateral regions of the irradiated parotid glands moved inwards (on average 3 mm), while the medial regions tended to remain in the same position. The irradiated submandibular glands shrank and moved in the cranial direction. The spared glands showed only a small deformation (around 1 mm in most regions). Additionally, the volume loss of the parotid glands was found to be proportional to the planned mean dose ($p < 0.001$).

In chapter 6, the non-rigid registration method was used to add dose distributions in the presence of anatomical changes for patients with oropharyngeal cancer who received a combination EBRT and brachytherapy (BT). For each of the five patients, two CT scans were used: the CT used for EBRT planning, and a CT acquired after catheter implantation, just before BT delivery. The EBRT and BT planned dose distributions were available. The salivary glands, chewing and swallowing muscles were contoured and registered. Then the BT dose distribution was mapped onto the EBRT dose distribution by applying the transformation obtained. To account for differences in fractionation, the physical doses were converted to a biologically equivalent dose in fractions of 2Gy (EQD_2), and the total dose was obtained by adding dose voxel by voxel. As an alternative for validation, the robustness of the dose addition was investigated by varying parameters of the dose accumulation and input data. Various values for the parameters for the point density ($r = \{5, 6, 8\}$), transformation stiffness ($\lambda = \{5, 0.5\}$) and the α/β ratio for EQD_2 (2.4, 2.7, 3.3 and 3.6 Gy) were used. Additionally, variations in the delineations of the organs were simulated and the locations of the points on the organ's surface were varied. The effect of the perturbations was evaluated using Dose-Volume Histograms (DVH) and strict gamma analyses (Distance-To-Agreement/Dose-Difference=1mm/1Gy). Analysis showed that the gamma index was moderately elevated for more flexible registrations ($\lambda = 0.5$), and large delineation variations (5 mm). An analysis of the perturbations per organ showed that the gamma index was moderately elevated for organs lying in areas with a steep gradient (median gamma index ≤ 2.3 for constrictor muscles) and low for the rest or the organs (≤ 0.7). In the DVH of the added dose distributions, only small variations were observed. In conclusion, the non-rigid registration method provides a solution for adding EBRT and BT dose distributions in the presence of anatomical changes for oropharyngeal cancer patients. Areas with steep gradients still present challenges but in general, the method is reliable and robust with respect to uncertainties in organ delineation, perturbations in method parameters and α/β values for EQD_2 .

In chapter 7, the non-rigid registration method was adapted to automatically segment and register vessels from CT and magnetic resonance (MR) images for seven liver cancer patients. Registration of MR and CT scans was not straightforward because the CT and MR scans were acquired under different conditions. During the acquisition of the MR scan, the patients were asked to hold their breath. The CT scan, on the other hand, was acquired in treatment position while applying abdominal compression to limit motion induced by breathing. The abdominal compression caused large deformations of the liver shape in the CT with respect to the liver shape in the MR image set. To automatically segment vessels, a vesselness measure was used. The segmented vessels were then thinned and registered with the non-rigid registration method. Two strategies were investigated and validated: Strategy A, which registered midlines of thick vessels first while midlines of thinner vessels were added at each iteration; and strategy B, which registered all vessels' midlines at once. To validate the method, residual distances for corresponding vessel bifurcations and additional anatomical landmarks were calculated. To estimate the deformation of the liver, the residual distances of the aforementioned anatomical points were calculated after rigid registration. The deformation of the liver ranged between 2.8 and 10.7 mm. The residual distances reduced to 1.6 (1.3-1.9) and 1.5 (1.1-2.3) mm after non-rigid registration, for bifurcations and anatomical landmarks, respectively. Due to differences in contrast between both scan modalities, a large number of points did not have a corresponding point in the other point set (outliers). Additionally, the vessel segmentation also produced false positives. The algorithm was able to identify these points, and consequently, they were not used in the computation of the transformation. Strategy A executed faster than B (>2.4 times), while the accuracy was similar.

In conclusion, the feature-based non-rigid registration method presented in this thesis registers multiple organs in an accurate, consistent, and anatomically coherent way. Furthermore, non-rigid registration is essential for many applications in radiotherapy, such as dose addition and image alignment. The method is a useful tool that could support further developments in high-precision image-guided adaptive radiotherapy.

Samenvatting

De mogelijkheden om tumoren te kunnen behandelen met ioniserende straling zijn sterk toegenomen met de komst van verbeterde technieken voor dosisplanning, het beeldgestuurd positioneren van patiënten en dosistoediening. Veranderingen in de anatomie van een patiënt, die mogelijk optreden tijdens de voorbereiding en/of uitvoering van een behandeling, kunnen daarentegen het optimaal gebruik van deze technieken belemmeren. Het is relatief eenvoudig om bij een behandeling rekening te houden met van nature rigide anatomische veranderingen (veranderingen waarbij de vorm van het object niet wezenlijk verandert) omdat de afbeeldingen van voor en na de verandering eenvoudig op elkaar te passen zijn (in het vervolg aangeduid met de term *registratie*). Vaak echter zijn anatomische veranderingen niet-rigide en biedt een rigide registratie geen bevredigend resultaat. Zo is een rigide methode niet geschikt voor het registreren van vervormingen die zijn ontstaan door verandering in de vulling van de blaas, het rectum, en overige delen van het spijsverteringssysteem, niet voor vervormingen door het krimpen van tumoren en ander weefsel bij hoofd-hals patiënten en niet voor vervorming in de lever die ontstaat door het toepassen van abdominale compressie voor het beperken van de beweging door ademhaling. Dergelijke niet-rigide vervormingen kunnen een rol spelen bij alle stappen van het radiotherapieproces, namelijk het definiëren van het tumorvolume, het opstellen van het bestralingsplan en de bestraling zelf. Zij beperken de nauwkeurigheid van een behandeling als geheel. Voor het compenseren van onnauwkeurigheid wordt in de praktijk een marge rondom het doelvolume aangebracht, waarmee een gebied wordt bestraald dat groter is dan het eigenlijke doelvolume. Bijgevolg wordt dus voor een deel gezond weefsel bestraald. Om radiotherapiebehandelingen verder te verbeteren en marges te kunnen beperken, is het zaak ook rekening te houden met niet-rigide anatomische veranderingen. Modelleren van deze veranderingen biedt hiervoor uitkomst. Met het presenteren van een methode voor kenmerkgestuurde niet-rigide registratie beoogt dit proefschrift hieraan bij te dragen.

Dit proefschrift beschrijft de verbeteringen die zijn aangebracht op een kenmerkgestuurde niet-rigide registratiemethode voor het toepasbaar maken van de methode in de radiotherapiepraktijk en behandelt drie praktische toepassingen. De originele registratiemethode, het 'thin-plate splines – robust point matching' (TPS-RPM) algoritme, werd door Chui en Rangarajan [25] geïntroduceerd. Bij deze puntgestuurde methode worden structuren gerepresenteerd door verzamelingen punten waarop de eigenlijke operaties worden toegepast. De correspondentie tussen twee puntenverzamelingen wordt iteratief geschat,

waarbij telkens een niet-rigide transformatie wordt doorgevoerd via 'thin-plate splines' modellering (hoofdstuk 2). De methode is aangepast om meerdere organen tegelijk te kunnen registreren en daarbij gebruik te maken van apriori informatie in de vorm van anatomische referentiepunten en karakteristieke structuren (hoofdstuk 3). Ook is de methode uitgebreid om, onafhankelijk van de functionele richting van de registratie, een consistent resultaat te verkrijgen (hoofdstuk 4).

De kwaliteit van een registratie is met diverse methoden vastgesteld. Zo is de transformatienauwkeurigheid bepaald aan de hand van de gemiddelde afstand tussen het referentie en getransformeerde oppervlak. In hoofdstuk 3 en 4 zijn de parameterwaarden van de methode afgestemd op de mate van vervorming die optreedt in de diverse tumorgebieden, zoals hoofd-hals, prostaat, en baarmoederhals. Met geselecteerde parameterwaarden werd een nauwkeurigheid beneden 1 mm bereikt. In de hoofdstukken 5 en 6 zijn eveneens parameterwaarden bepaald die een transformatienauwkeurigheid beneden 1 mm opleverden.

Ook is de registratiekwaliteit bepaald aan de hand van een foutmaat voor de consistentie van de transformatie. Stel dat het registreren van een puntenverzameling A met een puntenverzameling B, de niet-rigide registratie $T_{A \rightarrow B}$ oplevert en dat het verwisselen van de rollen van A en B de transformatie $T_{B \rightarrow A}$ oplevert. Dan zal, aannemende dat A en B voor beide transformaties gelijk zijn, voor een consistente transformatie gelden dat $T_{B \rightarrow A}$ de inverse is van $T_{A \rightarrow B}$. De transformatie-consistentie-fout wordt geïntroduceerd om de mate van overeenstemming tussen beide transformaties op het orgaanoppervlak te meten en is gedefinieerd als het gemiddelde van $d(p, T_{B \rightarrow A}(T_{A \rightarrow B}(p)))$ voor alle punten p op het oppervlak. Een waarde 0 duidt op perfecte overeenstemming zodat $T_{B \rightarrow A}$ gelijk is aan de inverse van $T_{A \rightarrow B}$. De transformatie-consistentie-fout varieerde tussen 1.0 en 1.7 mm voor prostaat en hoofd-hals casussen (hoofdstuk 3 en 5), en tussen 4.0 en 4.6 mm voor baarmoederhals casussen (hoofdstuk 3). In hoofdstuk 4 is met het opleggen van consistentie aan de methode bereikt dat voor baarmoederhals casussen met extreme vervormingen de transformatie-consistentie-fout tot ongeveer 1 mm kon worden teruggebracht.

Zoals eerder opgemerkt, kan door de keuze van de parameterwaarden, de methode worden afgestemd op verschillende situaties. Parameter λ bepaalt de deformeerbaarheid van de transformatie. In hoofdstukken 3 en 4 is de invloed van λ op de nauwkeurigheid en consistentie van de transformatie onderzocht. Grote waarden van λ maken de methode relatief stijf (neigend

naar een affiene transformatie) terwijl kleine waarden juist meer deformatie toestaan. Voor diverse tumorgebieden en daaraan gerelateerde deformaties, zijn optimale waarden van λ vastgesteld en toegepast. De gedetailleerdheid van de registratie kan worden ingesteld door de keuze van de puntendichtheid op het oppervlak (parameters r voor dichtheidsradius en ρ voor puntendichtheid). Een hoge puntendichtheid leidt tot relatief kleine fouten maar vergt ook meer rekentijd. Een lage puntendichtheid versnelt de berekening maar laat lokaal gedeformeerde oppervlakken niet altijd goed samenvallen. In hoofdstuk 3 en 4 zijn op grond van diverse evaluaties aanbevelingen opgesteld voor de keuze van de puntendichtheid bij diverse tumorgebieden en daaraan gerelateerde deformaties.

Om een veilig gebruik van de niet-rigide registratiemethode voor radiotherapie zeker te stellen, is het valideren van de methode noodzakelijk. Door het veelal ontbreken van kennis over de werkelijkheid, vormt een kwantitatieve anatomische validatie echter een grote uitdaging. In dit proefschrift zijn de transformaties gevalideerd door het vaststellen van de afstanden tussen de corresponderende anatomische referentiepunten of structuren die resulteren na transformatie. In de hoofdstukken 3, 4 en 7 zijn punten en lijnen gebruikt om anatomische kenmerken te markeren. Tabel S.1 geeft een overzicht van de anatomische kenmerken die gebruikt zijn voor de verschillende tumorgebieden in deze hoofdstukken. In hoofdstuk 6, is een analyse naar de robuustheid uitgevoerd als alternatief voor een vergelijking met de ontbrekende kennis over de werkelijkheid.

Naast de technische verbeteringen op de originele methode en de validatie-experimenten, worden in dit proefschrift ook drie geslaagde radiotherapie-toepassingen behandeld, namelijk: het kwantificeren van anatomische veranderingen in drie dimensies (3D) bij hoofd-hals-kankerpatiënten, het optellen van dosisverdelingen voor een combinatie van twee radiotherapiebehandelingen (uitwendige radiotherapie en brachytherapie) bij hoofd-hals-kankerpatiënten en tenslotte het registreren van twee afbeeldingen van onderling sterk vervormde levers door het automatisch segmenteren en registreren van vaten.

Hoofdstuk 5 beschrijft het gebruik van niet-rigide registratie voor het kwantificeren van 3D anatomische veranderingen als gevolg van bestraling bij hoofd-hals-kankerpatiënten. De methode is toegepast op beelden van 10 hoofd-hals-patiënten. Per patiënt werden twee CT-scans gebruikt: de scan voor dosisplanning en de vervolgscaan na bestraling met 46 Gy. De speekselklieren (de parotis en glandula submandibularis) en de tumor werden ingetekend en daarna niet-rigide geregistreerd. De speekselklieren werden

Tabel S.1: Anatomische referentiepunten en structuren gebruikt voor validatie.

Locatie	Anatomisch kenmerk
Hoofd-hals	parotis (oorspeekselklier) – mandibula overgang (lijn) Parotis – processus styloideus overgang (lijn) Parotis boven- en onderzijde Glandula submandibularis (onderkaak speekselklier) boven- en onderzijde
Prostaat	Geïmplanteerde goudmarker (lijn) Prostaat top Zaadblaasje top
Baarmoederhals	Baarmoeder hartlijn (lijn) Baarmoeder top Verkalkingen in de baarmoeder Geïmplanteerde marker Blaas boven- en onderzijde
Lever	Vaatvertakkingen Cysten Geïmplanteerde markers Vertakkingen galwegen

gelabeld als 'bestraald' of 'gespaard' afhankelijk van hun locatie respectievelijk in of buiten een behandelde nekhelft. Dit resulteerde in 15 bestraalde en 5 gespaarde speekselklieren. Na het samenvoegen van alle resultaten werden de algemene karakteristieken van deformatie zichtbaar. De laterale zijden van bestraalde parotiden vertonen een naar binnen gerichte verplaatsing (gemiddeld 3 mm), terwijl de mediale zijden vrijwel geen verplaatsing hadden ondergaan. Bestraalde glandulae submandibulares waren gekrompen en in craniale richting verplaatst. Gespaarde speekselklieren vertoonden slechts kleine vervormingen (in de orde grootte van 1 mm op de meeste plekken). Ook werd vastgesteld dat volumevermindering van parotiden toenam met de geplande gemiddelde dosis straling op dit orgaan ($p < 0.001$).

Hoofdstuk 6 beschrijft het gebruik van niet-rigide registratie voor het optellen van dosisverdelingen in aanwezigheid van anatomische veranderingen bij patiënten met orofaryngeale kanker (kanker aan de mond- of keelholte)

die een combinatietherapie bestaande uit uitwendige radiotherapie (URT) en brachytherapie (BT) ondergingen. Voor elk van de vijf patiënten zijn twee CT-scans gebruikt, de scan voor URT dosisplanning en de scan verkregen na het aanbrengen van katheters voor de BT behandeling. Bij elke scan behoorde een geplande dosisverdeling. De speekselklieren en de kauwen slijkspiers, werden ingetekend en geregistreerd. Door het toepassen van de transformatie verkregen uit deze registratie, is vervolgens de BT dosisverdeling toegekend aan de URT dosisverdeling. Om rekening te houden met verschillen in fractionering, werd daarbij de reële dosis eerst omgezet in de equivalente dosis in fracties van 2 Gy (EQD_2), waarna door optelling de dosis per voxel werd verkregen. Als alternatief voor valideren is de robuustheid van de dosisoptelling onderzocht door de parameters van de niet-rigide registratiemethode te variëren ($r = 5, 6, 8$ en $\lambda = 5$ en 0.5) en door het invoeren van verschillende puntenverdelingen (4 verschillende wolken), intekeningen (willekeurige variaties in de contouren met maxima van 1, 3 en 5 mm) en α/β parameters behorende tot de EQD_2 berekening (2.4, 2.7, 3.3 en 3.6). Het effect van deze variaties werd geëvalueerd met het dosis-volume-histogram (DVH) en een strikte vorm van gamma-analyse (afstand tot overeenkomst = 1 mm, dosisverschil = 1 Gy). Uit de analyse blijkt dat een toenemende flexibiliteit van de registratie aanleiding geeft tot een lichte verhoging van de gamma index. Ook een variatieanalyse per orgaan laat een lichte verhoging van de gamma-index zien voor die organen welke gelegen zijn in gebieden waar een grote dosisgradiënt werd aangebracht (mediaan gamma index ≤ 2.3 voor musculus constrictor en ≤ 0.7 voor overige organen). De effecten van variatie op het DVH van opgetelde dosisverdelingen waren gering. Samenvattend kan gesteld worden dat de niet-rigide registratiemethode een geschikt instrument vormt voor het optellen van dosisverdelingen in aanwezigheid van anatomische veranderingen bij patiënten met orofaryngeale kanker die een URT-BT-combinatietherapie ondergaan. Hoewel gebieden met grote dosisgradiënten nochtans gevoelig zijn voor afwijkingen, is de methode in het algemeen betrouwbaar en robuust bij onderwerping aan intekenonzekerheden, parametervariaties, en variatie van EQD_2 α/β waarden.

In hoofdstuk 7 is de niet-rigide registratiemethode aangepast om in CT en MR (kernspin/magnetische resonantie) beelden van zeven leverpatiënten, levervaten automatisch te segmenteren en vervolgens te kunnen registreren. De CT- en MRI-scans werden onder verschillende omstandigheden en op verschillende tijdstippen gemaakt. Voor het maken van de MRI-scan werd aan patiënten gevraagd de adem in te houden, terwijl voor de CT-scan, pati-

ënten in behandelpositie werden neergelegd, waarbij abdominale compressie de ademhalingsbeweging verminderde. De MR beelden toonden duidelijk de grote leververvorming veroorzaakt door de abdominale compressie. De scans werden ongeveer twee weken na elkaar gemaakt. Om de MR- met CT-beelden te registreren zijn in beide beelden de levervaten automatisch gesegmenteerd op basis van een maat voor vaatovereenkomst. Vervolgens zijn in beide beelden de hartlijnen van gedetecteerde vaten bepaald waarna deze werden geregistreerd met een aangepaste versie van het TPS-RPM-algorithme. Twee strategieën werden daarbij onderzocht en gevalideerd: Bij strategie A werden in iedere iteratie eerst de hartlijnen van de bredere vaten geregistreerd en daarna de hartlijnen van de nauwere vaten toegevoegd en bij strategie B werden de hartlijnen van alle vaten tegelijkertijd geregistreerd. Ter validatie van de methode zijn de afstanden bepaald tussen overeenkomstige vaatvertakkingen en andere anatomische referentiepunten die resulteerden na registratie. Als uitgangspunt zijn de CT en MR scans eerst rigide geregistreerd. Deze vergelijking van rigide registratie met niet-rigide registratie laat zien dat de gemiddelde residu-afstanden van respectievelijk vaatvertakkingen en anatomische referentiepunten afneemt van (gemiddelde en bereik): 5.4 (2.8-10.2) en 6.0 (3.5-10.7) mm naar 1.6 (1.3-1.9) en 1.5 (1.1-2.3) mm. Door verschillen in contrast tussen beide scanmodaliteiten werd voor een groot aantal punten geen correspondentie gevonden tussen beide scans (uitschieters). Ook leverde de segmentatie van vaten soms valse posities (geen vaten) op. Met de methode die werd ontwikkeld kunnen deze punten echter worden gedetecteerd en weggelaten bij de transformatieberekening. Strategie A vergde minder rekentijd dan strategie B (>2.4 keer), terwijl de nauwkeurigheid vergelijkbaar was.

Concluderend kan gesteld worden dat de kenmerkgestuurde niet-rigide registratiemethode die in dit proefschrift wordt uiteengezet, een nauwkeurige en consistente methode behelst die in staat is op een anatomisch coherente wijze meerdere organen tegelijk te registreren. Bovendien wordt niet-rigide registratie als essentieel beschouwd bij een veelheid van toepassingen in de radiotherapie, waaronder het optellen van dosisverdelingen en het registreren van beelden die verkregen zijn op verschillende momenten of onder verschillende omstandigheden. De methode is een bruikbaar instrument om verdere ontwikkelingen in de hoge-precisie radiotherapiepraktijk te ondersteunen.

Introducción corta y resumen

He incluido este capítulo para describir en español el contenido de la tesis. Es una traducción 'libre' y adaptación de la introducción en el capítulo 1 y del resumen de la tesis, originalmente escritos en inglés.

R.1. Radioterapia

El objetivo de radioterapia es tratar cáncer y otras enfermedades mediante el empleo de radiaciones ionizantes [103, 119]. Funciona dañando el material genético (DNA) de las células que se encuentran en el área irradiada. Las células que no pueden auto-repararse son eliminadas por el cuerpo. En general, las células saludables son más aptas para repararse que las células cancerígenas, sin embargo ambos tipos de células son afectadas por la radiación. Por lo tanto, uno de los desafíos de radioterapia es dirigir la radiación de manera que sólo las células cancerígenas sean eliminadas, y las células sanas se conserven. Para lograr este objetivo, las imágenes médicas juegan un papel clave.

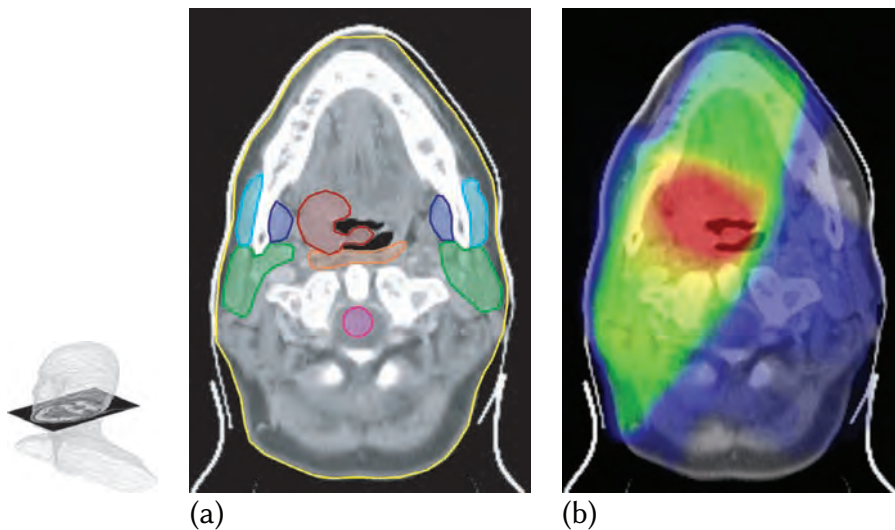


Figura R.1: Tomografía computarizada de un paciente con cáncer en la cabeza-cuello. La imagen en la izquierda representa la orientación de la tomografía en la cabeza del paciente. La tomografía computarizada fue usada para a) identificar el tumor ■, y órganos importantes tal como las glándulas parótidas ■, la médula espinal ■ y los músculos constrictor ■, pterigoideo ■ y masetero ■; y b) planear el tratamiento. Los colores cálidos representan altas dosis de radiación, mientras que los colores fríos representan dosis bajas de radiación.

Imágenes médicas, por ejemplo tomografías computarizadas o resonancias magnéticas, son usadas para localizar el tumor y órganos importantes dentro del cuerpo (ver figura R.1a). Para tratar un paciente con radioterapia externa, en la cual rayos X de alta energía son dirigidos al tumor desde fuera del cuerpo, primero se realiza una tomografía computarizada del área del tumor. Esta tomografía es usada para demarcar con contornos el tumor, otras áreas sospechosas de estar afectadas por cáncer y órganos importantes que deben ser protegidos de altas dosis de radiación. La tomografía computarizada y los contornos de los órganos y del área a ser tratada (el tumor y las áreas sospechosas) son usadas para diseñar un plan de tratamiento, donde las dosis de radiación que cada tejido recibe son calculadas (ver figura R.1b). La radiación es dirigida al paciente por medio de rayos de fotones desde diferentes direcciones. La forma y la intensidad de cada rayo pueden ser amoldadas para reducir la dosis aplicada al tejido sano y concentrar la radiación en el tejido a ser tratado. El tratamiento se aplica al paciente en pequeñas cantidades o fracciones diarias, para permitir a las células sanas repararse del daño de la radiación. Típicamente, un tratamiento puede tomar entre un par de días a un par de semanas. Después de la aplicación de la radiación, la salud del paciente es monitoreada por varios años, para controlar los efectos secundarios y comprobar que el cáncer no reaparezca.

Tumores también pueden ser tratados con radioterapia interna, o braquiterapia, donde se ponen fuentes pequeñas de radiación dentro o cerca del tumor. Las fuentes de radiación pueden ser dejadas permanentemente [105] o pueden ser transportadas dentro y fuera del cuerpo por medio de tubos (catéteres). La radioterapia externa e interna suelen combinarse para obtener un tratamiento en el cual el tumor recibe dosis extra de la braquiterapia.

R.1.1. Precisión del tratamiento y cambios anatómicos

Para minimizar el daño a los tejidos sanos cercanos al tumor, los tratamientos requieren alta precisión. Esto incluye asegurarse que el paciente esté en la misma posición en cada fracción del tratamiento. Sin embargo, es común que la anatomía del paciente cambie durante el tratamiento, debido por ejemplo a razones fisiológica como cambio en los niveles de llenado del estómago, la vejiga y el intestino; o debido al tratamiento, como inflamación, reducción del tamaño del tumor o pérdida de peso (ver figura R.2). Como consecuencia de estos cambios anatómicos, áreas que requieren recibir altas dosis de radiación, por ejemplo el tumor, puede recibir dosis menores; y paralelamente, áreas que fueron planeadas para recibir bajas dosis, como órganos cercanos al tumor,

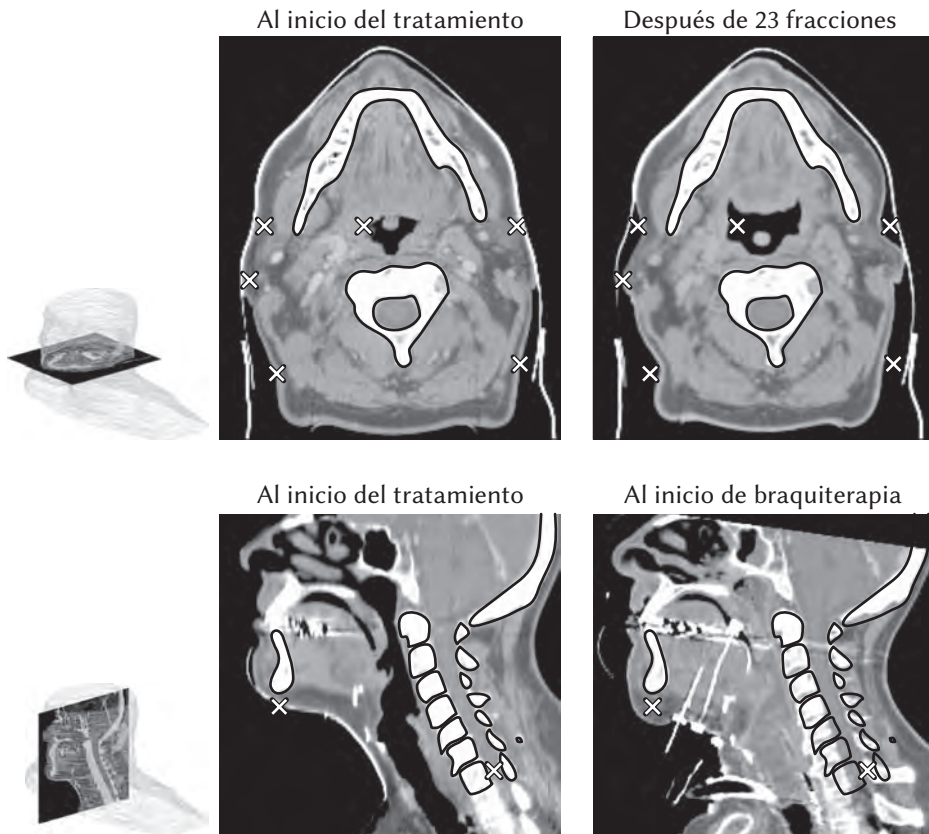


Figura R.2: Cambios en la anatomía de un paciente, vistos en tomografías computarizadas. La primera fila muestra cambios anatómicos causados por pérdida de peso y reducción del tamaño del tumor después de 23 días de tratamiento. La segunda fila muestra cambios anatómicos causados por un tratamiento complementario (braquiterapia), incluyendo inflamación y una posición diferente del paciente. Los cambios anatómicos son indicados con cruces. Los contornos en las imágenes demarcan la mandíbula, algunas vértebras y la base del cráneo de la imagen antes de empezar el tratamiento.

pueden recibir dosis más altas, lo que puede causar efectos secundarios a largo, mediano y corto plazo [89, 30, 49, 71, 74, 4]. Para mejorar los tratamientos de radioterapia, estos cambios anatómicos deben ser tenidos en cuenta. Un primer paso implica seguir los cambios anatómicos mediante el registro de imágenes médicas tomadas en momentos distintos.

R.2. Registro de imágenes

Registro de imágenes se refiere al proceso de identificar los elementos correspondientes en dos imágenes, usualmente del mismo sujeto, y subsecuentemente alinear dichos elementos mediante una transformación geométrica T (definida por una función matemática, [90, 23, 150]). Dependiendo del tipo de transformación usada, el registro de imágenes puede ser rígido o no rígido. El registro rígido de imágenes sólo permite rotar y trasladar las imágenes para alinearlas, lo cual es suficiente cuando el sujeto en las imágenes no sufre ninguna deformación. Sin embargo, cuando la forma del sujeto ha cambiado, como es el caso que se presenta en la figura R.3(a), el registro rígido puede alinear las imágenes globalmente, pero no a nivel local, véase el área de color gris claro bajo en la figura R.3(b). Registro no rígido de imágenes tiene el potencial de alinear también detalles a nivel local, así como se muestra en la figura R.3(c).

Para registrar imágenes, existen dos enfoques: basado en intensidades y basado en atributos. Registro de imágenes basado en intensidades usa las intensidades de los ‘vóxeles¹’ directamente [126, 21, 37, 87]. Para registrar dos imágenes de la misma modalidad, por ejemplo dos tomografías computarizadas, se asume que los vóxeles de un órgano determinado tienen valores de intensidad similares en ambas imágenes. En este caso, los algoritmos tienen como objetivo alinear las áreas con intensidades similares. Por otro lado, cuando las imágenes a ser registradas son de modalidades diferentes, por ejemplo una tomografía computarizada y una resonancia magnética, los vóxeles de determinados órganos pueden tener valores de intensidad distintos. En este caso, los algoritmos buscan alinear áreas con patrones similares, pero no necesariamente de intensidad similar. El registro basado en intensidades se emplea comúnmente para alinear imágenes médicas, pero sus resultados dependen fuertemente de la calidad de las imágenes usadas y son limitados cuando el contraste entre las estructuras u órganos es muy bajo, o si existen efectos no deseados producidos por artefactos extraños en el sujeto, por ejemplo metales en las tomografías computarizadas. Para superar estas limitaciones, enfoques que usan atributos presentes en la imagen en lugar las intensidades de los vóxeles pueden ser usados [133, 63, 50, 13, 113, 84]. Estos atributos pueden ser puntos de referencia anatómicos, marcadores implantados cerca al tumor (normalmente de metal), u órganos delineados (figura R.1a). El problema es entonces encontrar la correspondencia entre los atributos y alinear los atributos

¹un vóxel es un punto en una imagen 3D

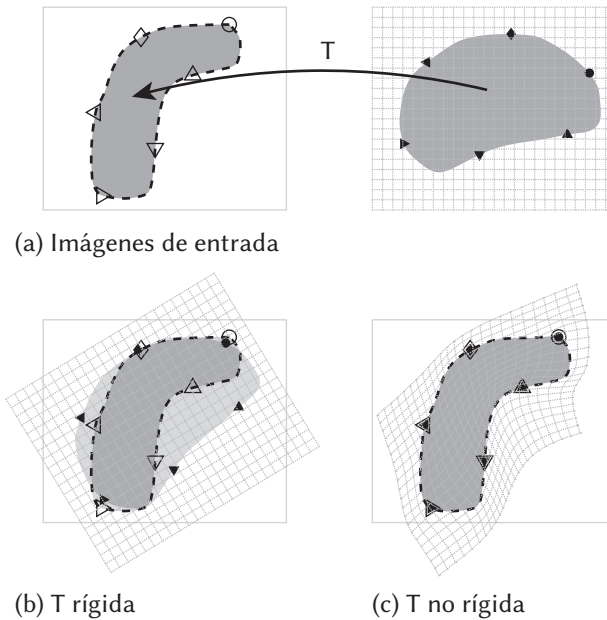


Figura R.3: Registro de dos imágenes. El objetivo es identificar elementos correspondientes en las dos imágenes (mostrados como círculos, triángulos, etc.) y subsecuentemente, encontrar la función o transformación T que alinee los elementos correspondientes. Cuando T es una transformación rígida, limitada a rotaciones y traslaciones, se pueden alinear ambas imágenes a nivel global, pero no local (área gris). En cambio, los detalles locales pueden ser alineados correctamente cuando T es no rígida.

que corresponden.

R.3. Resumen de esta tesis

Esta tesis presenta los cambios esenciales hechos a un método basado en atributos para posibilitar su uso en radioterapia y tres aplicaciones prácticas dentro de este campo. El método original, llamado *thin-plate splines – robust point matching* o TPS-RPM, fue propuesto originalmente por Chui y Rangarajan [25]. En el método, las estructuras a ser alineadas son representadas por dos conjuntos de puntos. El método estima la correspondencia entre los puntos de los dos conjuntos, y actualiza la transformación no rígida iterativamente. La transformación no rígida es modelada por thin-plate splines (véase capítulo 2). El método fue extendido para alinear múltiples órganos simultáneamente, y para permitir incluir información a priori representada con puntos de referencia

anatómicos y otras estructuras (véase capítulo 3). El método fue extendido para generar resultados consistentes que son independiente de la dirección de registro (véase capítulo 4).

La calidad de la transformación que resulta del registro, fue evaluada usando varios métodos. La distancia entre la superficie de los órganos transformados y la superficie de los órganos de referencia determina la exactitud de la transformación. La distancia promedio entre las superficies obtenida fue submilimétrica. En los capítulos 3 y 4, los parámetros fueron afinados en casos con varios grados de deformación: casos en la cabeza-cuello, próstata y cérvix-útero. Para un subconjunto de valores de los parámetros, se obtuvo una exactitud de la transformación de menos de 1 mm. Configuraciones óptimas de los parámetros fueron usados en los capítulos 5 y 6 para asegurar exactitudes de menos de 1 mm.

Otra métrica usada para evaluar la calidad de la transformación fue el error de consistencia. Cuando se alinea un conjunto de puntos A a un conjunto de puntos B, se obtiene una transformación no rígida $T_{A \rightarrow B}$. Paralelamente, la transformación $T_{B \rightarrow A}$ se obtiene cuando se invierten los roles de los conjuntos. Dado que los conjuntos de puntos son los mismos, se espera que los resultados sean consistentes, es decir que $T_{A \rightarrow B}$ sea la función inversa de $T_{B \rightarrow A}$. El error de consistencia mide el nivel de inconsistencia en las superficies de los órganos a ser registrados. Formalmente, es el promedio de las distancias $d(p, T_{B \rightarrow A}(T_{A \rightarrow B}(p)))$ para todos los puntos p en la superficie de los órganos (conjunto A). Se encontraron errores de consistencia entre 1.0 y 1.7 mm para los casos de próstata y cuello y cabeza (capítulos 3 y 5) y entre 4.0 y 4.6 mm para los casos en la región de la pelvis femenina (capítulo 3). En el capítulo 4, los errores de consistencia se redujeron a aproximadamente 1 mm en casos de deformación extrema en la región de la pelvis femenina, cuando la consistencia en la transformación fue reforzada.

Como se ha mencionado, el método puede ser ajustado cambiando los valores de los parámetros internos. La flexibilidad de la transformación puede ser determinada asignando un valor a λ . En los capítulos 3 y 4, la influencia de λ en la exactitud y consistencia de la transformación fue estudiada. Cuando se asignan valores altos a λ , la transformación es mayormente afín, con poca flexibilidad para alinear detalles locales, mientras que valores bajos relajan esta restricción. Valores óptimos para el parámetro λ para varias anatomías, cada una con un nivel diferente de deformación fueron hallados y usados. El nivel de detalle del registro es controlado por la densidad de puntos (radio de densidad r o densidad de puntos ρ). Cuando usan muchos puntos en el registro,

se pueden obtener transformaciones muy exactas, pero exige un alto tiempo de ejecución. Cuando se usan pocos puntos, el tiempo de ejecución se reduce, pero deformaciones locales pueden no ser alineados correctamente. En los capítulos 3 y 4 varias densidades en los conjuntos de puntos fueron evaluados, y recomendaciones son dadas para varios sitios anatómicos, con distintos niveles de deformación.

El uso seguro de registro no rígido en radioterapia exige que las transformaciones sean validadas a nivel anatómico. Se entiende por validación anatómica confirmar que los atributos anatómicos presentes en las imágenes son correctamente alineados. Sin embargo, una validación anatómica de deformaciones es aún un desafío, pues no existe una ‘verdad básica y elemental’². En los proyectos incluidos en esta tesis, se usaron distancias residuales después de aplicar la transformación a puntos o estructuras anatómicas identificadas. En particular, puntos y líneas fueron usados para representar estructuras anatómicas en los capítulos 3, 4 y 7. El cuadro R.1 lista las estructuras usadas por sitio anatómico. En el capítulo 6, un análisis de robustez fue usado como alternativa de validación.

En adición a las mejoras técnicas y los experimentos de validación, tres aplicaciones del método en el campo de radioterapia son descritas en esta tesis: Cuantificación de cambios anatómicos en 3 dimensiones para pacientes de cáncer en la cabeza y cuello, suma de distribuciones de dosis de radiación para dos modalidades de tratamiento (radiación externa y braquiterapia) y registro de hígados con deformaciones de gran magnitud usando venas automáticamente segmentadas.

En el capítulo 5, registro no rígido fue usado para cuantificar cambios anatómicos causados por radiación externa en pacientes de cáncer en la cabeza y cuello. Se usaron dos tomografías computarizadas por pacientes: la tomografía usada para planear el tratamiento, y una tomografía tomada después de 23 días de tratamiento (46 Gy de radiación). Las glándulas salivales (parótidas y submaxilares) y el tumor fueron delineados y registrados. Cada glándula fue rotulada como ‘protegida’ (si no estaba situada en un cuello tratado) o ‘irradiada’ (si estaba situada en un cuello no tratado)³. En total, 15 glándulas irradiadas y 5 glándulas protegidas fueron rotuladas. Patrones de deformación fueron hallados al sintetizar los resultados del registro de todos los pacientes. Las regiones laterales de las glándulas irradiadas se movieron

²Ground truth en inglés

³Dependiendo del tipo y estadio del cáncer se tratan los glándulos linfáticos en uno o ambos lados del cuello. Cada lado del cuello es denominado un cuello.

Cuadro R.1: *Puntos y estructuras anatómicas usadas para validación anatómica.*

Sitio	Atributo anatómico
Cabeza y cuello	Interface entre las glándula parótidas y la mandíbula (líneas) Interface entre las glándulas parótidas y los apófisis estiloides (líneas) Punto superior e inferior de las glándulas parótidas Punto superior e inferior de las glándulas submaxilares
Próstata	Marcadores de oro implantados (líneas) Ápice de la próstata Puntas de las vesículas seminales
Pelvis femenina	Línea media del útero Punta del útero Calcificaciones en el útero Marcadores implantados Punto superior e inferior de la vejiga
Hígado	Bifurcaciones de las venas Quistes Marcadores implantados Bifurcaciones en el árbol biliar

en dirección medial (en promedio 3 mm), mientras que las regiones mediales permanecieron en la misma posición. Las glándulas submaxilares se encogieron y se movieron en dirección craneal. Las glándulas protegidas mostraron una deformación a baja escala (aproximadamente 1 mm en la mayoría de las regiones). Adicionalmente se encontró que la pérdida de volumen de las glándulas parótidas fue proporcional a la dosis promedio planeada ($p < 0,001$).

En el capítulo 6, el registro no rígido fue usado para sumar distribuciones de dosis de radiación para tratamientos combinados de radiación externa y braquiterapia para pacientes con cáncer en la orofaringe tomando en cuenta cambios anatómicos. Dos tomografías computarizadas fueron usadas: la tomografía usada para planear la radiación externa y una tomografía tomada después de la implantación de catéteres y justo antes de la aplicación de la

braquiterapia. También se disponía de las distribuciones de dosis de radiación de cada modalidad de tratamiento. Las glándulas salivales y los músculos usados para masticar y tragar fueron delineados y registrados. La transformación resultante fue usada para mapear la distribución de dosis de radiación de la braquiterapia en la tomografía usada para planear la radiación externa. Las diferencias en fraccionación fueron tomadas en cuenta al usar la dosis equivalente a 2Gy (EQD_2 , de sus iniciales en inglés). La dosis total del tratamiento combinado se usa al sumar vóxel por vóxel la dosis en EQD_2 de cada modalidad. Como alternativa para validar, la robustez de la suma de dosis fue investigada perturbando: los parámetros de entrada del método para registro no rígido (radio de densidad $r = \{5, 6, 8\}$ y $\lambda = 0,5, 5$), los conjuntos de puntos usados para representar los órganos (4 nubes con puntos con coordenadas diferentes), delineaciones (variaciones aleatorias en los contornos definiendo los órganos de 1, 3 y 5 mm de magnitud) y la tasa α/β (2.4, 2.7, 3.3 y 3.6) usada en el EQD_2 . El efecto de las perturbaciones fue cuantificada usando histogramas de dosis vs. volumen (DVH, por sus iniciales en inglés), y un análisis gamma estricto (distancia de consentimiento/diferencia de dosis = 1mm/1Gy)⁴. El análisis gamma mostró índices moderadamente elevados para registros más flexibles ($\lambda = 0,5$), y para variaciones altas en las delineaciones (5 mm). Al analizar las perturbaciones por órganos, el índice gamma fue moderadamente alto para órganos en lugares con gradientes excesivos en la dosis de radiación (índice gama medio ≤ 2.3 para los músculos constrictores) y bajos para el resto de los órganos (≤ 0.7). En los DVH de las dosis totales, solo variaciones pequeñas fueron observadas. En conclusión, el método permitió sumar distribuciones de dosis de radiación para tratamientos combinados (radiación externa y braquiterapia) para pacientes con cáncer en la orofaringe. Áreas con gradientes excesivos aún presentan un reto, pero en general, el método es confiable y robusto con respecto a incertidumbres en las delineaciones de los órganos, perturbaciones en los parámetros del método y tasas α/β para el EQD_2 .

En el capítulo 7, el registro no rígido fue adaptado para segmentar y registrar las venas en tomografías computarizadas y resonancias magnéticas del hígado automáticamente. Las imágenes (la tomografía y la resonancia) fueron tomadas bajo condiciones diferentes y en dos momentos distintos.

⁴Análisis gamma evalúa las diferencias entre las distribuciones de dosis teniendo en cuenta las diferencias en dosis y en distancia entre dosis semejantes. Un índice gamma igual a cero indica la misma dosis en el mismo lugar. Un índice igual a uno indica que la misma dosis fue encontrada a 1 mm de distancia o que la diferencia de dosis en el mismo lugar es 1 Gy. Paralelamente, un índice alto indica una diferencia alta de dosis o la misma dosis en lugares alejados.

Se pidió al paciente retener la respiración mientras se tomaba la resonancia magnética. En cambio para la tomografía, se usó compresión abdominal para reducir el movimiento del tumor ocasionado por la respiración. La compresión abdominal causó deformaciones en el hígado de gran magnitud (en tomografía computarizada), comparado con el hígado en la resonancia magnética. Una medida de 'venosidad', fue usada para segmentar las venas automáticamente. Las líneas centrales de las venas fueron registradas usando una versión adaptada del registro no rígido. Dos estrategias fueron implementadas y validadas: Estrategia A que inicia registrando las líneas centrales de las venas más gruesas, e incrementalmente agrega venas más delgadas al proceso con cada iteración; y estrategia B, que segmenta todas las venas de varios diámetros y registra sus líneas centrales. Distancias residuales entre bifurcaciones de las venas y otros puntos de referencia anatómicos fueron usadas para validar los resultados. La magnitud de deformación del hígado fue estimado usando distancias residuales de las bifurcaciones de las venas y los puntos anatómicos tras un registro rígido. La magnitud de deformación obtenida rondaron entre 2.8 y 10.7 mm. Las distancias residuales tras el registro no rígido oscilaron entre 1.3 y 1.9 mm para las bifurcaciones de las venas y 1.1 y 2.3 mm para los otros puntos anatómicos. Debido a las diferencias en contraste entre las modalidades de imágenes, un gran número de puntos no tenían un punto correspondiente en el otro conjunto de puntos (llamados puntos atípicos). Adicionalmente, la medida de 'venosidad' produjo falsos positivos. El método fue capaz de identificar estos puntos y consecuentemente, ignorarlos al momento de establecer la transformación. La estrategia A se ejecutó más rápidamente que la estrategia B (>2.4 veces), resultando en una exactitud similar.

En conclusión, el método de registro no rígido, basado en atributos presentado en esta tesis se desempeña de manera exacta, precisa, consistente y genera transformaciones que son anatómicamente coherentes. Adicionalmente, el registro no rígido es esencial para muchas aplicaciones en radioterapia, tal como suma de distribuciones de dosis de radiación y registro de imágenes médicas. El método es una herramienta poderosa que puede ser usada para respaldar desarrollos de alta precisión en radioterapia dirigida por imágenes.

Acknowledgements

It has been a long journey, full of challenges, stressful times, and fortunately also, many achievements. Now that the thesis is written, and the date for the defense is settled, I would like to thank people that helped and supported me during the time of my PhD research.

My promoter, Prof. B. J. M. Heijmen. Ben, apart from the support you have given me on the professional side during my PhD research, you also gave me a warm welcome to the Netherlands. Being far from home is not easy, especially in the first months, and you and your family were a great support.

My copromoter Dr. M. S. Hoogeman. Mischa, thank you very much for all the support and supervision. Even in busy times, whether it was for discussing or for revising my articles, you always made time for me. I have been very lucky to have you as my supervisor.

Prof. P.C. Levendag. Peter, thank you very much for all the support, but especially for all the enthusiasm you always showed towards my research. Muchas gracias señor Levendag!

The co-authors of the articles included in this thesis: Abraham Al-Mamgani, Luiza Bondar, Ben J. M. Heijmen, Mischa S. Hoogeman, Inger-Karine K. Kolkman-Deurloo, Peter C. Levendag, Alejandra Méndez Romero, David N. Teguh, Piotr Wielopolski, Andrés Zolnay. I thank you for all the support and effort put into the research and writing. The diversity of your view points helped to enrich our investigations.

Dr. D. N. Teguh. David, we started almost at the same time in the Daniel, and since then we have shared the office. You also gave me the honor of being your paranymph. Besides talking about daily life, you are always there to clarify my doubts about medical terms. It is a pleasure to share the room with you. :)

My paranymphs and friends Sarah O. S. Osman and Angélica María Gómez. Dear Sarah, you once mentioned that Wouter and me were your family in the Netherlands. I feel the same way. Thank you for being there whenever I felt the need to let a scream go, or just to have a cup of tea and a muffin. I'm eager to share with you, Aymen and Kamal, the new phase of your lives.

Gie, hemos sido amigas desde pequeñas, y aunque vivamos a miles de kilómetros, ese vínculo sigue creciendo. Muchas gracias por 'tener la cabeza loca', como dice tu abuela, por escribir correos que me hacen reír por montones y por leer tantas barrabasadas de mi parte. Es un honor para mi, contarme entre tus amigos.

My family in Colombia. Estar y vivir lejos de Medellín ha sido difícil. Son las pequeñas cosas las que más se extrañan: subir a saludar a la abuela Rosa, darle un abrazo a mis primos, acostarme a ver tv con Ara, prender las velitas en

diciembre con todos, visitar a los abuelos en Barranquilla, etc. Mi familia me ha brindado apoyo incondicional siempre, sin el cual no estaría aquí, terminando este doctorado. Agradezco particularmente a mi mamá, Aracely, que ha sido mi roca desde siempre.

My extended family in the Netherlands. Thanks to the family of Wouter, particularly Freek and Fia, who welcomed me as part of the family since the very beginning.

My partner in crime. Wouter, who has been able to put up with all my bad mood during stressful times, supported me in everything I can think of, and always showed me his love unconditionally. ♥

Curriculum vitae



Eliana María Vásquez Osorio was born on March 30th, 1980 in Medellín, Colombia. She studied computer sciences at EAFIT University, Medellín, and has been involved with research since 1998, when she started as a research assistant at the Knowledge Engineering Laboratory. Later, in 1999, she became a member of the computer-aided design, manufacturing and engineering (CAD/CAM/CAE) laboratory. Her research involved developing industrial and scientific applications using computational geometry. In 2000 and 2002, Eliana was invited for a research

internship by the Department for Cognitive Computing & Medical Imaging (A7) at Fraunhofer Institute for Computer Graphics (IGD), Darmstadt, Germany. During these visits, Eliana participated in the development of algorithms for image-model matching, surface reconstruction, contour interpolation from multi-axial sampled data (medical imaging) and image matching.

In 2003, Eliana obtained her Bachelor of Science degree in computer science. The topic of her thesis was “Surface Reconstruction”, which was developed under the collaboration of the CAD/CAM/CAE Laboratory at EAFIT University and the department of Cognitive Computing & Medical Imaging at Fraunhofer Institute for Computer Graphics.

After the completion of her studies at EAFIT university, Eliana joined the department of Radiation Oncology at Erasmus Medical Center, Rotterdam, the Netherlands, as a PhD student. Her research included development, implementation and validation of a feature-based non-rigid registration method, and

applications in the field of radiotherapy. Currently, Eliana works as a post-doc researcher in the department of Radiation Oncology at Erasmus Medical Center, Rotterdam.

List of publications

Journal Articles

1. E. M. Vásquez Osorio, M. S. Hoogeman, D. N. Teguh, A. Al-Mamgani, I.-K. K. Kolkman-Deurloo, L. Bondar, P. C. Levendag, and B. J. M. Heijmen. Three-dimensional dose addition of external beam radiotherapy and brachytherapy for oropharyngeal patients using nonrigid registration. *International Journal of Radiation Oncology*Biophysics*, 80(4):1268 – 1277, 2011.
2. L. Bondar, M. S. Hoogeman, E. M. Vásquez Osorio, and B. J. M. Heijmen. A symmetric nonrigid registration method to handle large organ deformations in cervical cancer patients. *Medical Physics*, 37(7):3760–3772, 2010.
3. E. M. Vásquez Osorio, M. S. Hoogeman, L. Bondar, P. C. Levendag, and B. J. M. Heijmen. A novel flexible framework with automatic feature correspondence optimization for nonrigid registration in radiotherapy. *Medical Physics*, 36(7):2848–2859, 2009.
4. E. M. Vásquez Osorio, M. S. Hoogeman, A. Al-Mamgani, D. N. Teguh, P. C. Levendag, and B. J. M. Heijmen. Local anatomic changes in parotid and submandibular glands during radiotherapy for oropharynx cancer and correlation with dose, studied in detail with nonrigid registration. *International Journal of Radiation Oncology*Biophysics*, 70(3):875 – 882, 2008.

-
5. G. J. van der Wielen, T. F. Mutanga, L. Incrocci, W. J. Kirkels, E. M. Vásquez Osorio, M. S. Hoogeman, B. J. M. Heijmen, and H. C. J. de Boer. Deformation of prostate and seminal vesicles relative to intraprostatic fiducial markers. *International Journal of Radiation Oncology*Biology*Physics*, 72(5):1604 – 1611, 2008.
 6. W. Wunderink, A. Méndez Romero, E. M. Vásquez Osorio, H. C. de Boer, R. P. Brandwijk, P. C. Levendag, and B. J. M. Heijmen. Target coverage in image-guided stereotactic body radiotherapy of liver tumors. *International Journal of Radiation Oncology*Biology*Physics*, 68(1):282 – 290, 2007.

Short Papers and Conference Abstracts

1. S. Leinders, Y. Seppenwoolde, S. Breedveld, E. Vásquez Osorio, A. Méndez Romero, and B. Heijmen. 534 oral adaptive liver sbrrt: Daily re-planning to compensate for non-rigid anatomy changes improves dose distributions. *Radiotherapy and Oncology*, 99(Supplement 1):S218, 2011. (abstract).
2. E. Vásquez Osorio, M. Hoogeman, D. Teguh, I. Kolkman-Deurloo, L. Bondar, P. Levendag, and B. Heijmen. 3d dose addition of external beam radiotherapy and brachytherapy for oropharyngeal patients using non-rigid registration. *ICCR: Proceedings of the XVth International Conference on the Use of Computers in Radiation Therapy*, 1:Track 12408, May 2010.
3. S. Breedveld, P. R. M. Storchi, L. Bondar, E. M. Vásquez Osorio, M. S. Hoogeman, and B. J. M. Heijmen. A fast and accurate automated method for online re-planning in adaptive radiotherapy. *ICCR: Proceedings of the XVth International Conference on the Use of Computers in Radiation Therapy*, 1:Track 12391, May 2010.
4. S. Breedveld, P. Storchi, M. Bondar, E. Vásquez Osorio, M. Hoogeman, and B. Heijmen. Fast on-line plan adjustment for adaptive radiotherapy evaluated for prostate and cervical cancer. *International Journal of Radiation Oncology*Biology*Physics*, 78(3, Supplement):S744 – S745, 2010. (abstract).
5. P. Levendag, M. Hoogeman, D. Teguh, T. Wolf, L. Hibbard, O. Wijers, B. Heijmen, P. Nowak, E. Vásquez Osorio, and X. Han. Atlas based auto-segmentation of ct images: Clinical evaluation of using auto-contouring

in high-dose, high-precision radiotherapy of cancer in the head and neck. *International Journal of Radiation Oncology*Biography*Physics*, 72(1, Supplement):S401, 2008. (abstract).

6. E. Vásquez Osorio, M. Hoogeman, A. Al-Mamgani, D. Teguh, P. Levendag, and B. Heijmen. Non-rigid point matching and its application in radiotherapy. *ICCR: Proceedings of the XVth International Conference on the Use of Computers in Radiation Therapy*, 2:413–417, June 2007.
7. E. Vásquez Osorio, M. Hoogeman, A. Al-Mamgani, D. Teguh, P. Levendag, and B. Heijmen. Shape changes in head and neck radiotherapy assessed with non-rigid feature registration. *Proceedings of the First Dutch Conference in Bio-medical Engineering*, 1(1):track number 4, 2007. (abstract).
8. E. Vásquez Osorio, M. Hoogeman, A. Al-Mamgani, D. Teguh, P. Levendag, and B. Heijmen. Shape changes in h&n radiotherapy assessed with non-rigid feature registration. *Radiotherapy and Oncology*, 81(Supplement 1):S352, 2006. (abstract).

Chapter in book

1. Chapter 14. Non-rigid registration in *Contouring in Head & Neck Cancer*, P. C. Levendag, A. Al-Mamgani, and D. N. Teguh, editors. Elsevier Professional Education, 2009. ISBN 978-3-437-59904-0.



PhD Portfolio

Summary of PhD training and teaching

Name PhD student:	PhD period:
E.M. Vásquez Osorio	2004 - 2011
Erasmus MC Department:	Promoter:
Radiotherapy	Prof.dr. B.J.M. Heijmen
Research School:	Supervisor:
Molecular medicine	Dr. M.S. Hoogeman

1. PhD training	Year
General courses	
Biomedical English Writing and Communication. Erasmus MC, Rotterdam	2007
Oral and poster presentations at international conferences	
XVIth International Conference on the Use of Computers in Radiation Therapy. ICCR Amsterdam, The Netherlands	2010
XVth International Conference on the Use of Computers in Radiation Therapy. ICCR Toronto, Canada	2007
European Society for Therapeutic Radiology and Oncology. ESTRO Leipzig, Germany	2006
Other presentations	
Molecular Medicine Day. Rotterdam, The Netherlands	2010
Nucletron's user meeting. Amsterdam, The Netherlands	2010
First Dutch Conference on Bio-medical Engineering. Egmond aan Zee, The Netherlands	2007
Kring voor Radiotherapeutische en Klinische Fysica. Eindhoven, The Netherlands	2007

Attendance to international conferences		
IEEE Shape Modeling International Conference.	2005	
		Boston, USA
ACM Solid and Physical Modeling Symposium.	2005	
		Boston, USA
<hr/>		
2. Teaching		Year
<hr/>		
Internal presentations		
Refeeravond: 3D Dose Addition of Combined EBRT and BT for Oropharyngeal Patients	2009	
Journal club: Deformation and Motion in the Liver	2009	
Refeeravond: Flexible Framework for Non-rigid Registration in Radiotherapy	2008	
Journal club: Algorithms for Autosegmentation	2008	
Refeeravond: Shape Changes in Head and Neck in Radiotherapy Assessed with Non-Rigid Registration	2007	
Journal club: Mathematical Background of Non-rigid Registrations	2007	
Journal club: Finite Element Analysis	2006	
Journal club: Radiation Induced Anatomical Changes During the Course of Fractionated Radiotherapy	2006	
Journal club: Non-rigid Matching	2005	
<hr/>		
3. Distinctions and awards		Year
<hr/>		
Article selected as Issue Highlights of the International Journal of Radiation Oncology*Biology*Physics	2008	
Honorable Mention - E-Poster, XVth International Conference on the Use of Computers in Radiation Therapy, ICCR	2007	



The
end